MODELLING AND STABILITY ANALYSING OF FRACTIONAL FREQUENCY OFFSHORE WIND POWER SYSTEM WITH MODULAR MULTILEVEL MATRIX CONVERTER

by

KAI LIN

A thesis submitted to

The University of Birmingham

for the degree of

DOCTOR OF PHILOSOPHY

Department of EESE,

School of Engineering

The University of Birmingham

August 2022

ABSTRACT

Offshore wind energy contributes significantly to the reduction of carbon emissions and the dependability on fossil fuels. Current transmission systems have been challenged by the growth trend of offshore wind power system establishments. The maximum transmission distance of the traditional high voltage AC (HVAC) transmission is hampered by the reactive current charging requirement. In contrast, the fractional frequency transmission system (FFTS) is a promising technology to solve this issue. The offshore grid is designed with a fractional frequency equal to around one-third of the system frequency, which significantly reduce the charging current of the transmission system. The frequency converter is the central component of the FFTS, and the modular multilevel matrix converter (M^3C) is regarded as the recognised new AC/AC converter technology for offshore wind power integration due to its advantages of simple scalability, full controllability, and high effectiveness. The system structure, working principle, and control system of the M^3C are presented initially in this study in Chapter 3 with the electromagnetic (EMT) simulation model developed in MATLAB/Simulink software. It has been demonstrated that M^3C can serve as the frequency converter for FFTS.

The small signal stability is an enduring topic of power system study. The M^3C based FFTS is shown to be a competent contender for offshore wind power system integration, therefore, a small signal model is required to examine its damping ability. In Chapter 4, the small signal model of FFOWPS contains the doubly fed induction generator (DFIG) based wind power system and the M^3C is proposed, taking into account the dynamics of DFIG system, the M^3C and the interaction between the two power electronic systems. In addition, an eigenvalue based small signal stability analysis is implemented to examine the impacts of controller parameters and circuit elements on the damping ability of the system.

It is proven that the proposed DFIG-M^3C based FFOWPS has numerous technical advantages, nevertheless, its economic viability must be evaluated in order to determine its industrial applicability. A techno-economic cost comparison between M^3C and back-to-back modular multilevel converter (BtB-MMC) is presented in Chapter 5. The two frequency conversion technologies utilised in FFOWPS are studied and compared in terms of technical performance. The performance of the two technologies is validated. For further comparison, an economic analysis model incorporating the capital costs, unavailability costs, operation and maintenance (O&M) costs, and power loss costs for FFOWPS components is developed. Cost components comprising a significant portion of the total cost are highlighted in the two versions of FFOWPS and it is indicated the wind turbine consist of up to 50% of total cost of FFOWPS. To further pursue the economic advantage of the M^3C based FFOWPS, the economical transmission distance of the M^3C based FFOWPS and BtB-MMC based HVDC system is investigated, and hence the advantageous transmission range of the two technologies is identified while the M^3C based FFOWPS is a more cost effectiveness choice for medium transmission distances around 280 km.

ACKNOWLEDGEMENT

First and foremost, I want to express my profound gratitude to Prof. Xiao-Ping Zhang, my lead supervisor, who broadened my interests in research and guided me during my PhD study. I consider it a great honour to have Prof. Xiao-Ping Zhang as my PhD study supervisor. Due to his wise advice, I never strayed from my path.

Second, I would like to express my thanks to Dr. Dilan Jayaweera, my co-supervisor, for teaching me knowledge about renewable energy. Next, I want to extend thanks to Dr. Ying Xue and Dr. Jianing Li for their inspiration, support, and assistance with my research.

Additionally, I would want to thank all of my friends, especially my research colleagues. They gave me a wealth of enjoyable recollections. They are Dr. Jiajie Luo, Dr. Xianxian Zhao, Dr. Conghuan Yang, Dr. Zuanhong Yan, Dr. Min Zhao, Dr. Cong Wu, Longmao Fan, Chenyixuan Ni, Nan Chen, and Xin Ma.

Finally, I am grateful to my parents, Mr. Huabin Lin and Ms. Airong Shi, for their unwavering love and support throughout my entire life.

Table of Contents

List of Figures

List of Tables

List of Abbreviations

BtB	back-to-back
DFIG	doubly fed induction generator
EMT	electromagnetic transient
FFOWPS	fractional frequency offshore wind power system
FFTS	fractional frequency transmission system
HVAC	high voltage alternating current
HVDC	high voltage direct current
IGBT	insulated-gate bipolar transistor
MMC	modular multilevel converter
M^3C	modular multilevel matrix converter
O&M	operation and maintenance
PMSG	permanent magnet synchronous generator
SVM	space vector modulation
VSC	voltage source converter

Chapter 1 Introduction

The background and research interests are introduced in this chapter. The development of renewable energy in recent years is introduced, and the offshore wind power system is discussed in particular. The power transmission technologies are introduced, and considering the integration with offshore wind power, the fractional frequency offshore wind power system is discussed. The frequency converters, which are the key component of FFTS, are discussed in greater detail, with a focus on the new generation technology modular multilevel matrix converter (M^3C). The research motivations are given based on the technologies introduced, and the study contributions are listed. The thesis outline is given at the end of the chapter.

1.1 Background and Motivation

1.1.1 Development of Renewable Energy and Offshore Wind Power

Energy demand has been increasing rapidly with the development of human civilization since the start of the Industrial Revolution. The primary energy sources have been the main supply for industrial development since the last century and will continue to play a key role in global energy systems [1]. ig.1.1 shows fossil fuel consumption in the last 50 years. However, the emissions from fossil fuel burning are also the main contributors to climate change and air pollution. Fig.1.2 shows the rapidly increasing emissions in recent years due to the increasing consumption of primary energy sources. To deal with an increasingly severe situation, the Net Zero target is set to decrease greenhouse gas emissions to close to zero, apart from any remaining greenhouse gas re-absorbed methods [2]. Fig.1.3 shows the growing number of countries announcing the pledge to Net Zero and the covered emissions.

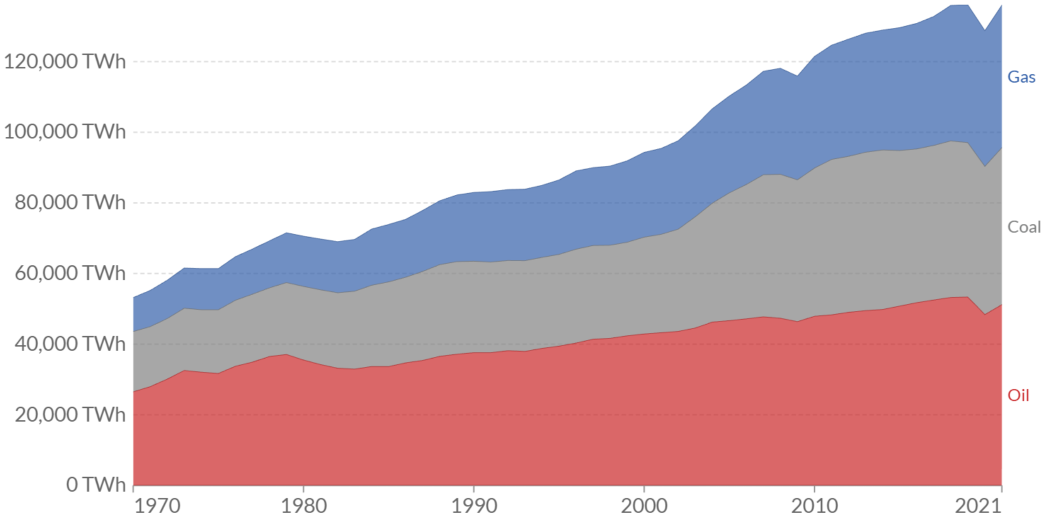

Fig. 1.1 World fossil fuel consumption. [1]

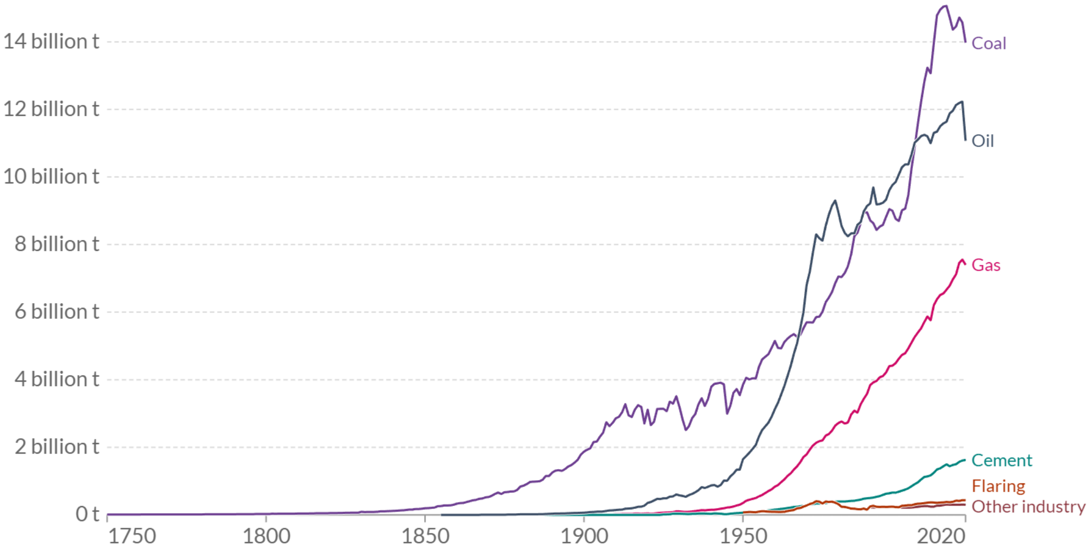

Fig. 1.2 World CO_2 emissions by fuel. [1]

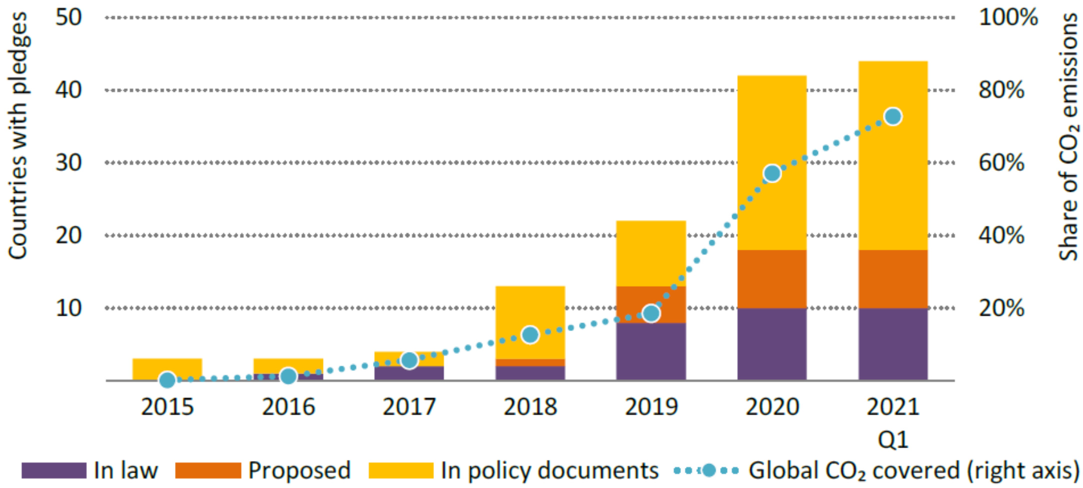

Fig. 1.3 Number of national net zero pledges and covered CO_2 emissions. [2]

In order to meet the target, the renewable energy draws attention of the countries across the world. As Fig. 1.4 shown, the renewable energy generation growth up quickly in recent years, and about 84% new power generating capacity installed in 2021 belongs to renewable energy [3]. It can also be found from Fig. 1.4 that the wind, solar and hydropower are currently the main renewable energy sources. The increasing of hydropower is not distinctly in recent years, however, the installation of solar and wind has a dramatic increase in last decade and further planning. As it known, both wind and solar power generation have geographical limitations, the development of new renewable generation is varied on different area. Table 1.1 shows the annual installed renewable generation capacity in UK since 2014 [4]. As can be seen, the wind and solar are the main contributor of UK's renewable power grid. However, it also can be seen the growth of solar power slows down after 2015, while the wind power keeps growing up. There were 1,290 MW new installed wind generation even with the impact of Covid-19 pandemic. In worldwide, the new installed wind power generation of 2021 reach to 102 GW, forming a total 845 GW cumulative capacity [3]. It proves that the wind power is a promising renewable energy source.

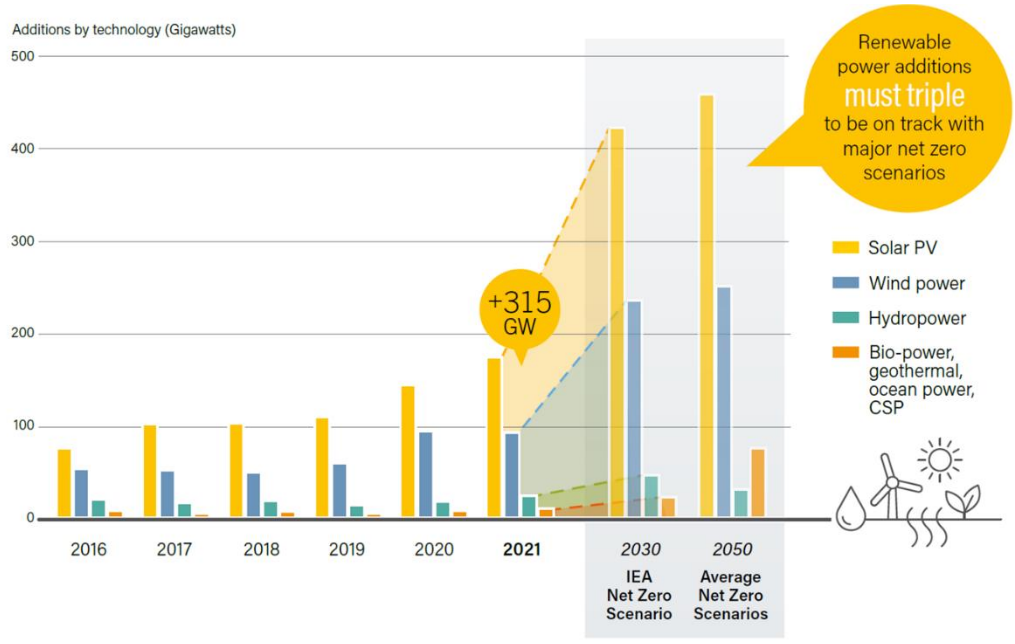

Fig. 1.4 Annual growth of renewable power capacity [3]

TABLE 1.1 RENEWABLE GENERATION CAPACITY(MW) IN UK

Year	Growth Generation Capacity		Cumulative Generation Capacity	
	Wind	Solar	Wind	Solar
2014	1,792	2,591	13,074	5,528
2015	1,232	4,073	14,306	9,601
2016	1,820	2,313	16,126	11,914
2017	3,459	846	19,585	12,760
2018	2,020	299	21,605	13,069
2019	2,281	286	23,887	13,345
2020	571	234	24,458	13,579
2021	1,290	386	25,748	13,965

The wind power plant can be distinguished as onshore wind farm and offshore wind farm by its location. As mentioned above, the wind power generation has its geographical restrictions, and at the early development stage of wind power, the power plant are usually installed onshore considering the economical suitability and technology limitation. With the development of wind generation technology and the increasing plant capacity, and also, the land limitation, the offshore wind power becomes more and more popular cross the world. Offshore wind farm brings the benefits of rich primary resource, less geographical restrictions and community friendly. Fig.1.5 shows the installed offshore wind generation capacity within the Europe countries. As it shown, the increasing of new installed offshore wind power capacity is growing up across the different Europe countries, and predictable, it will keep increasing in upcoming years considering the trend of renewable growth. At the quarter one of 2022, 15% electricity generation of UK came from offshore wind plant [5]. Based on the latest British Energy Security Strategy, the UK government is planning to deliver up to 50 GW offshore wind power by 2030 to meet its New Zero target [6]. Furthermore, China is also increasing its offshore wind power capacity dramatically. In 2021, the new installed offshore power capacity within the China has reached to 16.9 GW, which has made up 80% total new installation of the world [7]. It is no doubt that the offshore wind power system occupying a vital position within the world's power system and the Net Zero process.

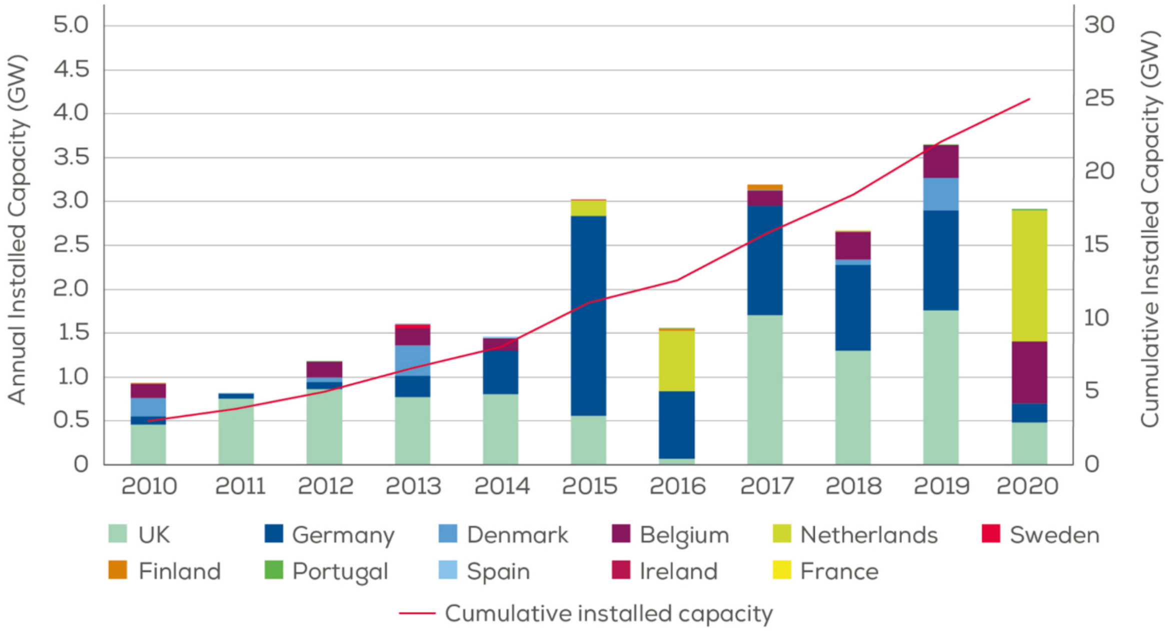

Fig. 1.5 Annual and cumulative installed offshore wind generation capacity [8]

Obviously, the offshore wind power system has its benefits and worthy to vigorous expansion, however, it has brought not only the merits but also the challenges. The most directly problem, the process of Net Zero requires replace the traditional fossil fuel generation plant with the renewable wind power plant, which also means the amount of synchronous generator has been reduced, while the percentage of converter control generator like wind turbine and PV panels are increased. Due to this reason, the inertia of current power system has been reduced significantly, which has affected system stability [9]. To solve this problem, the researches focused on low inertia system are needed. There are studies proposed the grid forming technologies [10, 11], to design a control method implemented on the grid connected inverter of renewable source to performance the behaviour of the synchronous generator. But still, more studies and validation are required before they could be served in practical power grid.

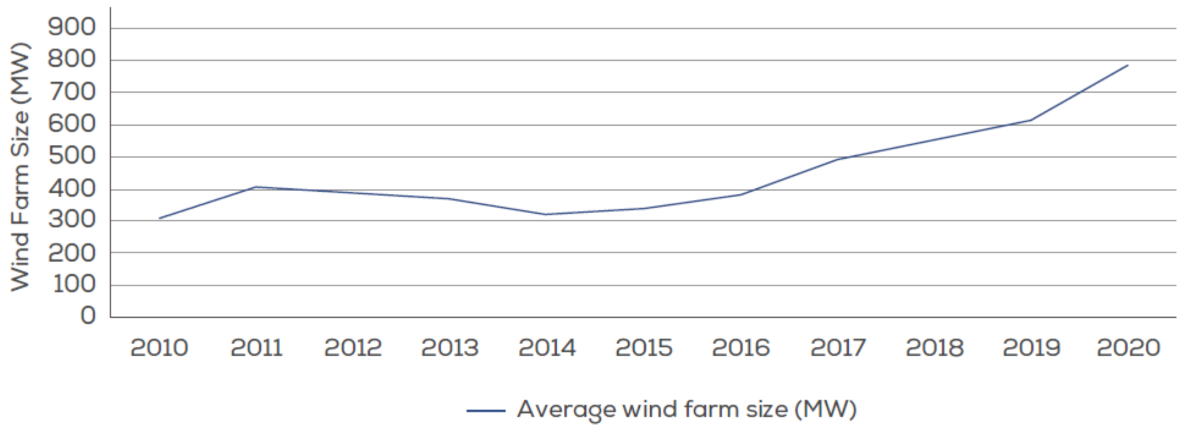

Fig. 1.6 Average size of commercial offshore wind farm projects in the year. [8]

Besides, the wind generation depends on the primary of wind source, which has extreme uncertainty. It brings the challenge to power planning as the current power system is unlikely to transmit and consume the all the wind power generated due to the constraints in the current transmission system and lack of long-term storage system. For instance, the National Grid ESO has paid 261 million pounds to turn wind plants down in the UK during 2020, and that cost ultimately went to the consumer’s bill [12].

Furthermore, regarding the rapidly developing wind technology, the rating of wind turbines has been increased towards the next generation. The average size of the installed wind farm in 2020 has reached 8.2 MW and the rating of the new turbine ordered in 2022 will be increased to 13 MW [8]. Foreseeable, the size of wind farms will keep growing. Fig. 1.6 shows the average size of wind farm growth in recent years. As it is shown, the size of offshore wind farms has been doubled since the last 10 years, and there is still more incoming commissioning of large-scale wind farms in the UK. On the other hand, considering the growing offshore wind plant establishing, the wind farm will have to be pushed further away from the coast, which will cause trouble for current traditional AC transmission system.

Among these technological challenges, due to the limited space and time, only new transmission technologies for offshore renewable energy will be the focus of this thesis. To sum up, the upgrade of the current transmission system is imperative. Different transmission technologies are introduced in the next subsection.

1.1.2 Transmission Technologies and Fractional Frequency Offshore Wind Power System

The traditional high voltage AC transmission (HVAC) system is the main served transmission technology for wind farm transmission in the world [13]. With years of studies and practical application experience, HVAC is a mature technology to transmit power with minimum cost. Compared to onshore power plant, the offshore wind farm requires more mature transmission technology. Currently, all the offshore wind in the UK is applied with HVAC transmission technology. However, the power capacity and transmission distance are the main challenges of HVAC due to the limitation of its capacitive charging current requirement [14, 15]. Currently, the HVAC transmission distance has been limited by around 100 km even with the reactive compensation devices [16]. As mentioned in last subsection, as the offshore wind farm is developed with the trend of larger size and further distance from coast, the HVAC may not be suitable for the task of transferring power from the far offshore wind farm.

The high voltage DC transmission (HVDC) system is the solution against the long distance transmission requirement. The offshore rectifier station transfers the AC power from the wind farm to DC, and then transmit it with high voltage level to the onshore inverter station and converts it back to AC. There are two kinds of HVDC system Categorised by the type of converter, the Line Commutated Converter (LCC) and Voltage Source Converter (VSC). For DC transmission, there is no constraint of the charging currents and the distance can be further extended. However, the requirement of large ac filter is the main economic disadvantage of HVDC system. A study introduced a flexible LCC-HVDC to provide no filter system with inserting the controllable capacitors [17]. Besides, with the increasingly strict requirements related to the power quality and fault ride through ability applied to the offshore wind farm transmission system, the traditional thyristor valve based LCC-HVDC may not be capable of the transmission job for future offshore wind due to its low controllability. The flexible LCC-HVDC in [17] would be a promising next generation LCC HVDC to deal with all the shortcomings of the traditional LCC HVDC, which can overcome the commutation failure and provide control of both active and reactive power. The VSC based HVDC system own the better controllability and requires no reactive compensation [18]. And with the further development, the modular multilevel converter (MMC) based HVDC has been introduced to provide fully controllability and higher scalability [19]. Nevertheless, the HVDC system still suffers the problem of hard to design the DC circuit breaker and limitation of fault level [20].

The fractional frequency transmission system (FFTS), or so called low frequency AC transmission system, has been introduced in [21]. Not considering the normal system frequency (50Hz/60Hz), the FFTS uses the smaller frequency, normally one third of the grid frequency for AC transmission from the perspective of the availability of the related equipment, existing operating experience, economic efficiency and technicality [22]. It simply provides large transmission capacity with lower impedance due to the lower frequency [23]. And for offshore wind power system, there is no need to build the offshore converter station, and the gearbox of wind turbine can be simplified as it only needs to output low frequency power [24]. The onshore AC/AC converter station is the key component of the FFTS as it needs to convert the power frequency back to system level for main grid integration.

Three main transmission technologies have been introduced above. The advantages and disadvantages of each transmission system are summarised in Table. 1.2. For offshore wind power system, even though the site of wind farm is expected to be more far away from the coast, but the maintenance and installation of plant should also be considered. Besides, considering the growth of the size of offshore wind farm, the offshore wind farm grid with a medium distance to the coast is expected to be built in the future.

TABLE 1.2 ADVANTAGES AND DISADVANTAGES OF TRANSMISSION TECHNOLOGIES

Technology	**Pros**	**Cons**
HVAC	• Mature technology • Low cost	• Limit transmission capacity • Short distance
HVDC	• Long distance transmission • Isolation of two AC grid	• Hard to design DC circuit breaker • Fault level limitation
FFTS	• Offshore station simplification • Higher transmission capacity • Easy to integrated	• Bigger offshore transformer

In that case, the FFTS is a competitive candidate for offshore wind power integration. There will be more details about the power electronics of FFTS introduced in the next subsection.

1.1.3 Power Electronics of FFOWPS

Based on the discussion presented above. The FFTS is a suitable choice for offshore wind power plant integration. The fractional frequency offshore wind power system (FFOWPS) is introduced. Within the FFOWPS, the offshore wind generation and onshore frequency converter are the main power electronics. For wind generation, it can be divided into two kinds based on the speed range as fixed speed wind turbine and variable speed wind turbine [25]. Fig. 1.7 shows the structure of the fixed speed wind turbine. The squirrel-cage induction generator (SCIG) connects the wind turbine to the gird via the switch and step-up transformer. The generator speed is fixed by the pre-set synchronous speed in spite of the change of wind speed [26]. And as the SCIG is directly connected to the grid, the slip speed of the generator rotor is affected by the grid frequency, hence, the power output of the generator is followed the change of grid frequency, which provides the system inertia support [27].

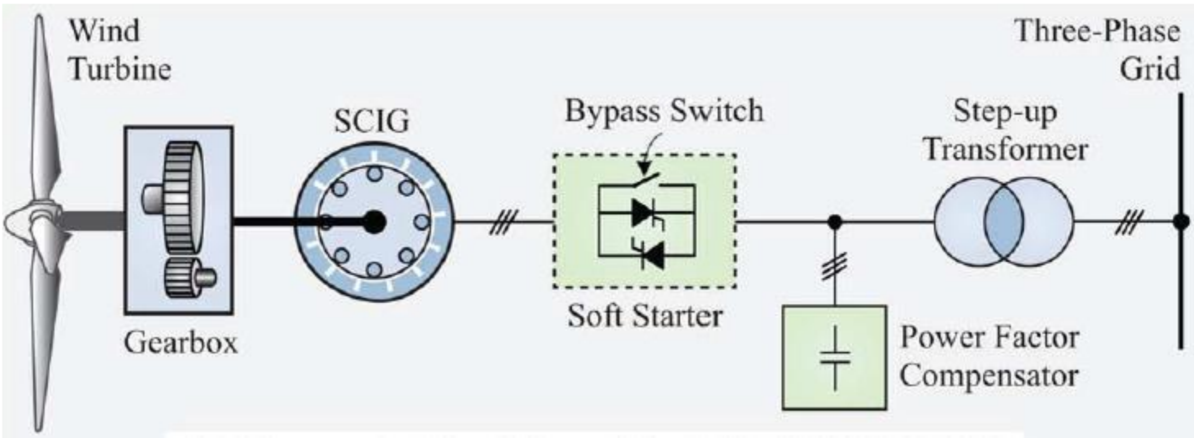

Fig. 1.7 Structure of fixed speed wind turbine [25].

Although the fixed speed wind turbine provides the merits including simple structure and easy interface, the wind power conversion efficiency is relatively low. In that case, the variable speed wind turbine is developed to capture more power from the wind source. Fig. 1.8 shows the doubly fed induction generator (DFIG) based wind turbine. As figure shown, the power from the wind turbine is transmit to grid via both stator and rotor windings, in this configuration, the size of the back-to-back power converter only need be 30% of the DFIG generator rating to severe the system [28]. The rotor side converter (RSC) applied the maximum power point tracking (MPPT) to control rotor speed to capture the maximum wind power, while the grid side converter (GSC) control maintain the DC link voltage and transmit the power from rotor to the grid. As the rotor speed is control by the converter in spite of the change of the wind speed, the DFIG system cannot help with the inertial response to the grid [29]. Compared to fixed speed wind turbine, the DFIG based wind power system provides the merits including better power conversion efficiency and flexible controllability, which is suitable to the offshore wind power generation. A further discussion about DFIG system is provided in Chapter 3.

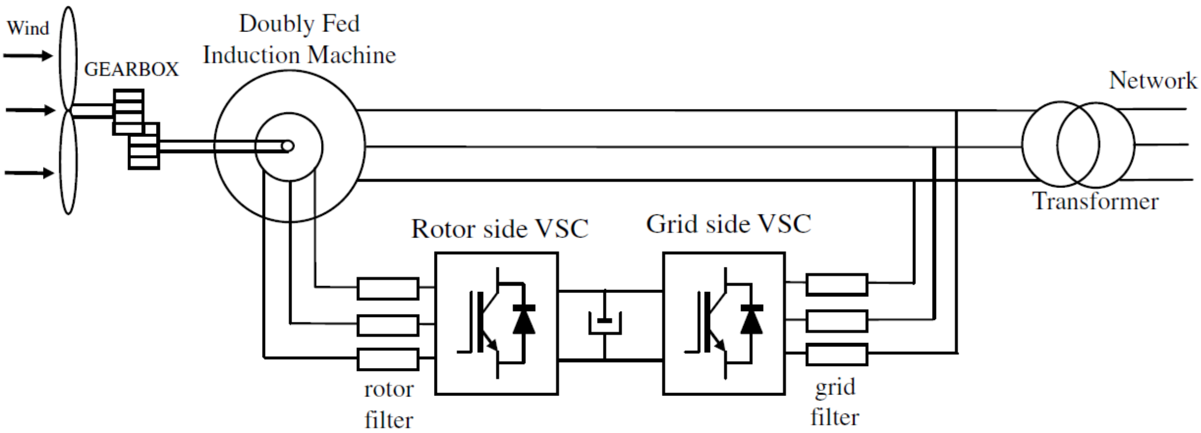

Fig. 1.8 Structure of variable speed wind turbine DFIG [29].

In addition to wind generation system, in order to stepped the fraction frequency back to system frequency standard, the onshore AC/AC converter, or frequency converter is also the key component of the FFOWPS. The frequency converter undertake the task to connect the fractional frequency offshore wind power system to the system frequency main grid, which determines the performance of the FFOWPS. At the early stage, before the insulated-gate bipolar transistor (IGBT) technology fully developed, the cycloconverter, which applied with the thyristor was a widely used AC/AC converter for driving the motor [30-32] and converting frequency within the FFOWPS [33, 34]. However, the later studies found that the cycloconverter is not capable of integrating the offshore wind power system due the lack of controllability, poor power quality and weak fault ride through ability [35]. With the widely use of the IGBT for power electronic applications, the Back-to-Back MMC (BtB-MMC) has been introduced, which provides highly controllability and large scalability as the AC-DC-AC converter for motor driving and offshore wind generation integration [36, 37]. Another technology, named Modular Multilevel Matrix Converter (M^3C), which was proposed in 2001 [38], is regarded as the next generation AC/AC converter. The structure of M^3C is shown in Fig. 1.9. As figure shown, there are nine arms with 3×3 matrix arrangement, and each arm composed of a series of full bridge IGBT based submodules. Same as the BtB-MMC, the M^3C also enjoy the merits including full controllability, flexible scalability and good power quality. Compared to BtB-MMC, the M^3C is more suitable and can satisfy the same system requirements using fewer submodules and smaller rating capacitors [39, 40]. The M^3C is designed for high voltage level power system, which is compatible to the offshore wind power system. The detail review of M^3C is provided in next chapter.

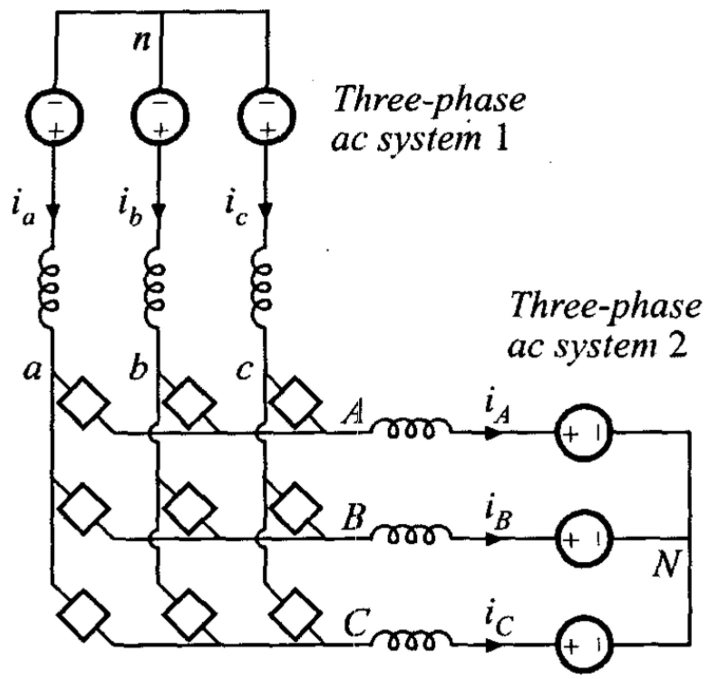

Fig. 1.9 Basic configuration of M^3C [38].

1.1.4 Research Motivations

With the increasingly serious climate change impacts and energy source scarcity, the development of renewable energy became the priority task across the world. With years development and practical application experiences, the offshore wind farm is becoming popular considering its rich primary resource, suitable for large scale development and community friendly. In order to accomplish the Net Zero target, new offshore wind power plants are being developed worldwide, which not only bring more cleaning energy, but also the challenges to the current power transmission system. The re-development and upgrade of current power transmission system is essential. The FFTS, as introduced above, is considered as one of the suitable candidates to integrate offshore wind power system to the main grid. Nevertheless, unlike the traditional HVAC transmission system or the popular HVDC technology which has already been well developed or has been deeply studied. However, there is a big research gap related to FFOWPS. A complete and in-depth research about FFOWPS is of great value in terms of both technical and economic modelling and analysis.

1.2 Research Objectives and Contributions

1.2.1 Research Aim and Objectives

Based on the literature review in Chapter 2, the research aim of the PhD project is to carry out a comprehensive stability analysis of FFOWPS and a techno-economic comparison with the other possible schemes. The objectives of this doctoral research can be concluded as follows:

- Provide the basic knowledge of power electronics applied to FFOWPS, which includes the system structure, working principles and control strategies of the wind generation system and the frequency converters.

- Design the control strategies for frequency converters to integrate with the wind generation system, and the conflict between control system from the wind generation and frequency converters should be avoid.
- Develop the EMT models of the studied power electronics with a single machine infinite bus (SMIB) structure for experimental simulation, to test system performances within the FFTS and validate the proposed control strategies.
- Develop a small signal model of the whole FFOWPS with mathematical effectiveness and satisfactory accuracy, which should consider the dynamic performance of all essential power electronic components within the system and be useful for small signal stability analysis.
- Carry out an economical and technical analysis and comparison among different offshore wind power transmission technologies to study the dominant cost of each power system and compare the pros and cons of each technology.

1.2.2 Research Contributions

The contributions of this doctorial research can be concluded as follows:

- Proposed a control strategy to integrate the wind generation system with the frequency converters smoothly, and the control conflict between the wind power system and the frequency converters has been avoided. The EMT models are developed to validate the proposed control methods and for further small signal stability analysis.
- A small signal model of DFIG-M^3C FFOWPS has been developed to fill the gap in the literature. The eigen-value based small signal stability analysis is provided to discuss the influence of the PI controller parameters and circuit component values. The optimised system is given out.

- A comprehensive eco-technical study of FFOWPS is provided. Two types of frequency converter are studied with the proposed economic analysis model, and the main cost elements are discussed. The comparisons between M^3C based FFOWPS and BtB-MMC based FFOWPS are provided from the economic aspect and the technical aspect, respectively.

1.3 Outline

Chapter 2 provides a literature review related to the study. The control strategies and applications of M^3C are reviewed first, then the basic theory of small signal stability is discussed in detail with the small signal modelling of wind generation system and multilevel converters. Finally, the economic analysis of FFOWPS is reviewed.

Chapter 3 deeply discusses the structure, working principles, and control strategy of the wind generation system and frequency converters. The EMT models are develop and the control strategy to connect wind generation and frequency converter are designed and validated with time domain simulation.

Chapter 4 proposes a small signal model of DFIG-M^3C based FFOWPS. The dynamics of the DFIG system are modelled first, and then the small signal model of M^3C with designed control strategy is introduced. Two systems are combined together, and an eigenvalue based small signal stability analysis is carried out. The influence of PI controller parameters and circuit elements is discussed, and optimised parameters are provided. An EMT model of FFOWPS has been developed for time domain simulation testing and validation.

Chapter 5 studies the economic aspect of the FFOWPS. The economic analysis model is designed and two different types of FFTS are discussed. The main cost elements of two systems are analysed and their total costs are compared under different case studies. A further technical comparison is provided with the EMT model time domain simulation.

Chapter 6 gives the conclusion of the thesis. The study outcomes are concluded and the possible further research directions are discussed.

The relationships between the chapters are as follows:

- Chapter 2 provides a literature review related to the study. Based on the literature review, research gaps are identified, and then the project aim and objectives are proposed.
- The Chapter 3 aims to establish the detailed EMT model for the whole system - FFOWPS. The collation of the knowledge, control strategy design, and testing system modelling for related power electronic provide the foundation for further studies in the rest of the chapters.
- Building upon the detailed EMT models of FFOWPS proposed in Chapter 3, Chapter 4 develops a small signal model of DFIG-M^3C based FFOWPS considering the dynamic responses of DFIG generator and M^3C response together. A small single stability analysis is carried out to study the impacts of PI controller parameters and system elements. The optimization of the system is provided based on the proposed small signal model.
- Based on the models and knowledge of all the previous chapters, Chapter 5 carries out comprehensive comparisons of the proposed FFOWPS with another scheme of BtB-MMC based FFOWPS.
- Finally, based on all these chapters, conclusions are drawn and future work is highlighted in Chapter 6.

Chapter 2 Literature Review

2.1 Introduction

This chapter provides the literature review of relevant technologies and research methods of this doctoral study. As the key component of the FFOWPS and a relatively new technology, the previous control strategies and applications of $\mathrm{M}^3\mathrm{C}$ are discussed first. Then the principle of small signal stability analysis is reviewed, and the modelling methodologies of wind power system and multilevel converters are reviewed. Finally, the economic analysis studies related to offshore wind power and related transmission technologies are reviewed.

2.2 Applications and Control strategies of $\mathbf{M}^3\mathbf{C}$

The $\mathrm{M}^3\mathrm{C}$ has been regarded as the next generation AC/AC converter, which was first introduced in 2001 [38]. As shown in Fig. 2.1, the configuration of $\mathrm{M}^3\mathrm{C}$ has evolved from the traditional matrix converter with a nine-swich matrix arm with the four-quadrant switch operation. The $\mathrm{M}^3\mathrm{C}$ applied with the IGBT full bridge submodules, which provide three different voltage levels during the switch conduction. The space vector modulation (SVM) control method is tested and validated to employ the converter, and the simulation is carried out on the $\mathrm{M}^3\mathrm{C}$ model with two submodules in each arm. After that, the $\mathrm{M}^3\mathrm{C}$ has been studied among different kinds of applications, and different control strategies have been proposed.

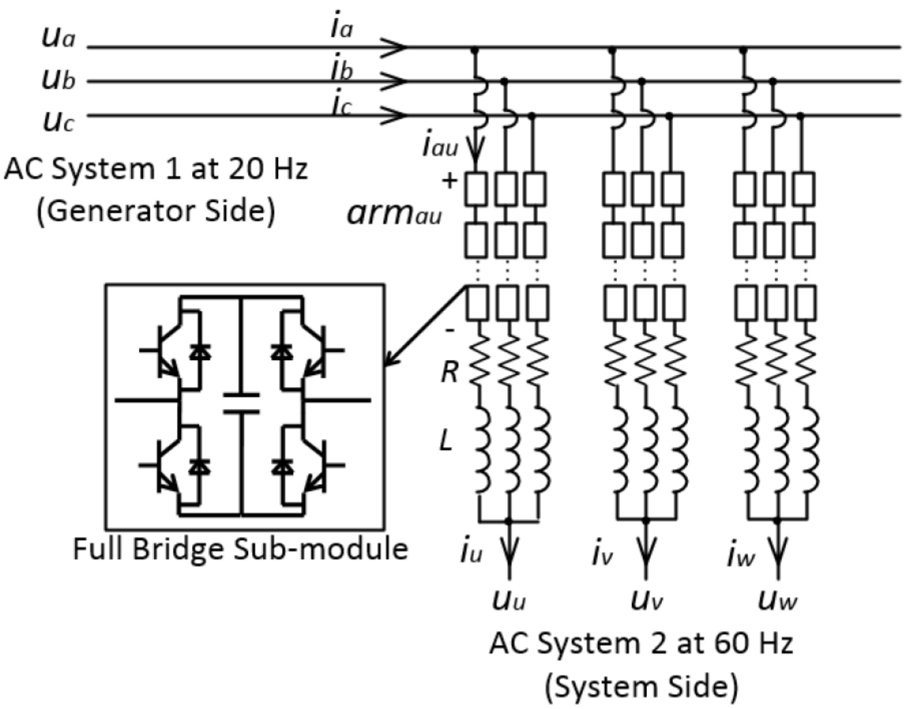

Fig. 2.1 Schematic diagram of M^3C [41]

2.2.1 Application of M^3C

Like other power converters, M^3C has been widely studied in aspect of motor driving [42, 43]. And with development of renewable energy, researches about wind power system integration are also provided [44]. Furthermore, it is known that the traction power system in Germany, Switzerland, Sweden, Norway and Austria also using the low frequency AC system on 16.7 Hz, and it is foreseeable that the M^3C could be applied in the railway sector to transfer regenerative braking energy thanks to its bidirectional operating ability [45, 46]. In [42], an optimised phase inductor design was proposed to lighten the weight and size of the M^3C. There are nine inductors inside M^3C originally for current control on each arm, and the author proposed a three legged, six winding inductors with zigzag wired to reduce the number of arm inductors to three. The new design ensured that no magnetic flux has been generated in the nine arms from the three phase source and motor currents. A downscaled motor-drive system has been built to validate the proposed design and the effectiveness has been proved. [43] presented a discussion about how to control the M^3C to employed as a medium voltage motor drived with regenerative braking. A decoupled current control was proposed to regulate the capacitor DC voltage of all submodules. And the performance of the control strategy was also validated with the experimental downscaled model.

Compared to driving the motor, the $\mathrm{M^3C}$ applied to wind power integration requires more submodules to meet the high voltage rating of the transmission system, and also the frequency from both sides should be controlled. Studies [47, 48] proved the operability of $\mathrm{M^3C}$ as the frequency converter for FFTS integration with the decoupled current control. However, the test system is simplified with only a very few submodules in each arm of $\mathrm{M^3C}$ and the wind power system is represented with a simple PQ source. Considering the growth size of the offshore wind power plant, the more realistic experimental systems and control strategies should be modelled and studied.

2.2.2 Control of $\mathbf{M^3C}$

Applied as the frequency converter for wind power integration applications, the control of $\mathrm{M^3C}$ is the main challenge. The SVM control method has been used in [49] to achieve the wide frequency conversion range of $\mathrm{M^3C}$ for FFTS. The experimental results proved the $\mathrm{M^3C}$ is able to operate without the circulating current control and provide a stable frequency conversion. However the test $\mathrm{M^3C}$ system only consists of three submodules inside each arm and considering the space vector used for control system is exponential increasing against the increasing of submodules, the SVM is not suitable for high voltage rating system with large number of submodules. [50] proposed a widely used decoupled current control. As there is no DC link inside the $\mathrm{M^3C}$, the voltage and current components with different frequencies are coupled with each other. The author presented a double $abc/\alpha\beta0$ transformation to achieve independent control for both sides of $\mathrm{M^3C}$ and balanced the internal current. However, after the double transformation, some components were still frequency related, which made it hard for control system design and small signal modelling. An improved version of this control strategy is proposed in [51]. The M^3C was divided into three sub-converters and the frequency related items can be converted to DQ axis as a DC signal and regulated under the synchronous rotating frames of these sub-converters. However the control method requires a number of frame transformation and interaction of different controllers, which will be a challenge when considering high volume of submodules. [52] proposed a vector control to provide the full range frequency conversion within the M^3C. A featuring frame transformation was applied to the arm voltage and current, and with essential filtering, the M^3C system was performed well over a wide range of frequencies, including the same input and output frequency mode. The effectiveness is validated by simulation based on a 27-cell 5kW prototype M^3C. However, to achieve the ideal results, system requires extra converter capacity.

In addition to the control strategies designed for frequency conversion, some research has been presented to optimise the performance of M^3C. A recent study [53] raised a concern that when M^3C applied with large number of submodules, the current centralised control structure may not be capable of its flexibility and modularity. The author proposed a distributed control mode by considering separating the current control loop and voltage control loop with a time-dimension decoupling method, which could reduce the communication delay of different control system. The effectiveness of proposed control structure is validated with an experimental model of M^3C. In [54], a sparse topology of M^3C has been proposed with an alternative structure of submodules. The system is designed with less components and the more than half of IGBT can operate with soft switching. The proposed structure is validated with the experimental model and simulation results. [55] considered the limitation of IGBT semiconductor current rating, and proposed a current reallocation control strategy to reduce the peak arm current of M^3C. It was proved by the simulation results that up to 14.6% - 21.6% of peak current could be decreased, which provided the enhancements to the M^3C like short-term overload rating and better fault ride through ability. In [44], the unbalanced grid conditions cased by single phase faults was discussed. With imbalanced power from the negative-sequence quantities was calculated and compensated by the designed feedforward control method, the M^3C system was functioned well under the unbalanced grid conditions. The proposed control strategy was verified by the experimental simulation. In [56], the further branch fault of M^3C was discussed. A optimised branch current configuration model was designed to deal with the one or more arms failure situation. The effectiveness of the proposed system is validated with the experimental M^3C prototype, which could be smoothly transformed from the full branch mode to a reduced operating mode while the branch failure happened without disabling the whole system. [57] considered the concern about frequency support of M^3C based wind power system. As introduced in Chapter 1, most wind conversion systems cannot support inertia to the power system, which caused the issue to the frequency response of the system. The proposed control strategy extracted the energy from the floating capacitors to serve the frequency response. However, as the energy from the floating capacitor is not much, the frequency support is limited.

From the research review introduced above, the control strategies proposed for M^3C are only consider M^3C itself. However, as the offshore wind power system integration technology, the interface between M^3C and wind generation system cannot be neglected. Studies [47, 51, 58] proposed related control strategies for low frequency offshore wind power system integration. However, the wind power system has been represented by a simple controllable current source within their study and the control system of wind generation has been ignored. As most renewable energy generations inherently are the voltage source converters, the interface of two converters may cause conflict. [59] proposed a constant voltage and frequency control for offshore wind farm integration with a VSC-HVDC. The proposed strategy operated the VSC converter as a voltage source with constant voltage magnitude and frequency, to naturally absorb the power from the wind farm without affecting the control system of the wind generator converter. The effectiveness of the proposed control scheme was validated by the experimental results. However, the control of M^3C is much more complicate than VSC due to its coupling frequency components. The control strategy for connecting M^3C to the DFIG system needs to be studied. The details of this work are discussed in Chapter 3.

2.3 Small Signal Stability Analysis and Modelling of FFOWPS

Since the 1920s, power system stability has been an enduring topic for secure system operation. The number of major system damages caused by system instability described the importance of this phenomenon [60]. And with the increasing penetration of renewable energy source, the power system stability faced an unprecedented challenge currently. The definition of the power system stability was proposed by the IEEE/CIGRE Joint Task Force in 2004. In general, the power system stability is the ability of the power system to regain the operating equilibrium after a physical disturbance. The Task Force also defined the classification of power system stability as follows:

- Rotor angle stability: it refers to the ability of the synchronous machine in an interconnected power system to recover from the subjected disturbance and back to synchronism. This stability problem is related to the electromechanical oscillations problem in the power system.
- Frequency stability: it refers to the ability of the power system to remain frequency stable after a significant power flow imbalance. The frequency stability problem may cause a sustained frequency swing and eventually trip the generations or loads.
- Voltage stability: it refers to the ability of the power system to maintain voltage at a steady level of each bus after introducing a disturbance. The instability of the voltage

may result in loss of loads in an area or triggering the system protective operation to cascade the transmission line and other elements.

The rotor angle stability can be refined into two subcategories:

- Small signal stability: this stability problem is concerned the steady state of power system or system ability to maintain synchronism with small disturbances. The disturbances should be small enough so the system equations can be linearized for further analysis [61].
- Transient stability: this stability problem is related to the ability of the power system to keep stable after a large disturbance, for instance, a short circuit fault. This problem involves the large excursions of generations and influences by the nonlinear dynamics relationship of power system. It depends on the initial operating conditions of the system and the seriousness of the fault.

This study was mainly focused on the small signal stability of the FFOWPS. The analysis of such stability problem can help studying the dynamic performance of the system and provide guidance to system designs, which is quit useful for new developed power system. The fundamental theory and analytical methods of small signal stability analysis is discussed in next subsection.

2.3.1 Fundamental of Small Signal Stability Analysis

The small signal stability of the power system can be influenced by system initial operating conditions, the control devices, and the strength of power connections electronic components [62]. As the practical power systems are unavoidably suffered small disturbances, it is essential for the power system maintain stable in term of small signal stability problems. System with small signal stability problem can be explained as a lack of damping ability against the oscillations. It is important to define the electromechanical oscillation modes of the system during the small signal stability analysis. The oscillation modes can be classified as follows [62]:

- Local modes: they are also named as machine modes, are related to the swing of the machine in one area to the rest power system. They are normally located at single station or small group of power system.
- Inter-area modes: they are normally a concern of the swing of the generator among the group located closely and link by a weak grid [63].
- Torsional modes: they are raised from the shaft system between the turbine and the generator unit and normally oscillated within a 10-50 Hz range.
- Control modes: they are involved with the exciters and speed governors within the generators, or the controllable power electronic devices and components. They are normally oscillated above 50 Hz and are the main oscillation modes to be discussed in this thesis.

The small signal stability of power systems is normally studied by the eigenvalue based analysis and frequency domain analysis, and the eigenvalue based analysis, is currently the most popular analytical method. It is derived from the Lyapunov stability theory about the linear system [62]. The basic theory is to linearize the dynamic power system from its nonlinear differential equations around a stable operating point. The analysis procedure is introduced as below.

The dynamic power system can be represented by the nonlinear model described as:

$$\dot{x} = Ax + Bu \tag{2.1}$$

$$y = Cx + Du \tag{2.2}$$

where x are the state vectors of the system; u are the system input variables; y are the system output variables. A and B represented the state variables matrix and control variables matrix, respectively. C and D represented the output variables matrix and feedforward variables matrix, respectively.

The state variables of the system can be defined in different ways as long as they can represent the system dynamics. The order of the system is decided by the number of state variables. The nonlinear model (2.1) and (2.2) can be linearized around an equilibrium point where all the derivatives equal to zero, and all variables are referred to the initial states. Then (2.1) and (2.2) can be derived as:

$$\Delta\dot{x} = A\Delta x + B\Delta u \qquad (2.3)$$

$$\Delta y = C\Delta x + D\Delta u \qquad (2.4)$$

where Δ is a small deviation of the variables from the equilibrium point.

Apply the Laplace transform to (2.3), the characteristic of the state variables matrix A can be calculated from:

$$\det(sI - A) = 0 \qquad (2.5)$$

where s are the eigenvalue from the state variables matrix. Based on the Lyapunov's theory, the system small signal stability can be determined by the locations of the eigenvalues. The rule is described as follows:

- System is small signal stable when all real parts of eigenvalues are negative.
- System is small signal unstable when at least one real part of eigenvalues is positive.
- System small signal stability cannot be determined when eigenvalues have zero real part.

The eigenvalue can be expressed as:

$$\lambda = \sigma \pm j\omega \tag{2.6}$$

The real part σ indicates system damping, while imaginary part ω determines oscillation frequency. It is given by:

$$f = \omega/2\pi \tag{2.7}$$

The rate of decay of the system can be represented by the damping ratio, which is given by:

$$\xi = -\sigma/\sqrt{\sigma^2 + \omega^2} \tag{2.8}$$

The mode is defined as poor damped while the damping ratio is less than 5%. In that case, system may have small signal stability concerns. The participation factor of each mode can be calculated from the left and right eigenvector, which determines the main contribute state variables to the oscillation modes.

2.3.2 Small Signal Modelling of Wind Power Systems

Wind energy is regarded as the most widely utilised renewable energy source cross the world. With the increasing share of wind generation system against the traditional power system, the system stability will be affected because of the poor inertia support ability of the wind system. Due to inherently different between the wind power plant and conventional power system. It is necessary to study the small signal stability of wind power system. The first step is to establish the small signal model.

As introduced in last chapter, currently the most widely used wind turbines are the fixed speed wind turbine SCIG and variable speed wind turbine DFIG. A simple model was proposed for the fixed speed wind turbine to discussed the dynamics of wind power system [64]. [27] provided the transient stability studies with a reduced-order model of SCIG. In [65], the modelling of large capacity fixed speed wind turbined based wind farm was proposed. For DFIG system, a detail engineering model of DFIG with its back-to-back PWM converter was described in [66]. A simple DFIG model was proposed in [67] for the grid integration impacts studies. [68] developed a dynamic model of DFIG with the relevant control and protection elements for transient analysis. In [69], a reduced order model of DFIG including its converter was provided.

Based on the knowledge about the modelling of the wind generators, the research works were pushed further to the small signal stability analysis. The full small signal model of the DFIG including the control systems of converter were presented in [70, 71], and related small signal stability analysis was provided for system optimization and control parameters selection. The proposed optimized system was validated by the simulation result. The impacts of different wind turbines to the power system was studied in [72] based on the small signal stability analysis. The conclusion is that the constant speed wind turbines offers better damping ability than the variable speed wind turbines. [73] studied the damping performance of different type of wind turbines integrated into the Nordic grid using the eigenvalue analytical method. It was found the SCIG has positive impact on the damping of inter-area oscillation while the DFIG has negative performance. In [74] a inertia sensitivity eigenvalue analysis is proposed to study the small signal stability and transient stability of DFIG within a large system. It was found increasing the number of DFIG wind turbines has both positive and negative impacts to the system damping.

It can be found from the studies reviewed above that the small signal model of DFIG has been well studied, and the impacts of DIFG to the power system has been discussed. However, the dynamic performances of DFIG system combined with other power electronics in small signal stability aspect have not attracted many attentions, which still needs to be studied.

2.3.3 Small Signal Modelling of Power Converters

The converters have been widely used for different applications in power system. Based on the conversion type, it can be categorized as AC/DC converter such as Static Synchronous Compensator [75], AC/DC/AC converter used for HVDC system [76], and AC/AC converter for FFTS [21]. The AC/DC/AC converter can also be configured as back-to-back structure for wind energy conversion [77] or FFTS integration [36]. A multilevel static synchronous compensator small signal model was provided in [78], and a new feedback control method to balance the dc capacitor voltage is proposed based on the model. The small signal model of a single machine infinite bus with the VSC based HVDC system was studied in [79]. Based on the small signal stability analysis, the open loop system has poor performance on stability, and a damping controller is designed to VSC-HVDC to improve system performance. The effectiveness of the proposed controller was validated in both eigenvalue analysis and time domain simulation. In [70], the back-to-back AC/DC/AC converter of DFIG system was modelled for small signal stability analysis. The vector-based control systems were also modelled and the impacts of controller is studied. The small signal model of a cycloconverter based FFTS was proposed in [34]. Through the small signal stability analysis, it was found the cycloconverter has detrimental impacts on system damping and a feedback PI controller was designed to solve the problem. The effectiveness of the controller was validated, however, the cycloconverter was simply represented by a first order time delay model and the dynamics of the converter were ignored. The interface between the converter and wind system was unable to be studied. With the efforts of the researchers, the small signal model of MMC are available. It was firstly evolved from the VSC model with neglecting the internal dynamic of MMC and assuming the internal damping of MMC is satisfied [80]. And the improved model was provided in [81] with the internal dynamic components modelled. It considered only the DC component of the circulating current and ignored the frequency components with the assumption of the frequency circulating current component could be remained at the steady state with the proposed controller. However, when MMC subjected to a small disturbance, the power components inside the arm were coupled with the circulating current and the dynamic of circulating controller should be considered. The small signal model provided in [82] included this part of work. The circulating current suppression control is modelled and the capacitor voltage ripper also studied in a double system frequency DQ frame. Due to the scalability of MMC, the number of the submodules could be very large and each submodule component could be considered as a state variable for the small single model. It should be reasonably when choose the state variables to ensure the system accuracy and also mathematical effectiveness.

It can be found from that there are some commonalities among different type of converters. The modelling of M^3C can borrow some experiences from MMC models considering they are both multilevel converters, but there are also some fundamental differences that M^3C has no DC link and the different frequencies power quantities from both sides of M^3C are merged together inside the converter arm. The isolation and modelling of that dynamic components needs to be studied. A small signal model of M^3C was introduced in [41] to fulfil these requirement. The model considered the dynamics performance inside the converter arm, and the decoupling control system was modelled to isolate the frequencies components. However the small signal only considered the M^3C itself, and the external AC system was modelled with a simal voltage source. The integration of M^3C to offshore wind power system still needs to be studied.

2.4 Economic Analysis of FFOWPS

Many technologies were firstly introduced with excellent performance, however, the economic cost determined the further development of these technologies. The illustrative diagram of a general FFOWPS is shown in Fig. 2.2. As a relatively new technology, the economic aspect of FFOWPS needs to be studied. The cost analysis studies related to offshore wind power system and the transmission technologies are provided in this section.

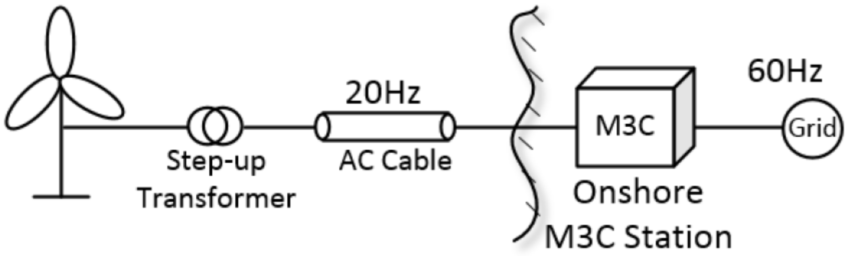

Fig. 2.2 Illustrative diagram of FFOWPS [41]

2.4.1 Economic Analysis of Offshore Wind Power System

The renewable power generation costs has been studied and published annually by the International Renewable Energy Agency [83]. It provided the transparent details related to the cost of renewable energy so that the academic, industrial and market can have a distinct view at the economic aspect of renewable energy. The latest report [83] pointed out the share of offshore wind energy among the world power capacity is remaining the growing trend, while the cost for offshore wind power reduced again and will remain the fall trend. That is due to reasons of development of technologies, experiences from previous projects, and a more competitive equipment price.

In [84], the basic cost components of offshore wind farm was reviewed based on the data available in the bibliography, which is useful for payback analysis and cost optimized studies. However some regression curves are drawn based on the assumption data and the applied technologies was not analysed. [85] studied the opportunities to integrate energy storage device with the large-scale wind farm into the future Netherland power grid. Different types of energy storage technologies was studied based on a cost-benefit analysis method and the CO_2 emission impact was accounted. It was found the cost savings from storage device increase with the number of wind turbine installed, but it is hard to have the payback due to the large initial investment. And considering the energy storage devices are allowed to absorb the cheap fuel generation energy in Dutch power system, the CO_2 emission levels will increased and even with the wind power integration, it will partly offset the CO_2 emission saving from wind farm. [86] proposed an opportunity to produce hydrogen by using the wind power in a microgrid considering the variation of wind power output. Based on the economic analysis model, the breakeven period was found to be 15.58 years and the hydrogen cost is 17.65 $/kg. The results varied against the wind power price and hydrogen price but the proposal is viable with the development of renewable energy. [87] further studied the cost effectiveness of proposal that producing the hydrogen using the wind power. It was found the cost of hydrogen is much affected by the balance between the rating of wind power generation and hydrogen generation, due to the mismatch of the power between two systems made the energy price uncompetitive. A optimal configuration of the system is designed based on the economic analysis. The economic analysis of a hybrid system was provided in [88]. The wind-solar combined system is studied to power the AC and DC irrigation pumps. The optimal arrangement of the wind-solar capacities are proposed based on the analysis results that the AC pump is uneconomic against the DC pump. In [89], a fully review of the economic and technic analytical methods for hybrid renewable system was presented. Author compared and summarised the differences of 31 computer tools and 20 arithmetical models to give a clear view to the researchers. In [90], four general economic analysis methods were introduced as shown in Table 2.1. Based on the results from the analysis methods, the optimal generation capacity and hub height were choosen for the wind farm to improve economic effectiveness.

TABLE 2.1 GENERAL ECONOMIC ANALYSIS METHODS

Economic analysis methods	Contents
Simple payback period method	• Equals to the capital cost divided by the average annual income • Determine the breakeven period
Cost of energy (COE) method	• Determine the unit cost of energy generation • For comparison between different energy generation.
Discounted cash flow (DCF) method	• Calculate the value of the money paid now and received future • Focused on the time preference of money
Life-cycle costing (LCC) method	• Calculate the present value of the project take account the future cost and time value of money • Determine the feasibility of the project from available choices and technical parameters

2.4.2 Economic Analysis of Transmission Technologies

As introduced in last chapter, the distance of new developing offshore wind to the coast are in growing trend, and the transmission technologies to transmit power from the far ocean needs to be studied. In [91], the transmission technologies HVDC and HVAC were compared in economic aspect for offshore wind power integration. Based on the study, the HVDC had advantages in long distance transmission and the cost effectiveness cross point of two transmission system among the distance was calculated based on the economic analysis model. It was found the difference is more obvious when considering the large-scale wind power system. The cross point of distance for two transmission system is 160km for a 1 GW offshore wind plant. A further economic analysis between two type of transmission line was presented in [92], which considered the operation and maintenance (O&M) cost and energy waste cost. Based on the case study, the strength of HVDC technology appeared on transmission distance longer than 90km. However the system capacity is only considered for 200 MW and 500MW, which may not suitable for future large scale wind farm plant.

Limited attentions has been paid to the FFTS in economic aspect. [93] studied the differences among HVAC, FFTS and HVDC technologies for offshore wind power integration in economic area. The cost effectiveness of each technology was calculated based on different scenarios and the most economical choice was provided. However, the system model of HVDC is too simple and some of cost factors like the O&M and power loss were not considered. In [94] a more detail economic analysis model was provided for FFTS and the conclusion is that FFTS is a suitable choice for offshore wind farm with 200MW capacity and located 100km to the coast. But the frequency converter in this study was considered as the cycloconverter, which, as mentioned above, is not suitable for FFOWPS.

2.5 Summary

This chapter has reviewed the technologies related the FFOWPS. The M^3C is the key component of the FFOWPS and is a relatively new developing technology, hence the application and control of M^3C has been reviewed first. It has been found the M^3C is capable of integrating the offshore wind power system, however, the control strategies of M^3C to interface with the wind power system still needs to be studied, which will be discussed in Chapter 3. The small signal stability problem is an enduring topic of the power system. The fundamental of small signal stability analytical methods and small signal modelling of related technologies have been reviewed. It can be found there is a lack of small signal stability analysis of the M^3C based FFOWPS in literature. The detail small signal stability study related to DFIG-M^3C based FFOWPS is presented in Chapter 4. Technologies may have outstanding functionalities, but the economic cost determined whether it can be applied into the practical power system. The previous economic related knowledge of offshore wind power and transmission system technologies have been studied at the end of this review. Different cost analysis method related to offshore wind power can be found in the literatures, however, considering the integration of the relatively new FFTS and M^3C, the cost analytical model needs to be studied. Chapter 5 provides the discussion related to this aspect.

Chapter 3 EMT Simulation Models of FFOWPS

3.1 Introduction

This chapter aims to discuss the system structures, operating principles and control strategies of the key components the FFOWPS: the wind generation system and the frequency converter. Chapter 2 has reviewed different technologies for FFTS. The DFIG based wind power system is considered in this study due to its low cost, high power transfer efficiency and flexible controllability. Another important component of FFOWPS is the AC/AC converter, or the frequency converter. M^3C is a new generation of AC/AC converter, with the advantages of full controllability and high power quality. It is a promising technology to integrate wind farm from offshore to onshore. To avoid the conflict of the control system between wind power system and frequency converter when connecting them together, a constant voltage and frequency control strategy is designed to M^3C system. Another AC/AC converter technology, the BtB-MMC is also introduced and discussed in this chapter for further comparison study against M^3C system in Chapter 5. The EMT models have been developed for each technology to test systems performance for FFOWPS and validate the proposed control strategies. The main contributions of this chapter are listed below:

- The system structure, working principle and general control strategies of DFIG, M^3C and BtB-MMC are introduced;
- The control strategies to integrate the frequency converters with the DFIG system are designed to avoid the conflict between different control systems;

- The EMT models of all the system components are developed and the SMIB time domain simulations are presented to test systems performance and validate proposed control strategies.

The knowledge presented in this chapter constructures the foundation of the Chapter 4 and Chapter 5.

3.2 Dynamics of DFIG for FFOWPS

The DFIG is considered in this study due to the fact that it is a popular technology with its high power transfer efficiency, low cost and flexible controllability. The output power frequency of DFIG is defined by the gear box of wind turbine. It can generate low frequency power with a small ratio gearbox or even without gearbox for FFTS, which makes it a good candidate for FFOWPS. A EMT simulation model of DFIG is designed for the generated fractional frequency power at 20 Hz for FFOWPS, which is discussed in details in the rest sections.

3.2.1 Operating Principle and System Structure

A DFIG based wind power system is shown in Fig. 3.1. System consists of the induction machine, driven train, back-to-back converter and its controller. The power generated from the induction can be fed to grid by both stator and rotor windings. System can be controlled by the small capacity converter as the power transmitted through the converter is only 20% - 30% of the rating power of generator. The wind power capture by DFIG wind turbine depends on the wind speed and its rotor speed. The aerodynamic power of wind is given by:

$$P_{WF} = \frac{1}{2}\rho C_p A V_w^3 \tag{3.1}$$

where P_{WF} is the captured wind power; ρ is the air density; A is the rotor swept area; V_w is the wind speed; C_p is the power coefficient.

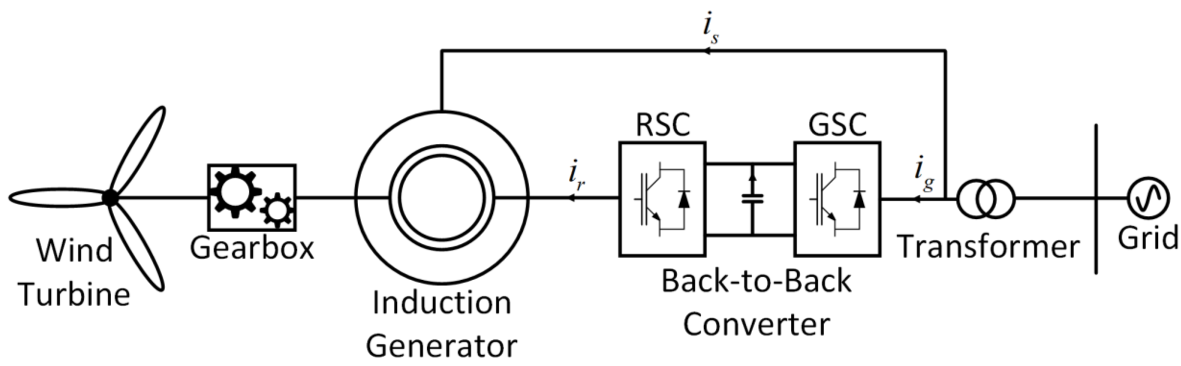

Fig. 3.1 Structure of DFIG-based wind turbine

The relationship between rotor speed and wind speed can be expressed as:

$$\lambda = \frac{\omega_t R}{V_w} \tag{3.2}$$

where λ is the blade tip speed ratio; ω_t is the rotor speed; R is the wind turbine blade radius.

The maximum power coefficient C_p can be achieved by controlling the rotor speed, then the maximum captured wind power is given as:

$$P_{WF\_max} = \frac{1}{2}\rho C_{p_{max}}\left[\frac{R}{\lambda_{max}}\right] A V_w^3 \tag{3.3}$$

As mentioned above, the power from DFIG wind turbine delivered to grid through both stator and rotor winding. When system operated under steady state, the power transmitted through the DFIG is shown as Fig. 3.2. For simplified, this relationship ignores the stator and rotor power loss.

Fig. 3.2 Power transmitted through DFIG

The power relationship can be expressed as:

$$P_{WF} = P_s + P_r \tag{3.4}$$

The relationship between rotor power P_r and stator power P_s is depended on the slip ratio of DFIG, which can be expressed as:

$$s = (\omega_s - \omega_r)/\omega_s \tag{3.5}$$

Where ω_s is the synchronous speed and ω_r is the rotor speed. The relationship between rotor power and stator power can be expressed as:

$$P_r = -sP_s \tag{3.6}$$

3.2.2 Control Strategy Designed for FFTS

The decoupling control strategy is widely used for controlling the back-to-back converter. With implementing the DQ transformation on the current and voltage quantities of two sides of converter, the active and reactive components of both sides can be decoupled and controlled separately. For DFIG system, the rotor-side converter (RSC) aims to control the active power or electromagnetic torque and reactive power from the generator side. Under the DQ frame, the active power or electromagnetic torque is proportional to and controlled by Q quantities of rotor current and voltage, and the reactive power is proportional to and controlled by D quantities of rotor current and voltage. The grid-side converter (GSC) aims to maintain the DC-link voltage and regulate the reactive power of grid side terminal. It is controlled by the grid current and voltage quantities. With implementing the DQ transformation, the DC-link is proportional to and controlled by D quantities of grid current and voltage, and the reactive power is proportional to and controlled by Q quantities of grid current and voltage.

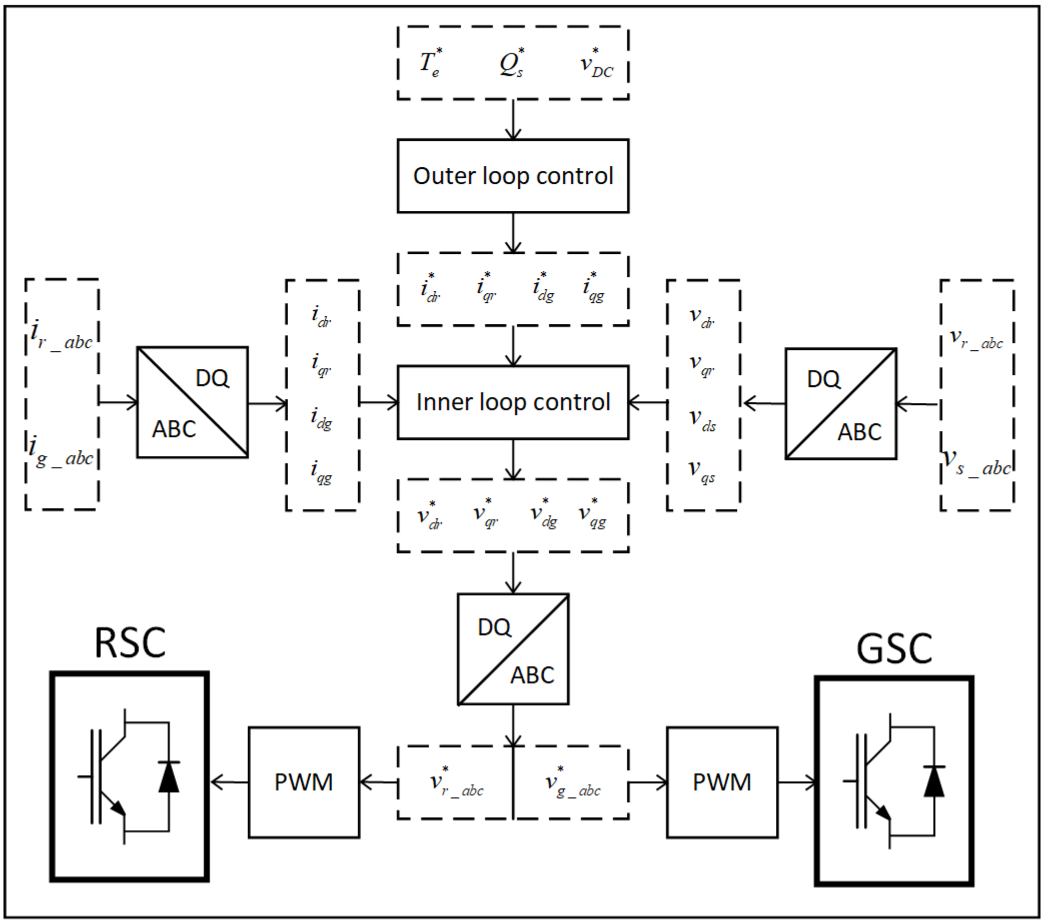

Fig. 3.3 Control diagram of back-to-back converter

The schematic diagram of the control strategy for back-to-back converter of DFIG is shown as Fig. 3.3. For RSC control, the electromagnetic torque reference T_e^* is achieved from the maximum power tracking point (MPTT), and the reactive power reference Q_s^* can be set to a constant value or zero depends on different situation. The PI controller is applied to the outer loop control to achieve the reference rotor current signal, and also applied to the inner loop control to regulate the rotor current. The output reference rotor voltage signal is transformed back to ABC frame and sent to the pulse width modulation (PWM) generator, and the control signal for RSC can be achieved. For GSC control, the reference for DC-link voltage depends on the size of the back-to-back converter and modulation factor, and the reference of reactive power of the terminal normally set to zero. Same as the RSC control, the GSC also applies the cascade control. The outer loop control use PI controller regulating the DC-link voltage to achieve the reference gird current signal, and the inner loop control regulate the grid current signal via PI controller. The output reference grid voltage signal is transformed back to ABC frame and sent to PWM generator, and the control signal for GSC can be achieved.

3.2.3 EMT Model and SMIB Simulation

A single machine detailed model of DFIG is developed in MATLAB/Simulink for EMT simulation. The MATLAB/Simulink is a powerful simulation software which can not only implementing power system simulations, but also capable of a large contents of system simulation and analysis in engineering domain. The Simulink simulation can also be supported by the MATLAB script and user-defined function which give it more flexibility to study new system. The rest of the frequency converter are also modelled on the MATLAB/Simulink and the further small signal stability analysis is implemented by using the MATLAB script.

The structure of DFIG is shown in Fig. 3.1. The simulation system is built as a single machine system, with the DFIG directly connected to the grid via a transmission line. The AC grid is modelled as a three-phase constant voltage source. For further study purpose, the whole system is modelled as a 20 Hz fractional frequency system. The DFIG system generated 1.5MW power with 0.575 kV rating voltage. The transformer steps up voltage to 120 kV and transmit it to the grid. Full system detail parameters can be found in Appendix A. The controller of the system is build based on the control strategies introduced in last section. The PI controller and PWM generator model from MATLAB/Simulink library are used. The tuning of primary PI controller parameters is based on general rules. Higher proportional parameter helps system react quicker to the steady state error, but cannot totally remove steady state error, and the error overshoot will also be increased, which will push system poles to the positive panel. The integral gain improves controller performance against steady state error, but will slow the reaction of controller. A further controller parameters optimization will be discussed in Chapter 4. The DFIG model developed in this subsection will be used for further discussion in Chapter 4 and Chapter 5 to integrate with frequency converter models.

The terminal voltage and current at steady state is shown as Fig. 3.4. As figure shown, the waveforms of voltage and current are ideal sinusoidal with only 0.13% Total harmonic distortion (THD) in voltage and 0.45% in current, which are far below the 5 % IEEE standard

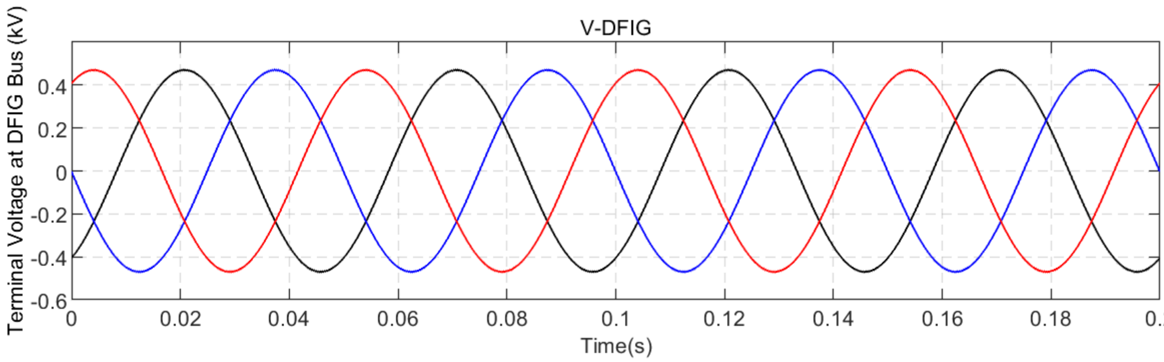

(a) Terminal Voltage at DFIG Bus

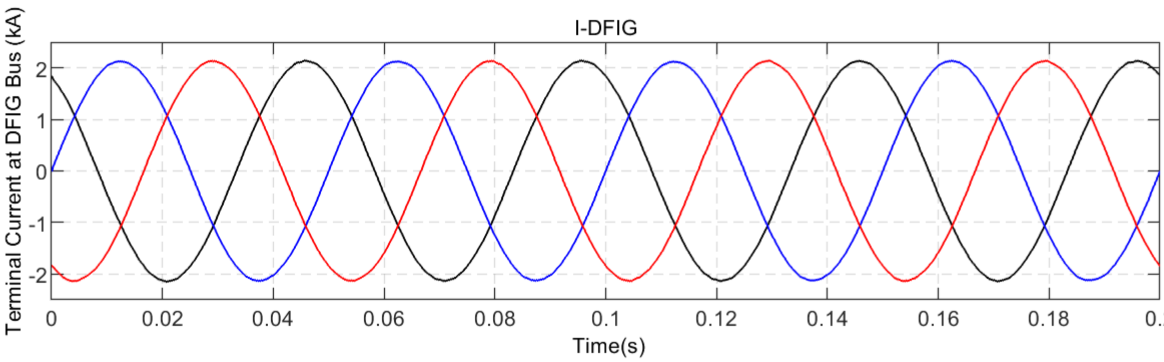

(b) Terminal Current at DFIG Bus

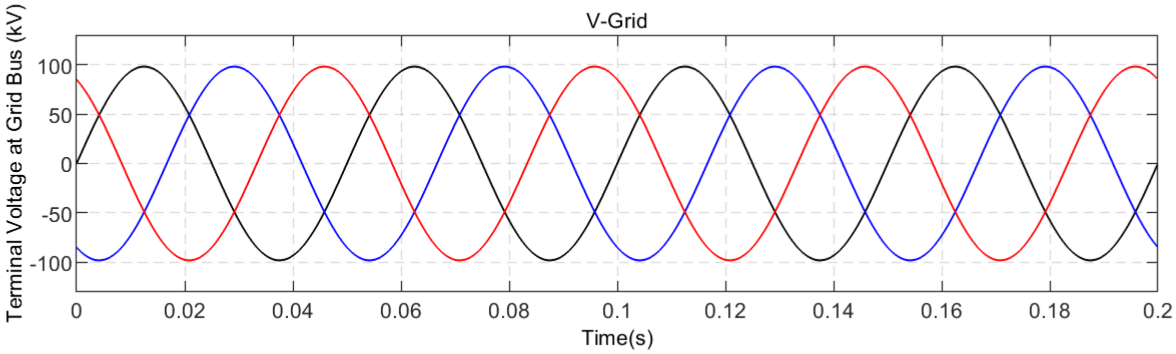

(c) Terminal Voltage at Grid Bus

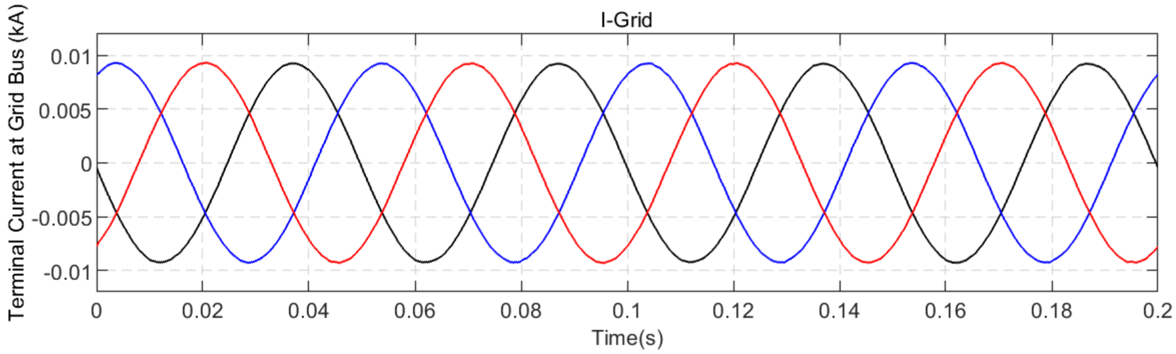

(d) Terminal Current at Grid Bus

Fig. 3.4 Terminal Voltage and current waveforms of DFIG

The DC-link voltage and active power transmitted to grid is shown as Fig. 3.5. The voltage ripple of DC-link voltage is only 0.3% and the oscillation on active power waveform are also negligible.

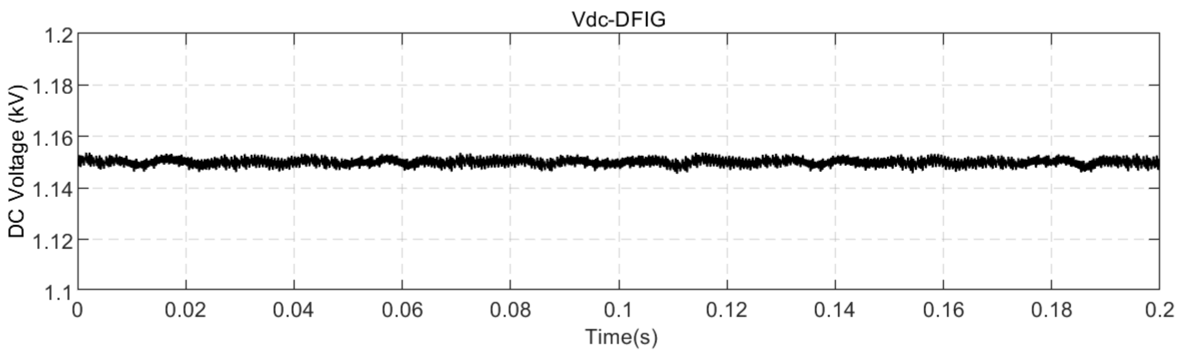

(a) DC link Voltage

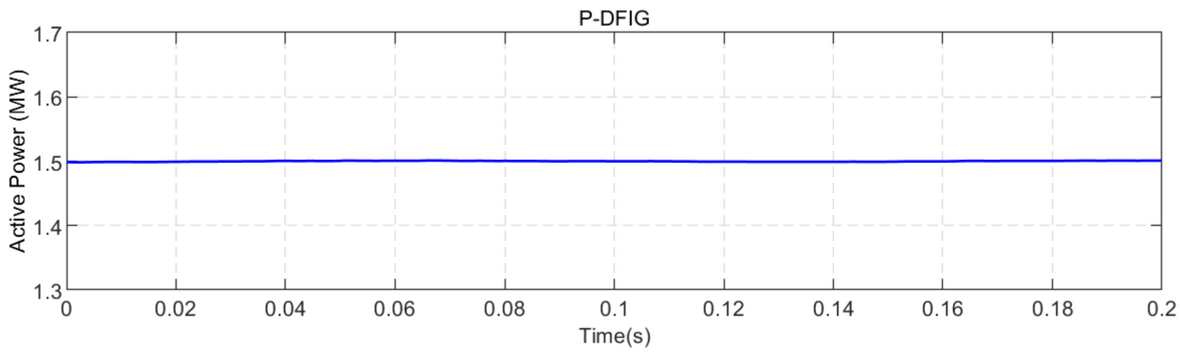

(b) Active power

Fig. 3.5 DC link Voltage and active power of DFIG

A 0.1 pu step change of electromagnetic torque reference is applied on the control system of DFIG. The active power step change simulation result is shown in Fig. 3.6. As figure shown, the active power tracked on the reference signal, which validates the satisfactory performance of the controller. The further controller improvement for Electromagnetic torque reference step change will be discussed in Chapter 5.

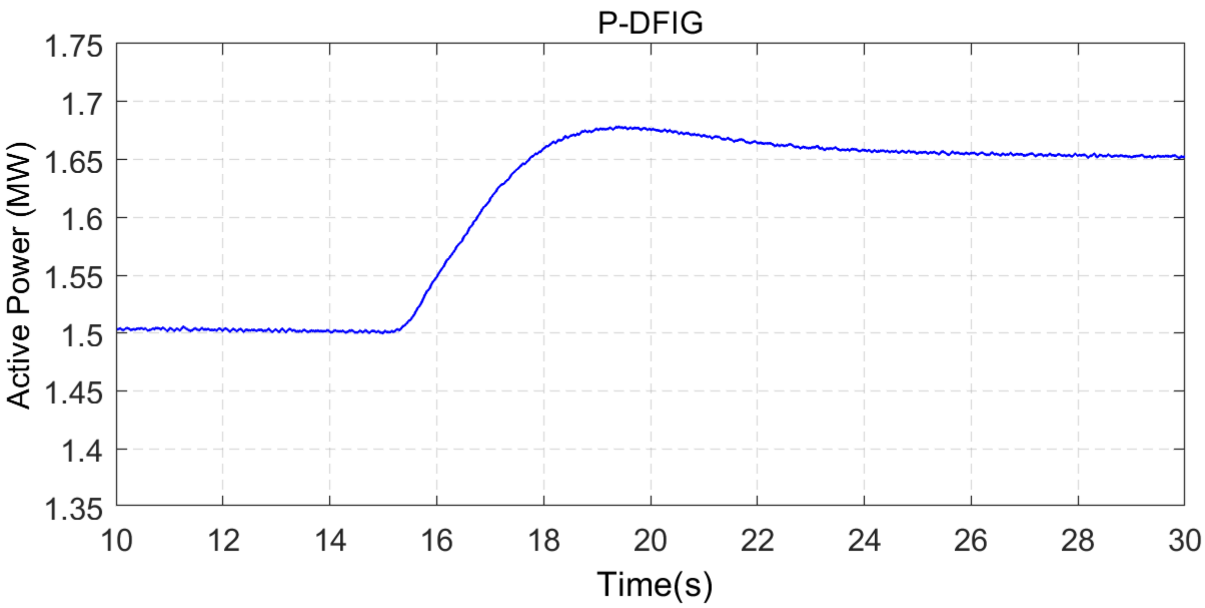

Fig. 3.6 DFIG Active Power Step Change

3.3 Dynamics of M^3C for FFOWPS

As discussed in Chapter 2, thanks to its full controllability and high power quality, M^3C system is a suitable technology to integrate the offshore wind power system. In this section, the operating principle and system structure of M^3C is introduced first in following subsection. Then, the control strategy of M^3C is discussed and a constant voltage and frequency control method is designed to connect M^3C to the offshore wind power system. A EMT time domain simulation model is developed and simulated to validate the designed control strategy and the performance of M^3C for FFOWPS. The M^3C model developed in this section will be further served in Chapter 4 for constructing the DFIG-M^3C based FFOWPS.

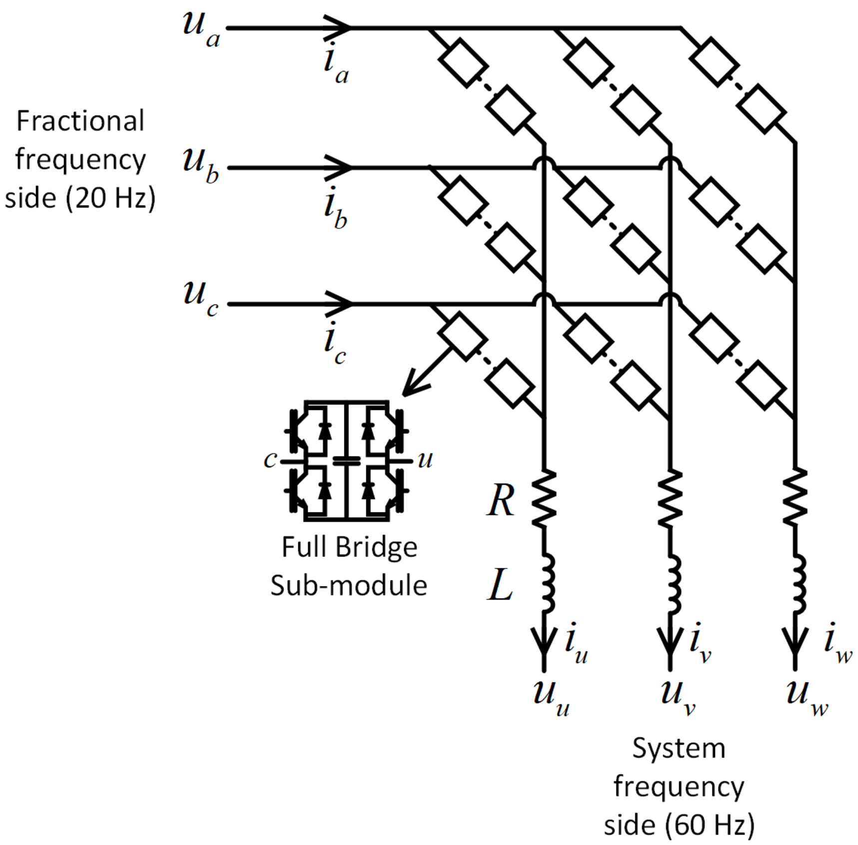

Fig. 3.7 Structure of M^3C

3.3.1 Operating Principle and System Structure

The topology of M^3C is shown in Fig. 3.7. Basically, it is a three phase AC/AC matrix converter. The voltages u_a, u_b, u_c, represent the three phase on the fractional frequency side, while the u_u, u_v, u_w refer to the three phase on the system side. Currents of two sides represented by same subscripts and the direction is as shown in Fig. 3.7. In the middle is the nine arms of M^3C, and each arm consist of N series sub-modules and an arm inductor L. The resistor R refers to converter losses.

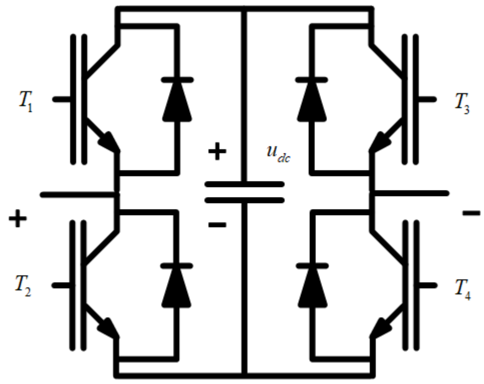

Fig. 3.8 Full Bridge Sub-Module

The sub-module can be presented by an IGBT based full bridge with a capacitor as the dc voltage source, as shown in Fig. 3.8. The combination of the switch on and off decides how the sub-module operated. In specifically, the sub-module is operated under positive insertion mode with switches T_1 and T_4 on, T_2 and T_3 off. Similarly, the sub-module is operated under negative insertion mode with switches T_2 and T_3 on, T_1 and T_4 off. The sub-module will be bypassed with either switches T_1 and T_3 on, or T_2 and T_4 on. When turning off all switches, the sub-module will be blocked. Table 3.1 summarises the operation modes of sub-module. With different switching signal inserted ($S_{arm} = 1, 0, -1$), the sub-modules can output three voltage levels: $\pm u_{dc}$ and 0.

TABLE 3.1 FULL BRIDGE SUB-MODULE OPERATION MODES

Operation Mode	T_1	T_2	T_3	T_4
Positive Insertion	ON	OFF	OFF	ON
Negative Insertion	OFF	ON	ON	OFF
By Pass	ON	OFF	ON	OFF
	OFF	ON	OFF	ON
Block	OFF	OFF	OFF	OFF

Under normal operation mode, the sub-module of each arm is inserted in a certain direction. n represents the number of inserted sub-modules, and C represents the capacitance of sub-module capacitor, the arm current can be expressed by:

$$n\, i_{arm} = NC\frac{du_{dc}}{dt} \tag{3.7}$$

Define $S_{arm} = \frac{n}{N}$, (3.7) becomes:

$$i_{arm} = \frac{1}{S_{arm}}C\frac{du_{dc}}{dt} \tag{3.8}$$

This research is focused on developing a general FFOWPS small signal stability analysis model under balanced steady state. The $\mathrm{M^3C}$ is assumed working under balanced state. The $\mathrm{M^3C}$ and MMC-HVDC share the same sub-module voltage balancing method which has been discussed and validated in [95]. Fig. 3.9 shows the block diagram of the voltage balancing method for each arm.

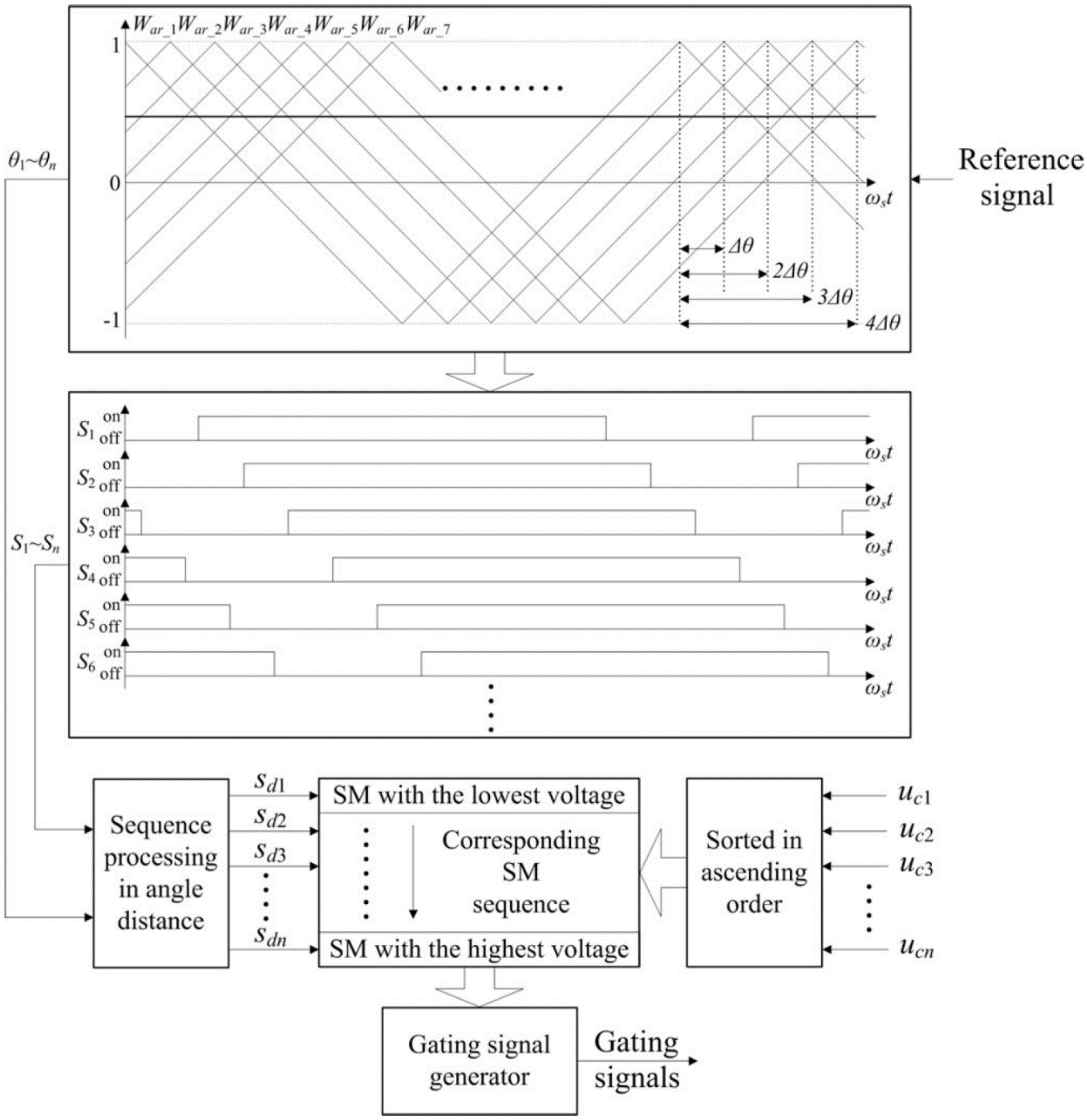

Fig. 3.9 Block diagram of voltage balancing control for each arm of the M^3C [95]

With the balanced sub-module voltages, the arm voltage can be expressed by:

$$u_{arm} = NS_{arm}u_{dc} \tag{3.9}$$

Under the balanced steady state, the AC currents spreads equally into three arms. The currents of fractional frequency side (20 Hz) and system frequency side (60 Hz) couple inside the M^3C. If we ignore the current harmonics, then the arm current i_{au} can be expressed as:

$$i_{au} = I_a\, sin(\omega_1 t + \beta_1) + I_u\, sin(\omega_3 t + \beta_3) \quad (3.10)$$

where I_a and I_u are a third of AC phase currents magnitudes of fractional frequency side and system frequency side, respectively; ω_1 and ω_3 are angular frequencies of both sides, respectively; β_1 and β_3 are current phase angles of both sides, respectively. And the arm switching function can be expressed as:

$$S_{au} = \frac{E_a}{U_{DC}} sin(\omega_1 t + \alpha_1) + \frac{E_u}{U_{DC}} sin(\omega_3 t + \alpha_3) \quad (3.11)$$

where E_a and E_u are the magnitudes of modulation voltages at fractional frequency side and system frequency side, respectively; α_1 and α_3 are the voltage phase angles of both side, respectively; U_{DC} is the total arm capacitor DC voltage.

3.3.2 Control Strategy Designed for FFTS

There is no DC link inside M^3C and the quantities from two frequencies side are mixed. This subsection will introduce the decoupling control for M^3C to extract the two frequencies items. The fractional frequency side of M^3C is set to 20 Hz and is designed to control the active power and reactive power at low frequency terminal. The system frequency side of M^3C is set to 60 Hz and is designed to maintain the capacitor DC voltage and reactive power at high frequency terminal. Based on the structure of M^3C shown in Fig. 3.7, and consider M^3C operated under balanced steady state, the voltage equation of nine arms can be expressed as follow:

$$u_a = v_{au} + \left(R + L\frac{d}{dt}\right) i_{au} + u_u \quad (3.12)$$

$$u_a = v_{av} + \left(R + L\frac{d}{dt}\right) i_{av} + u_v \quad (3.13)$$

$$u_a = v_{aw} + \left(R + L\frac{d}{dt}\right) i_{aw} + u_w \quad (3.14)$$

$$u_b = v_{bu} + \left(R + L\frac{d}{dt}\right) i_{bu} + u_u \quad (3.15)$$

$$u_b = v_{bv} + \left(R + L\frac{d}{dt}\right) i_{bv} + u_v \quad (3.16)$$

$$u_b = v_{bw} + \left(R + L\frac{d}{dt}\right) i_{bw} + u_w \quad (3.17)$$

$$u_c = v_{cu} + \left(R + L\frac{d}{dt}\right) i_{cu} + u_u \quad (3.18)$$

$$u_c = v_{cv} + \left(R + L\frac{d}{dt}\right) i_{cv} + u_v \quad (3.19)$$

$$u_c = v_{cw} + \left(R + L\frac{d}{dt}\right) i_{cw} + u_w \quad (3.20)$$

The items v_{xy} and i_{xy} represent the coupled arm voltage and current included two frequencies quantities. To extract the different frequencies components, the $\alpha\beta 0$ transformation is applied. The 60 Hz components can be extracted from the $\alpha\beta$ components, for instance, $v_{a\alpha}, v_{a\beta}$ *and* $i_{a\alpha}, i_{a\beta}$. And 20 Hz components can be extracted from the 0 components, for instance, v_{a0} *and* i_{a0}. Implemented a further d-q transformation to the $\alpha\beta 0$ components, the DQ components of $\alpha\beta$ items can be used for vector control on 60 Hz side, while the DQ components of 0 items can be used for vector control on 20 Hz side. The voltage relation of two sides can be expressed as:

$$E_{d20} = U_{d20} - \left(R + L\frac{d}{dt}\right) I_{d20} + \omega_1 L I_{q20} \quad (3.21)$$

$$E_{q20} = U_{q20} - \left(R + L\frac{d}{dt}\right) I_{q20} - \omega_1 L I_{d20} \quad (3.22)$$

$$E_{d60} = -U_{d60} - \left(R + L\frac{d}{dt}\right) I_{d60} + \omega_3 L I_{q60} \quad (3.23)$$

$$E_{q60} = -U_{q60} - \left(R + L\frac{d}{dt}\right) I_{q60} - \omega_3 L I_{d60} \qquad (3.24)$$

The items with 20 subscript are 20 Hz components and with 60 subscript are 60 Hz components. However, in order to connect the M^3C to the DFIG system, the control system conflict should be avoided. As discussed in last section, the RSC of DFIG also control the system active power, in that case, the fractional frequency side of M^3C should operated as a constant voltage source to absorb the energy transferred from the DFIG. The constant voltage and frequency control is designed for this case. Fig. 3.10 shows the proposed control strategy for M^3C system.

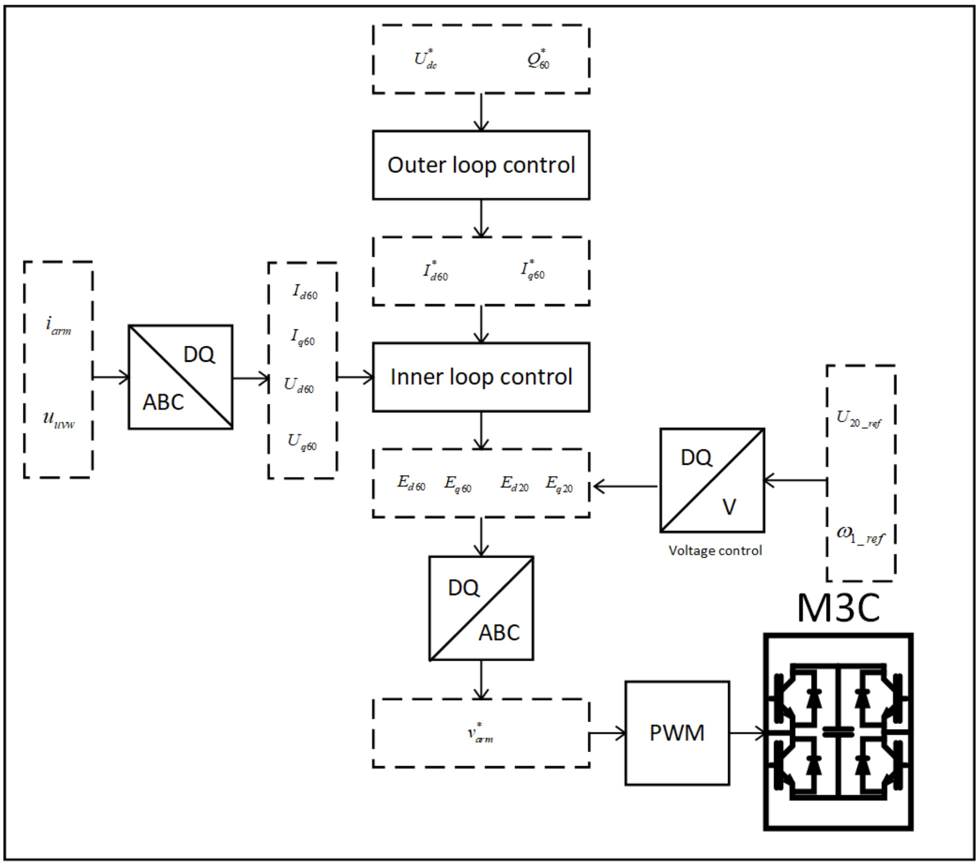

Fig. 3.10 Control Strategy of M^3C

3.3.3 EMT Model and SMIB Simulation

To test the proposed M^3C system, a detailed EMT model is developed using MATLAB/Simulink. The modelled system is a single machine system. The structure of M^3C

is shown in Fig. 3.7. Each arm of M^3C consists of 40 submodules. The submodule is modelled with the build-in full bridge MMC model from MATLAB/Simulink library. The external AC systems of the two frequencies sides are simply represented by two voltage sources. The power is transmitted from 20 Hz side to 60 Hz side. Full technology details of the system are listed in Appendix A. The system are test with the original vector control and designed constant voltage and frequency control. The simulation results are introduced as follow.

With vector control system, the terminal voltages and currents the of M^3C two sides are shown in Fig. 3.11. As figure shown, the voltage and current waveforms are ideal sinusoidal with the defined frequencies. For 20 Hz side, the THD of voltage and current are 0.42% and 1.39%, respectively; for 60 Hz side, the THD of voltage and current are 0.21% and 0.23%, respectively.

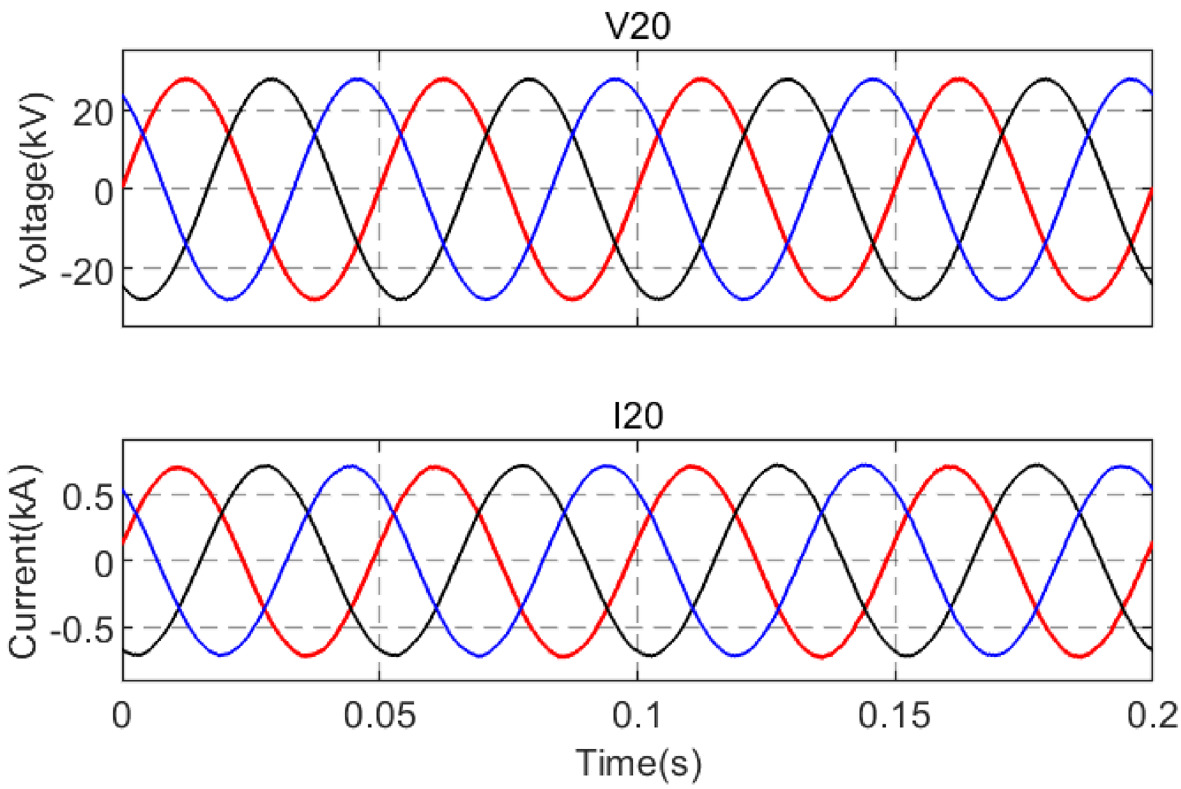

(a) Terminal Voltage (up) and Current (down) at 20Hz Side

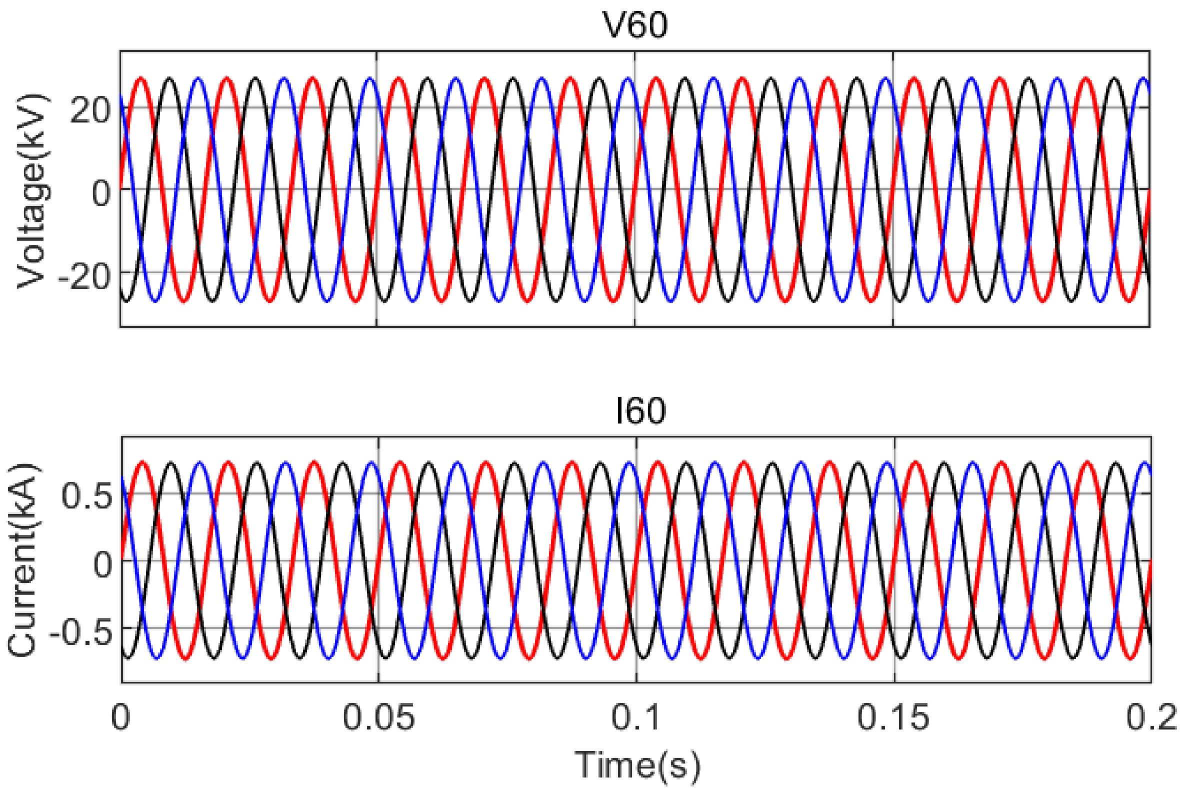

(b) Terminal Voltage (up) and Current (down) at 60Hz Side
Fig. 3.11 Terminal Voltage and current waveforms of M^3C

The arm voltage and current waveforms of M^3C with vector control are shown in Fig. 3. 12. As the figure shown, the waveforms are the coupled components of 20 Hz and 60 Hz sinusoidal waveform. It also can be seen the waveforms are in good quality. Overall, the voltage and current profiles of modelled M^3C are satisfactory and the performance of M^3C as the frequency converter is successful.

The method to extract the 20 Hz components and 60 Hz components from the coupled arm voltage and current has been discussed in subsection 3.3.2. With implementing the $\alpha\beta 0$ transformation, the 20 Hz components can be achieved from 0 components while the 60 Hz components can be achieved from $\alpha\beta$ components. Fig. 3.13 shows the isolated voltage quantities.

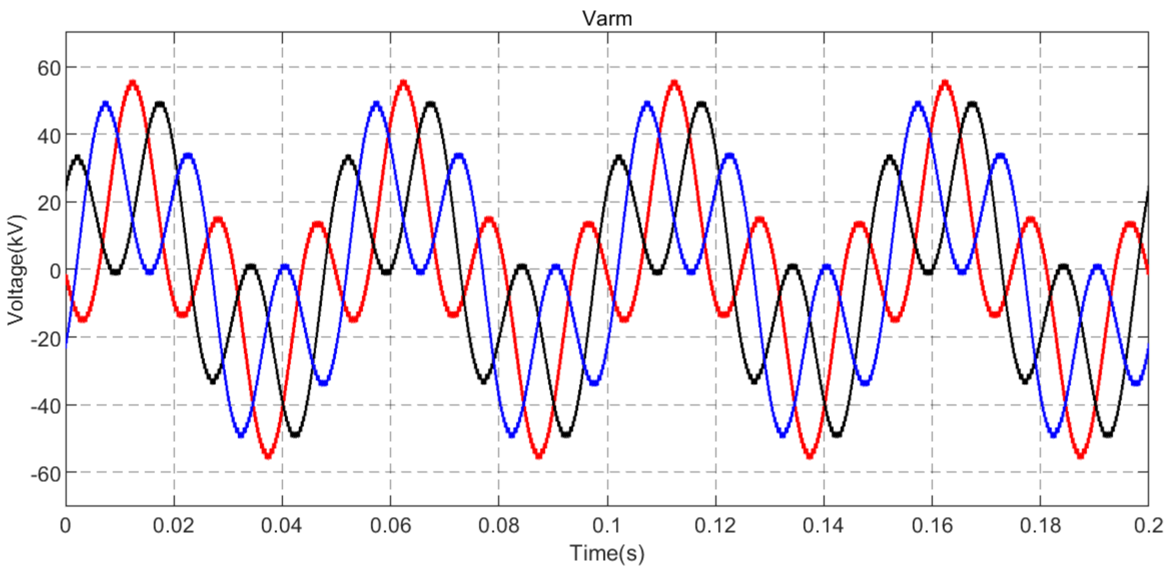

(a) Arm Voltage of M^3C

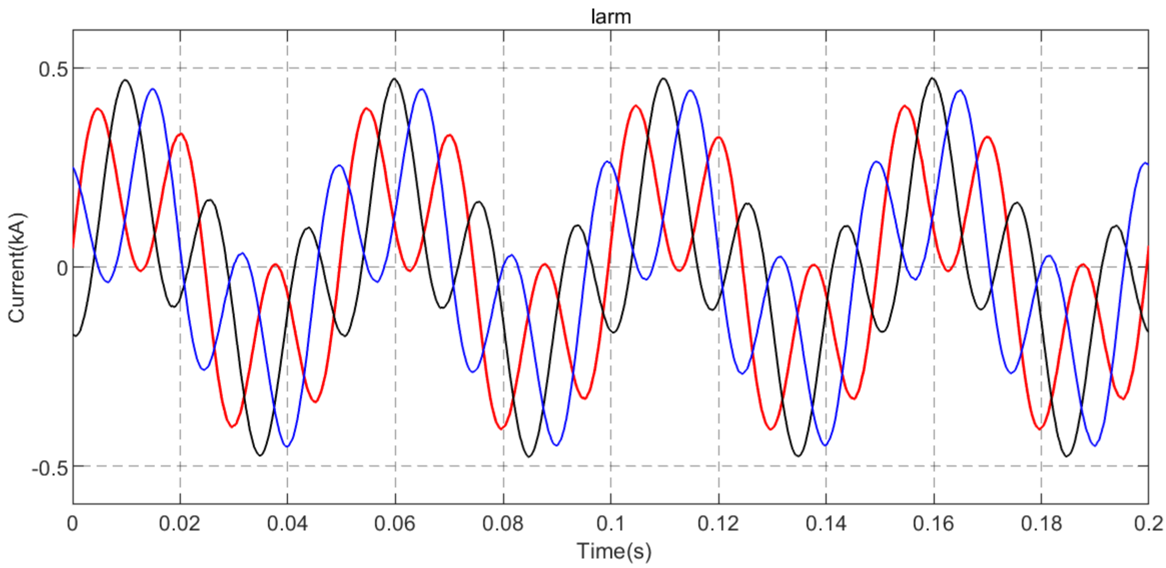

(b) Arm Current of M^3C

Fig. 3.12 Arm Voltage and Current Waveforms of M^3C

It can be seen from Fig. 3.13 (a) the $\alpha\beta$ components of arm voltage are in sinusoidal 60 Hz. And the 0 components of arm voltage are in sinusoidal 20 Hz, as Fig. 3.13 (b) shown. The current components have same performance which are not repeated shown.

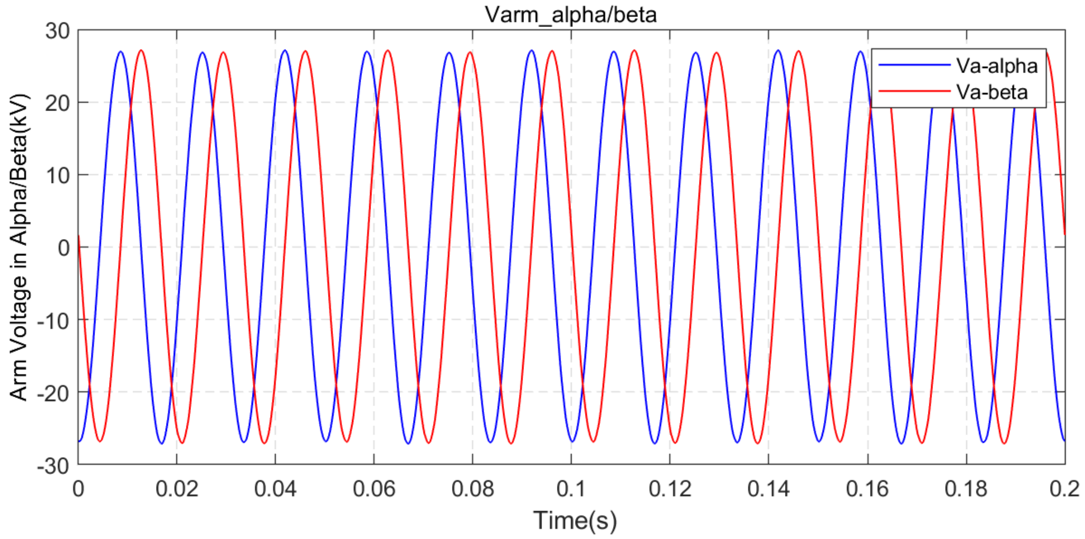

(a) Alpha and Beta Components of M^3C Arm Voltage

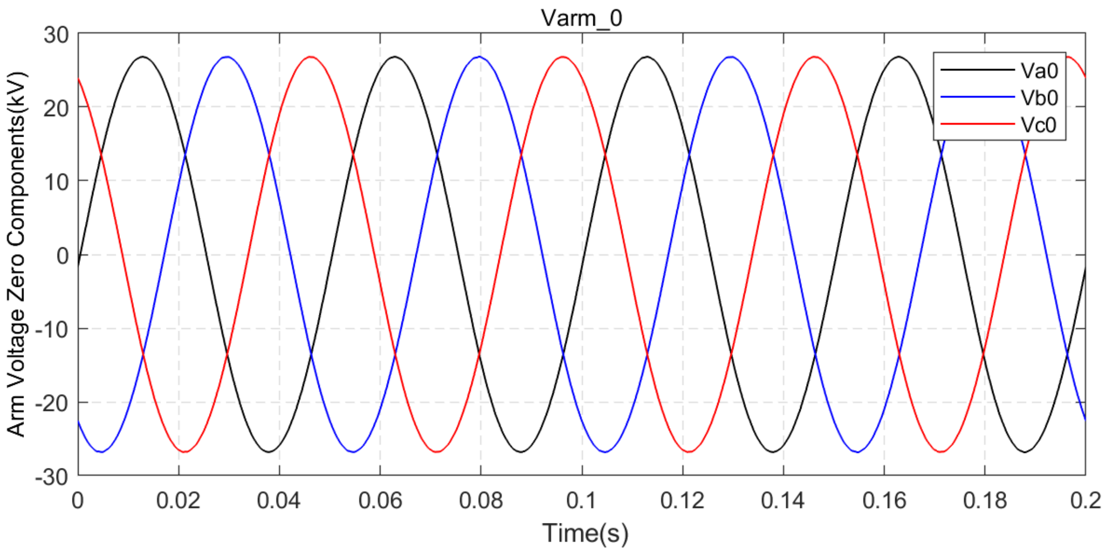

(b) Zero Components of M^3C Arm Voltage

Fig. 3.13 M^3C Arm Voltage Components after $\alpha\beta 0$ Transformation

Fig. 3.14 shows the terminal voltage and current waveforms of the two frequencies sides of M^3C with constant voltage and current control. As discussed in above subsection, to avoid the control conflict between DFIG and M^3C, the M^3C system operated as a voltage source and the active power of M^3C are not controlled. The simulation results presented below show the performance of proposed control strategy.

As shown in Fig. 3.14 (a), the voltage waveforms in 20 Hz side are in good performance while the current waveforms are relatively bad and the magnitudes are very small. That is due to the lack of active power control, and current external AC systems are modelled with a simple voltage source. Fig. 3.14 (b) shows the 60 Hz side waveforms which have the same performance. The simulation results validate the expectation of the proposed control strategy as the M^3C supposed to work as a voltage source with the constant voltage and frequency control implemented, and the active power should not be controlled.

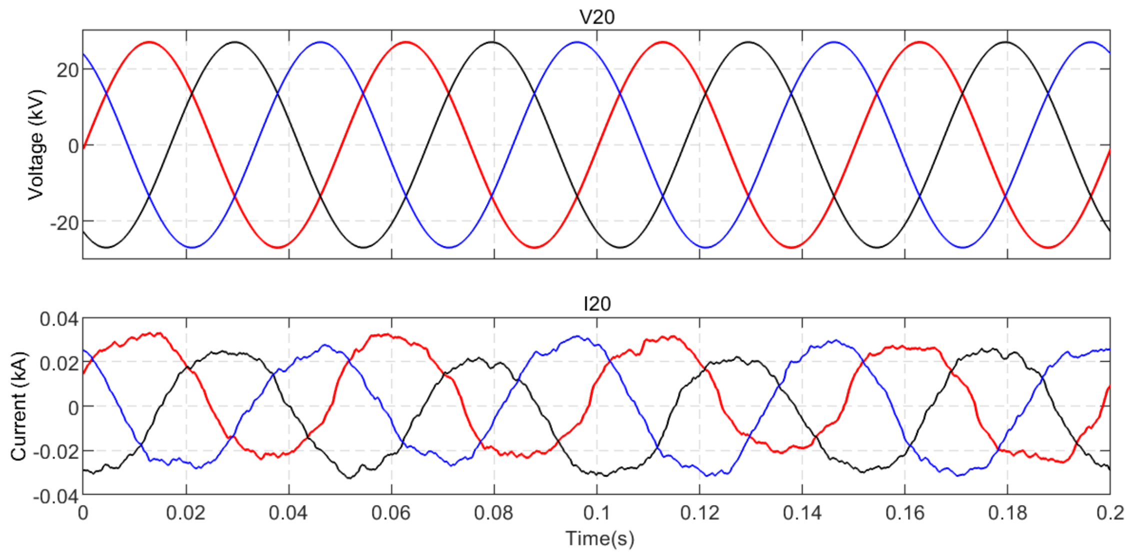

(a) Terminal Voltage (up) and Current (down) at 20Hz Side

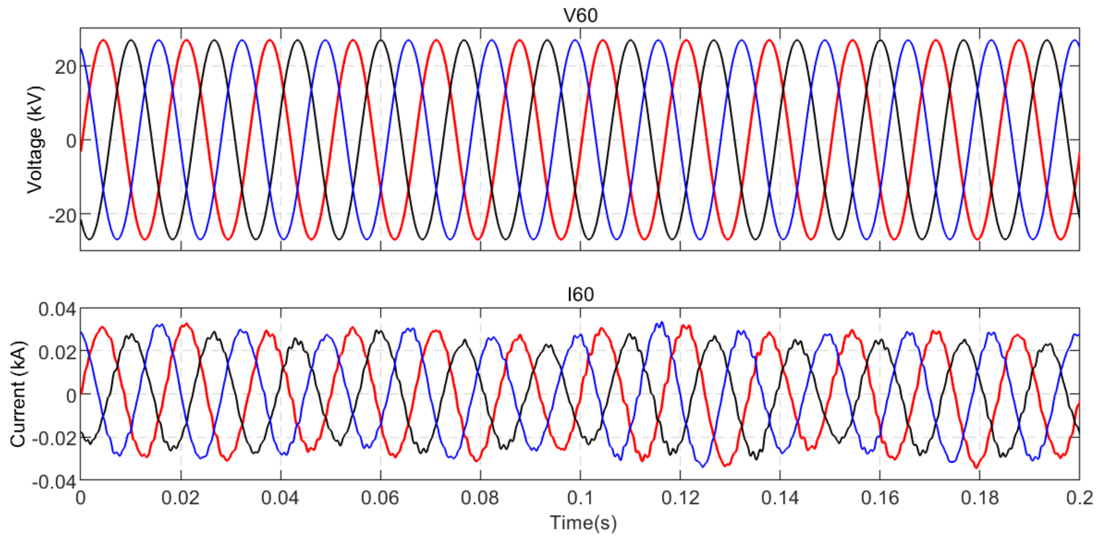

(b) Terminal Voltage (up) and Current (down) at 60Hz Side

Fig. 3.14 Terminal Voltage and Current Waveforms of M^3C

The arm voltage and current waveforms are shown in Fig.3.15. Same as the terminal voltages and currents, the arm voltage waveform performance are also in high quality while the current waveform reflect the situation that the active power of M^3C is not in control.

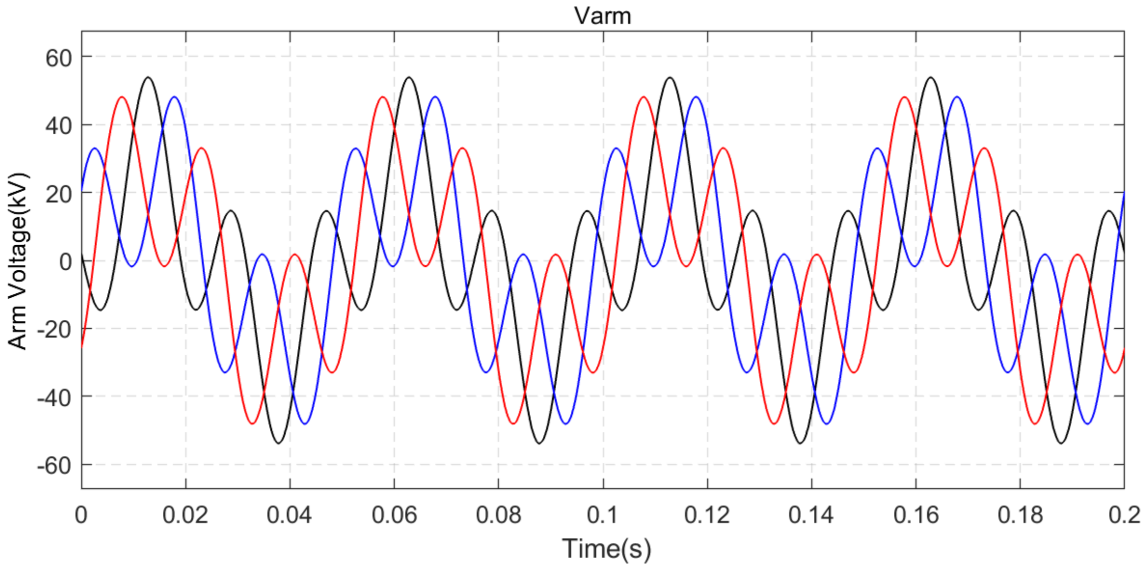

(a) Arm Voltage of M^3C

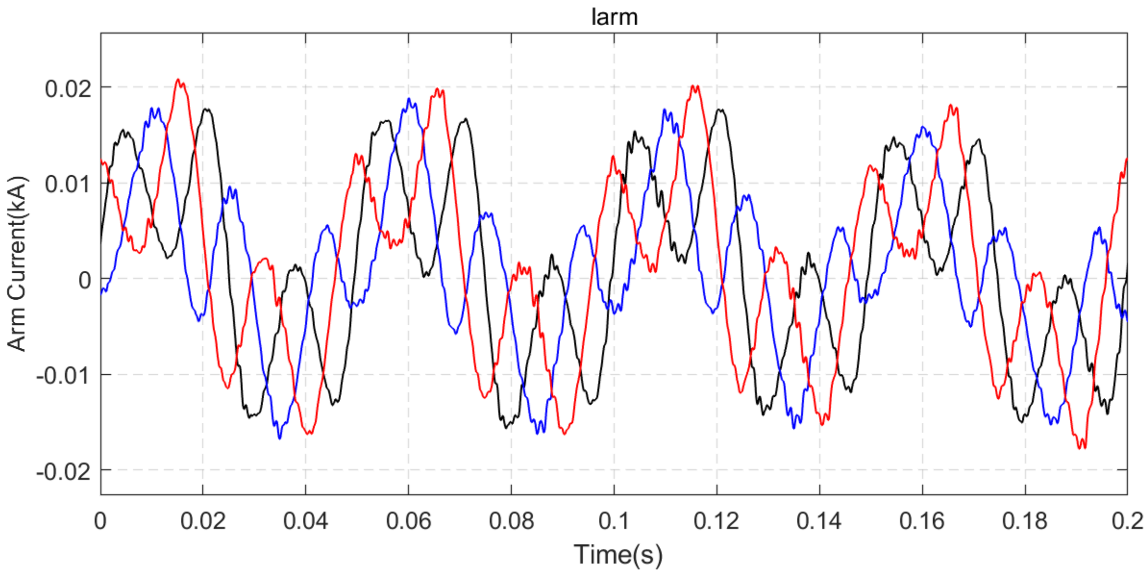

(b) Arm Current of M^3C

Fig. 3.15 Arm Voltage and Current Waveforms of M^3C

The further discussion and validation of proposed control strategy will be provided in Chapter 4 with the DFIG and M^3C system integrated. With DFIG system controls active power, the M^3C can absorb the power from the DFIG smoothly with the proposed constant voltage and current control strategy.

3.4 Dynamics of BtB-MMC for FFOWPS

The MMC-HVDC technology has been studied and practically implemented for years, which has been considered as a mature technology for power transmission system. The BtB-MMC is considered as an appropriate candidate for the LFAC system as the frequency converter, which is a good choice to be studied as a reference subject against the M^3C system. In this section, the operating principle and system structure of the BtB-MMC will be briefly introduced. The designed constant voltage and frequency control strategy discussed in last section is also implemented in the low frequency side of the BtB-MMC system. A EMT time domain simulation model is developed to examine system performance for LFAC system integrated. The model developed in this section will be further served in Chapter 5 for the comparison study between M^3C based FFOWPS and BtB-MMC based system.

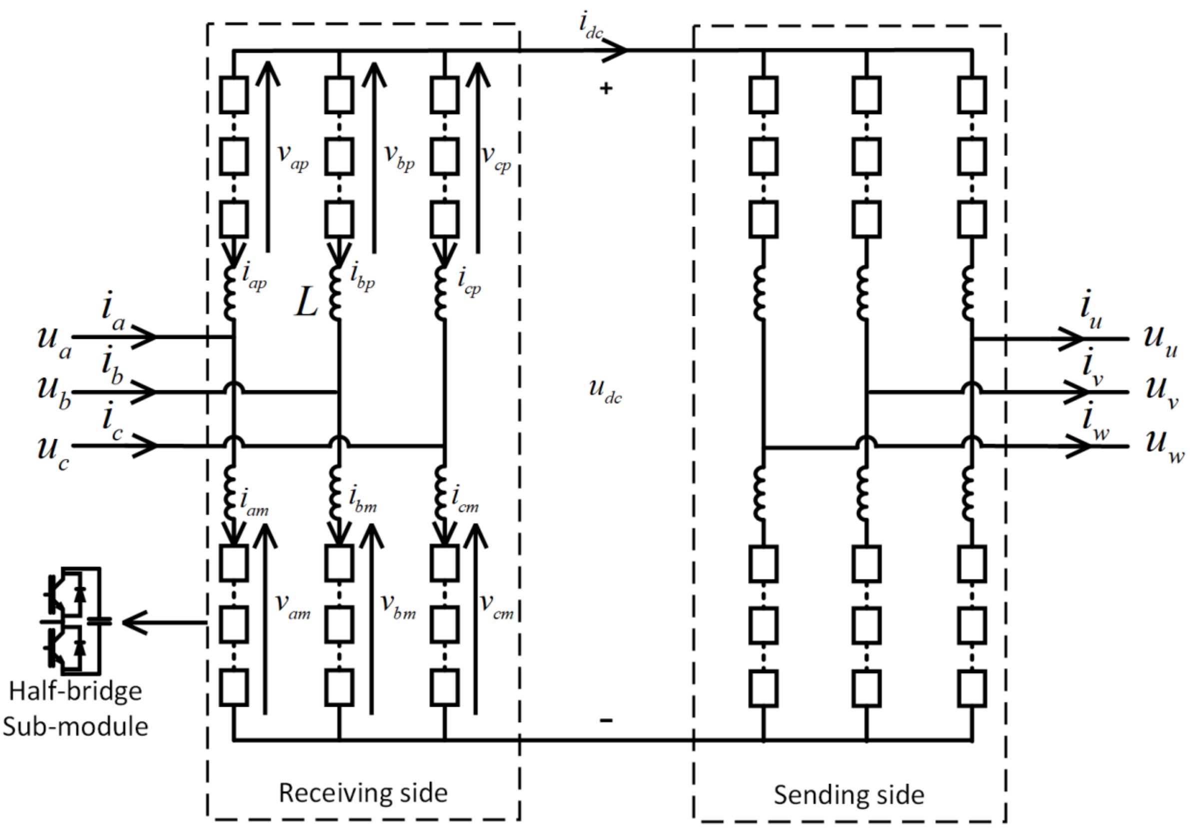

Fig. 3.16 Schematic diagram of BtB-MMC

3.4.1 Operating Principle and System Structure

The structure of the BtB-MMC is shown in Fig. 3.16. It is formed with the receiving side and sending side. Both side are of the same configuration. The receiving side work as the rectifier to transfer AC components to DC, while the sending side work as the inverter to transfer DC components back to AC. Each side consists of 6 arms and each arm composed of a number of sub-modules. The sub-module consists of two IGBTs switches with two freewheeling diode installed in anti-parallel and a dc capacitor, which is so called half-bridge sub-module, as shown in Fig. 3.17.

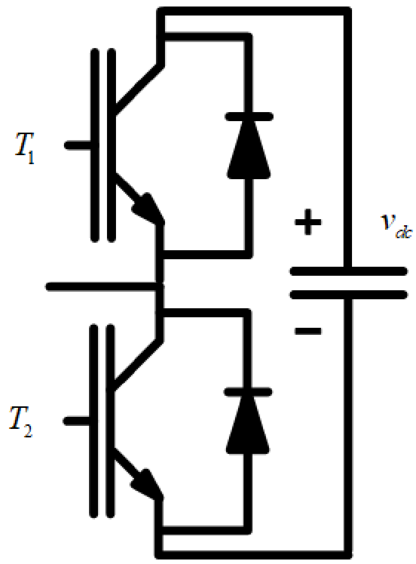

Fig. 3.17 Schematic diagram of half-bridge sub-module

The sub-module is activated when T_1 switch on and swich T_2 swich off, the charge and discharge of capacitor depends on the direction of arm current. To be specify, with T_1 switch on and swich T_2 swich off , when T_1 is conducting, the capacitor discharged, and when the anti-parallel diode conducting, the capacitor charged. Table 3.2 summarises the operation mode of sub-module.

TABLE 3.2 HALF BRIDGE SUB-MODULE OPERATION MODES

Operation Mode	Arm current	T_1	T_2
Charge	POSITIVE	ON	OFF
Discharge	NEGATIVE	ON	OFF
By Pass	N/A	OFF	ON

The current and voltage relationship are studied and well documented in [96] and given below:

$$u_{dc} = v_{jp} + v_{jm} + L\frac{d}{dt}(i_{jp} + i_{jm}) \tag{3.25}$$

$$i_{dc} = i_{ap} + i_{bm} + i_{cm} \tag{3.26}$$

where $j = (a, b, c)$, the subscript p means upper arm items, and subscript m means lower arm items. The power equations is given by:

$$P_{dc} = u_{dc} \times i_{dc} \tag{3.27}$$

$$P_{ac} = 3(v_{jp} + v_{jm})i_j \tag{3.28}$$

3.4.2 Control Strategy Designed for FFTS

For the sake of simplification, the BtB-MMC also be implemented the decoupling control same as the M^3C system. The receiving side applied the constant voltage and frequency control, while the sending side control the DC link voltage and reactive power of the terminal. The control strategy is shown in Fig. 3.18. The subscript S means the current and voltage from sending side converter, and the subscript R means the current and voltage from receiving side converter.

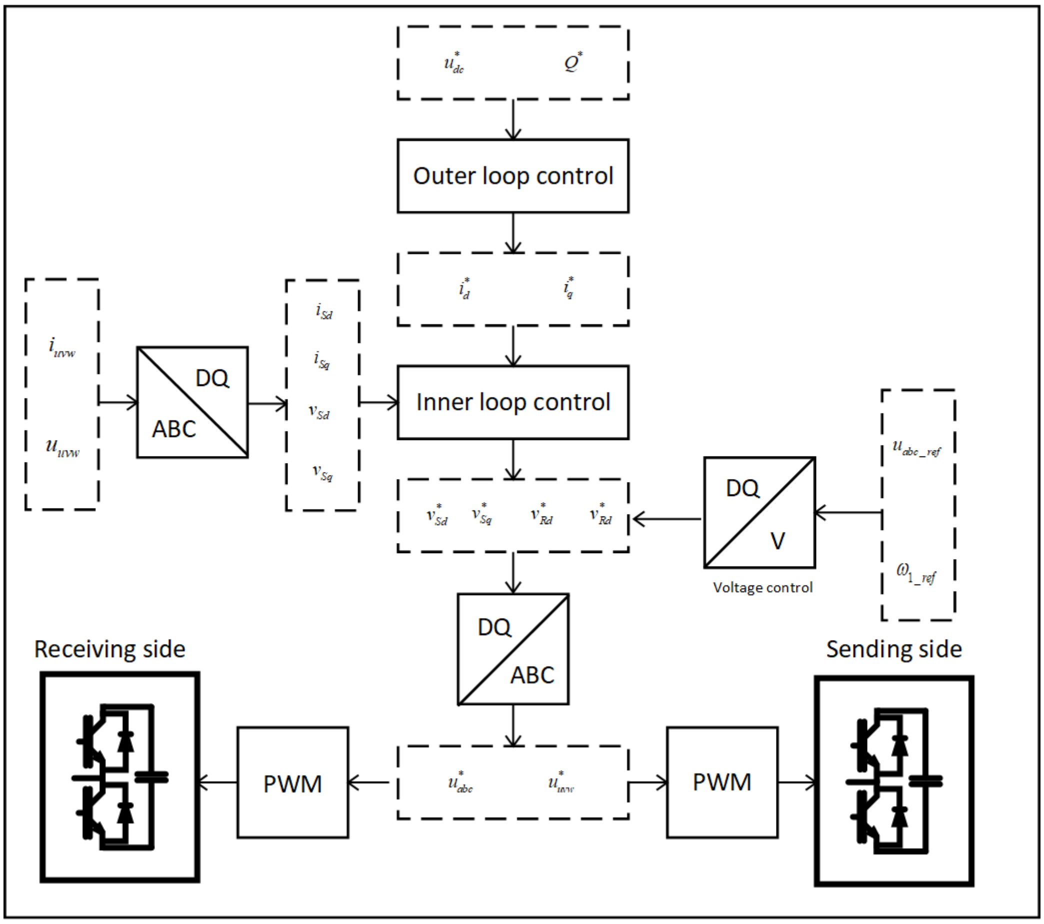

Fig. 3.18 Control diagram of BtB-MMC

3.4.3 EMT Model and SMIB Simulation

The EMT model of the BtB-MMC is also developed using MATLAB/Simulink to test the proposed control strategy. System is modelled as a single machine system. The BtB-MMC is modelled based on the structure shown in Fig. 3.16. The number of sub-module inside each arm has been set 40, which is same as the M^3C system. The sub-module is modelled with the build-in half bridge MMC model from MATLAB/Simulink library. The external AC system of receiving side is also modelled as the low frequency system with 20 Hz, and the sending side is modelled as the system frequency system with 60 Hz. Both the AC systems are represented by a constant voltage sources model. As the constant voltage and frequency control strategy implemented in receiving side converter, there is no active power control within the system. The AC voltage of both side of converter are set to 66 kV, and the DC link voltage is set to 100 kV. Full technology detail can be found in Appendix A. The simulation results are introduced as follow.

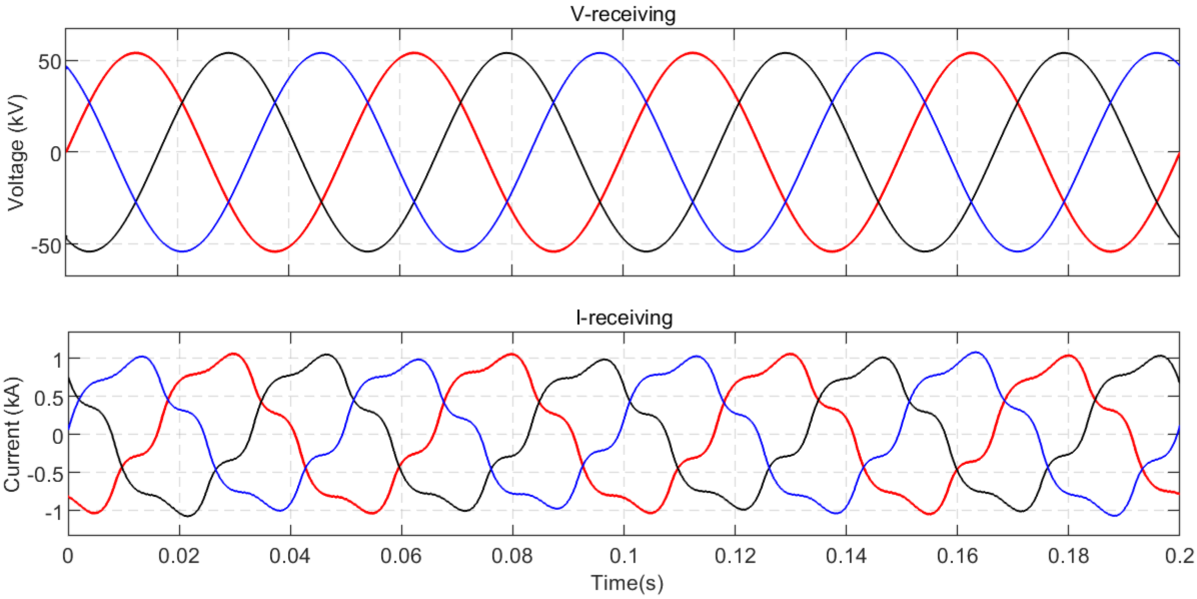

(a) Terminal Voltage (up) and Current (down) in Receiving Side

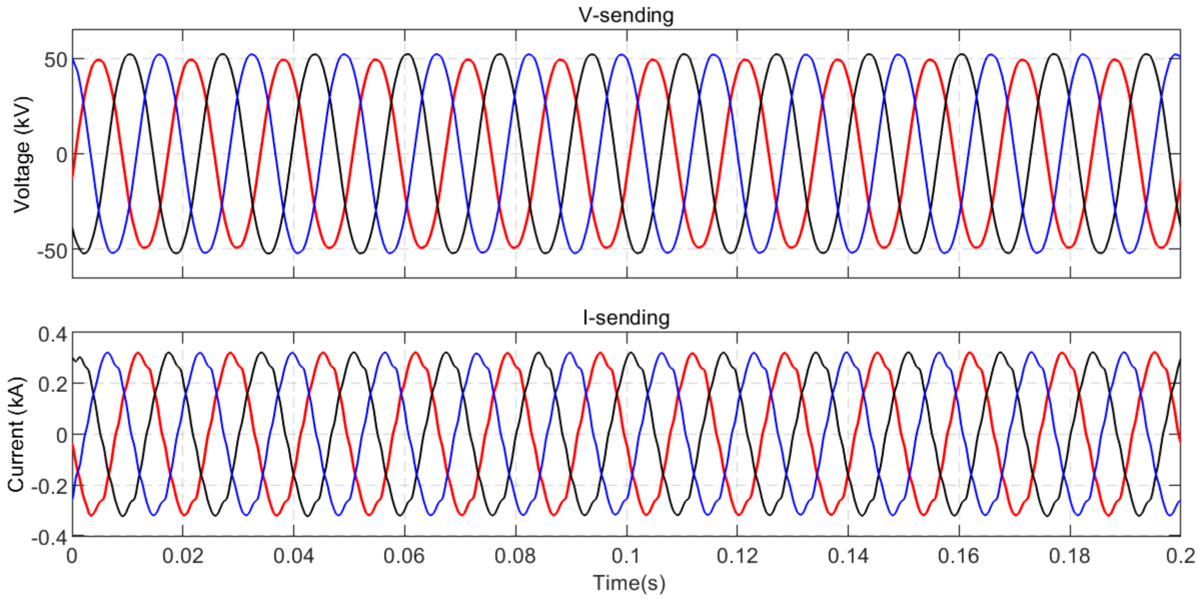

(b) Terminal Voltage (up) and Current (down) in Sending Side

Fig. 3.19 Terminal Voltages and Currents of BtB-MMC

The terminal voltages and currents from the receiving side and sending side of the BtB-MMC are shown in Fig. 3.19 (a) and (b). As figure shown, the voltage waveforms are ideal sinusoidal with the defined frequencies, while the current magnitude are relatively small. The simulation result is similar to the results from M^3C system discussed in last section, which again, validates the proposed constant voltage and frequency control strategy.

Fig. 3.20 shows the DC link voltage and current. As figure shown, the voltage ripple of DC link voltage are negligible, and the DC current are very small, which complies the expected results.

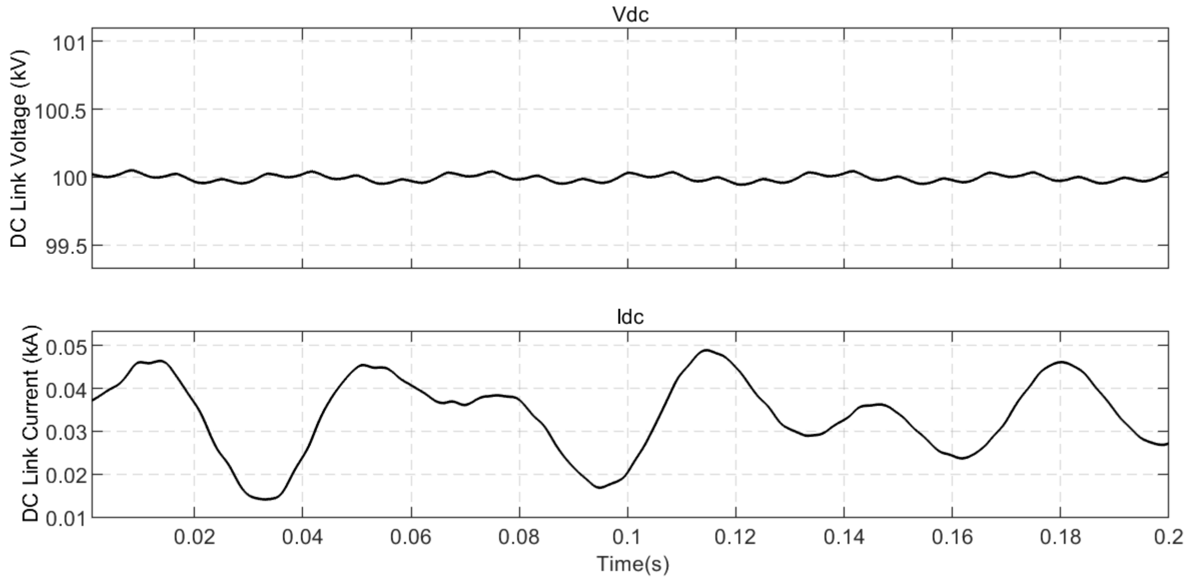

Fig. 3.20 DC Voltage and Current Waveforms of MMC

The EMT model of BtB-MMC will be served in Chapter 5 to integrated with the offshore wind power system. A further comparison study against the M^3C based FFOWPS will be presented in Chapter 5.

3.5 Summary

This Chapter has discussed the key components within the FFOWPS - the offshore wind turbine and the onshore AC/AC frequency converter. DFIG has been considered as the wind power generation in this study due to its advantages including low cost, high power transfer efficiency and flexible controllability. The system structure, working principle and control strategies of the DFIG have been introduced and discussed. A single machine EMT model of DFIG for adapting the low frequency system has been developed using the MATLAB/Simulink software. The simulation results have validated the good performance of DFIG system working with the low frequency system. The M^3C system has been choosen as the frequency converter of the FFOWPS. The system structure has been introduced and the methods to isolate the different frequencies components within the converter has been discussed. In order to integrate the M^3C with the offshore wind power system, the constant voltage and current control strategy has been implemented to the fractional frequency side of the converter. The EMT model of M^3C has been developed to test system performance as the frequency converter and the simulation waveforms have complied the expected results. The reliability of proposed constant voltage and current control strategy have been also validated. Based on the DFIG and M^3C EMT models developed in this chapter, small signal modelling and stability model will be developed in Chapter 4, and the system stability analysis will be carried out. The BtB-MMC has also been discussed in this chapter to worked as the frequency converter for FFOWPS. The EMT model has developed for further comparison study in Chapter 5.

Chapter 4 Small Signal Stability Analysis of DFIG-M3C based FFOWPS

4.1 Introduction

The offshore wind power generation is becoming a vital part of world's power generation mix. In recent years, the penetration of offshore wind power keeps increasing and the latest British Energy Security Strategy indicated that UK is planning to deliver up to 50GW offshore wind power by 2030 to meet its 'Net zero target'[6]. With the increasing capacity of offshore wind power generation, it is worth to consider the power deliver system. Compared with the traditional HVAC transmission system, the FFTS uses a lower frequency to achieve a higher transmission capacity, which provides a more economical solution to boost grid capacity, no matter of constructing new transmission line or upgrading current system. Compared to HVDC, FFTS requires no offshore converter station, which makes it an economical choice for offshore wind power generation with medium distance power transmission. Besides, the well-developed AC transmission system is more reliable for large offshore wind power generation, considering the low inertia ability of wind power generator.

The AC/AC converter plays a key component inside the FFTS, which steps the fractional frequency power to system frequency power. Cycloconverter was a candidate of FFTS in early research. However, cycloconverter is not a suitable participant for offshore wind power transmission as its poor controllability and low power quality. On the contrary, the M^3C provided a possible solution to offshore wind power integration with its full controllability and low harmonics.

Great efforts have been made to prove the reliability of FFOWPS, however, rare studies pay attention to the small signal stability domain. Considering the particularity of offshore wind farm in geographic, it is necessary to study the dynamic performance of FFOWPS as a whole. The small signal model of FFOWPS should consider the interaction between wind power generation and AC/AC converter, and the whole system should be convenient to integrate with external AC grid. In this chapter, a small signal model of DFIG-M^3C based FFOWPS is introduced. The main contributions of this chapter are list below:

- A small signal model of FFOWPS including the dynamic model of DFIG and M^3C, and the transmission line between the two systems is developed;
- The eigen-value based small signal stability analysis is performed to optimize system parameters and improve system damping ability;
- The EMT model of FFOWPS is developed and the time domain simulation is presented to validate the proposed small signal model and optimized system performance.

The structure of proposed DFIG-M^3C based FFOWPS is shown in Fig. 4.1. The offshore DFIG generates the fractional frequency power at 20 Hz, and transmits it to the onshore M^3C substation. The M^3C absorbs the offshore power and transfer the frequency to the system standard at 60 Hz, and sends it to main gird.

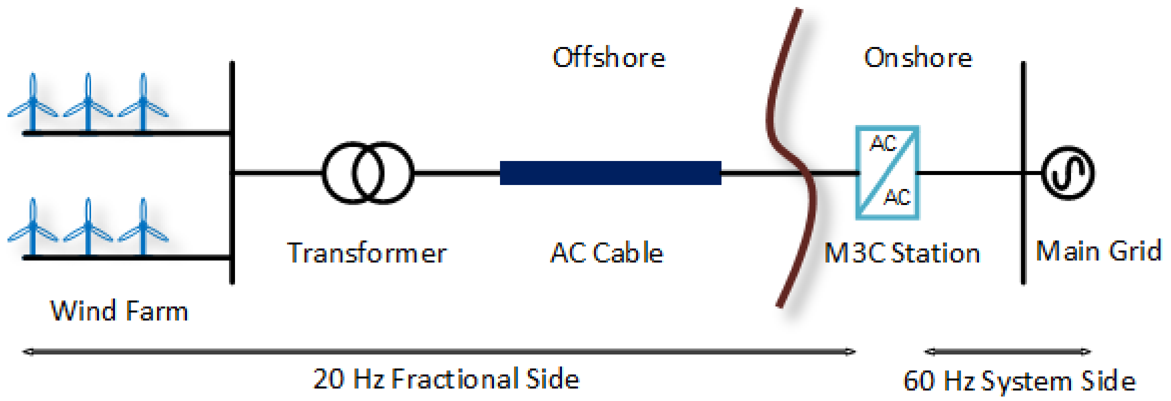

Fig. 4.1 Structure of DFIG-M^3C based FFOWPS

The remainder of this chapter will describe the small signal models of each power electronic device separately before combining them. The eigen-values based small signal stability analysis will be implemented to discuss the impact of controller parameters on the system's damping capability, and the control system will be optimised based on the results of the analysis. In order to evaluate the performance of the optimised system, the EMT model of the proposed FFOWPS will be developed and simulated with various disturbances.

4.2 Modelling of DFIG

As shown in Fig.3.1, the model of DFIG wind turbine consist of the induction generator, the driven train, and the back-to-back converter with its controller. The mathematic equations of DFIG model are well documented and presented in [70]. The small signal model state variables of each part are introduced below based on the mathematic equations.

4.2.1 Induction Generator

The generator of DFIG can be represented as an wound rotor induction machine. The voltage and current relationship is similar to that of an induction generator introduced in [61]. The model of DFIG generator can be expressed as:

$$\frac{X_s'}{\omega_s}\dot{i}_{ds} = v_{ds} - \left[R_s + \frac{1}{\omega_s T_0'}(X_s - X_s')\right] \times i_{ds} \\ -(1-s_r)E_d' - \frac{L_m}{L_{rr}}v_{dr} + \frac{1}{\omega_s T_0'}E_q' + X_s' i_{qs} \qquad (4.1)$$

$$\frac{X_s'}{\omega_s}\dot{i}_{qs} = v_{qs} - \left[R_s + \frac{1}{\omega_s T_0'}(X_s - X_s')\right] \times i_{qs} \\ -(1-s_r)E_q' - \frac{L_m}{L_{rr}}v_{qr} - \frac{1}{\omega_s T_0'}E_d' - X_s' i_{ds} \qquad (4.2)$$

$$\dot{E}_d' = s_r\omega_s E_q' - \omega_s\frac{L_m}{L_{rr}}v_{qr} - \frac{1}{T_0'} \times \left[E_d' + (X_s - X_s')i_{qs}\right] \qquad (4.3)$$

$$\dot{E}_q' = -s_r \omega_s E_d' + \omega_s \frac{L_m}{L_{rr}} v_{dr} - \frac{1}{T_0'} \times \left[E_q' - (X_s - X_s') i_{ds}\right] \tag{4.4}$$

where i_{ds} and i_{qs} are stator currents in DQ frame, respectively; v_{dr} and v_{qr} are rotor voltage in DQ frame, respectively; v_{ds} and v_{qs} are stator voltage in DQ frame, respectively; E_d' and E_q' are voltage behind the transient reactance in DQ frame, defined as $E_d' = -\omega_s \frac{L_m}{L_{rr}} \psi_{qr}$ and $E_q' = -\omega_s \frac{L_m}{L_{rr}} \psi_{dr}$, respectively; ψ_{dr} and ψ_{qr} are rotor flux linkages in DQ frame, respectively; s_r is the rotor slip; X_s and X_s' are stator reactance and transient reactance, defined as $X_s = \omega_s L_{ss}$ and $X_s' = \omega_s[L_{ss} - (\frac{L_m^2}{L_{rr}})]$, respectively; T_0' is the rotor time constant, defined as $T_0' = \frac{L_{rr}}{R_r}$; L_{ss} and L_{rr} are the stator self-inductance and rotor self-inductance, respectively; L_m is the mutual inductance; R_s and R_r are the stator and rotor resistance, respectively.

The d-q frame 4th order model of induction generator can be expressed with state and input variables as:

$$x_g = \left[i_{ds}, i_{qs}, E_d', E_q'\right] \tag{4.5}$$

$$u_g = \left[v_{ds}, v_{qs}, v_{dr}, v_{qr}\right] \tag{4.6}$$

4.2.2 Drive Train

The two-mass model is usually used to represent the drive train system of DFIG. The power relationship of DFIG is described in Chapter 3. The mathematic equations can be written as:

$$\dot{\omega}_t = \frac{T_m - T_{sh}}{2H_t} \tag{4.7}$$

$$\dot{\theta}_{tw} = \omega_b(\omega_t - \omega_r) \tag{4.8}$$

$$\dot{\omega}_r = \frac{T_{sh} + T_e - B\omega_r}{2H_g} \tag{4.9}$$

$$T_{sh} = K_{sh}\theta_{tw} + D_{sh}\dot{\theta}_{tw} \quad (4.10)$$

where H_g and H_t are the inertia constant of DFIG generator and wind turbine, respectively; T_m is the wind turbine mechanical torque; T_{sh} is the shaft torque; T_e is the DFIG electromagnetic torque; ω_t is the wind turbine angle speed; B is the DFIG generator friction coefficient; K_{sh} and D_{sh} are shaft stiffness coefficient and damping coefficient of wind turbine, respectively;

The mechanical torque T_m and electromagnetic torque T_e of DFIG are given by:

$$T_m = \frac{P_{WF}}{\omega_t} = \frac{0.5\rho\pi R^2 C_p V_w^3}{\omega_t} \quad (4.11)$$

$$T_e = \frac{P_s}{\omega_s} \quad (4.12)$$

As mentioned in Chapter 3, the maximum power coefficient C_p can be achieved by controlling the rotor speed, and the maximum power can be extract from the wind.

The model of driven train can be expressed with state variables list below:

$$x_t = [\omega_t, \theta_{tw}, \omega_r] \quad (4.13)$$

$$u_t = [T_e] \quad (4.14)$$

4.2.3 Converters

The structure of a back-to-back converter is shown in Fig. 4.2. Considering the power is balanced in the converter, power exchange equation can be expressed as:

$$P_r = P_g + P_{DC} \quad (4.15)$$

where P_r is the active power of rotor-side converter, which is given by:

$$P_r = v_{dr}i_{dr} + v_{qr}i_{qr} \quad (4.16)$$

P_g is the active power of grid-side converter, which is given by:

$$P_g = v_{dg}i_{dg} + v_{qg}i_{qg} \tag{4.17}$$

P_{DC} is the active power of DC link, which is given by:

$$P_{DC} = v_{DC}i_{DC} = -Cv_{DC}\frac{dv_{DC}}{dt} \tag{4.18}$$

where i_{dr} and i_{qr} are rotor current in DQ frame, respectively; v_{dg} and v_{qg} are grid-side converter voltage in DQ frame, respectively; i_{dg} and i_{qg} are grid-side converter current in DQ frame, respectively; v_{DC} is the DC link capacitor voltage; i_{DC} is the DC link capacitor current; C is the capacitance of DC link capacitor.

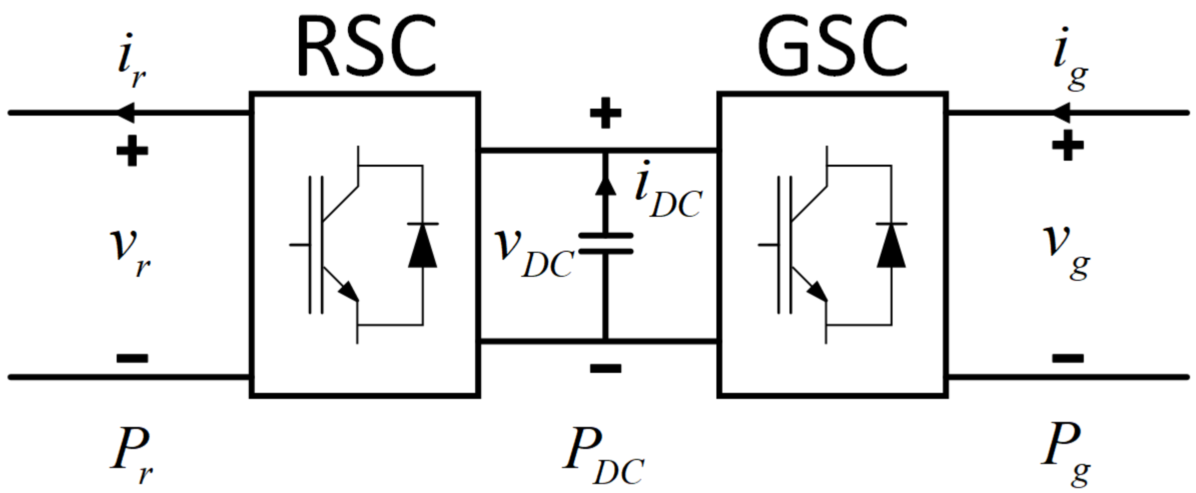

Fig. 4.2 Back-to-back converter

Substitute (17), (18) and (19) into (16), the model of converter can be derived as:

$$\dot{v_{DC}} = \frac{1}{Cv_{DC}}\left[v_{dg}i_{dg} + v_{qg}i_{qg} - \left(v_{dr}i_{dr} + v_{qr}i_{qr}\right)\right] \tag{4.19}$$

4.2.4 Control System

The control blocks are designed based the control strategies introduced in Chapter 3. The decoupling control is implemented. The rotor-side converter is for controlling the electromagnetic torque and reactive power at the generator, while the grid-side converter is controlling the terminal reactive power and maintaining the DC link voltage. The control block diagrams are shown in Fig. 4.3 and Fig. 4.4, respectively. Where x_1, x_2, x_3, x_4 are the intermediate variables in rotor-side converter controller and x_5, x_6, x_7 are the intermediate variables in grid-side converter controller.

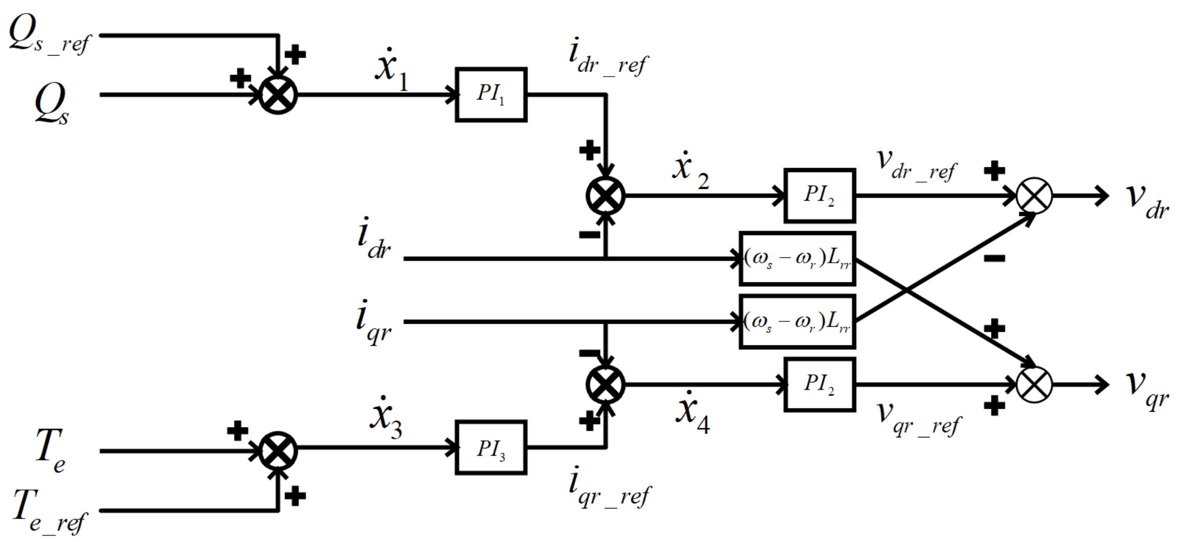

Fig. 4.3 Controller of rotor side converter

The control equations of RSC are given by:

$$\dot{x}_1 = Q_s^* + Q_s \tag{4.20}$$

$$\dot{x}_2 = K_{p1}(Q_s^* + Q_s) + K_{i1}x_1 - i_{dr} \tag{4.21}$$

$$v_{dr} = K_{p2}x_2 + K_{i2}x_2 - (\omega_s - \omega_r)L_{rr}i_{qr} \tag{4.22}$$

$$\dot{x}_3 = T_e^* + T_e \quad (4.23)$$

$$\dot{x}_4 = K_{p3}(T_e^* + T_e) + K_{i1}x_3 - i_{qr} \quad (4.24)$$

$$v_{qr} = K_{p2}x_4 + K_{i2}x_4 + (\omega_s - \omega_r)L_{rr}i_{dr} \quad (4.25)$$

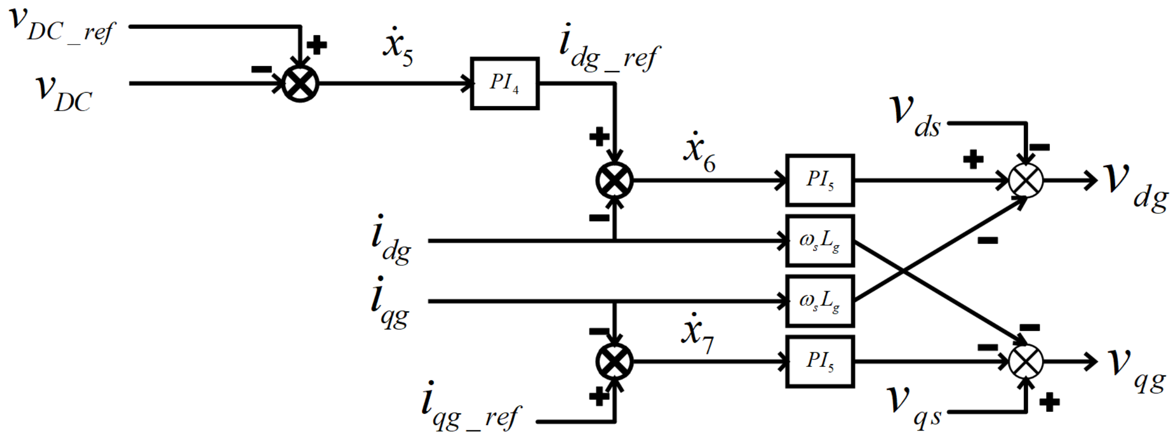

Fig. 4.4 Controller of grid side converter

The control equations of GSC are given by:

$$\dot{x}_5 = v_{DC}^* - v_{DC} \quad (4.26)$$

$$\dot{x}_6 = K_{p4}(v_{DC}^* - v_{DC}) + K_{i4}x_5 - i_{dg} \quad (4.27)$$

$$v_{dg} = -K_{p5}x_6 - K_{i5}x_6 + v_{ds} + \omega_s L_g i_{qg} \quad (4.28)$$

$$\dot{x}_7 = i_{qg}^* - i_{qg} \quad (4.29)$$

$$v_{qg} = -K_{p5}x_7 - K_{i5}x_7 + v_{qs} - \omega_s L_g i_{qg} \quad (4.30)$$

The back-to-back converter and its control can be modelled with state and input variables as below:

$$x_c = [x_1, x_2, x_3, x_4, v_{DC}, x_5, x_6, x_7, i_{dg}, i_{qg}] \quad (4.31)$$

$$u_c = [i_{dr}, i_{qr}, v_{ds}, v_{qs}] \quad (4.32)$$

4.2.5 Combined Model

After eliminated the input and output variables, the entire model of DFIG is of 17th order differential equation and can be expressed as:

$$\dot{x}_{WF} = f(x_{WF}, u_{WF}) \tag{4.33}$$

All variable are listed below:

$$\begin{cases} x_{WF} = [\omega_t, \theta_{tw}, \omega_r, i_{ds}, i_{qs}, E'_d, E'_q, \\ x_1, x_2, x_3, x_4, v_{DC}, x_5, x_6, x_7, i_{dg}, i_{qg}] \\ u_{WF} = [v_{ds}, v_{qs}] \end{cases} \tag{4.34}$$

4.3 Modelling of M3C

The structure of $\mathrm{M^3C}$ is shown in Fig.3.7. The voltage and current quantities with the two frequencies from the two side of $\mathrm{M^3C}$ are coupled together as there is no DC link inside the $\mathrm{M^3C}$. Considering the simplification, the complicated ABC terms are decoupled by implementing d-q transformation. The $\mathrm{M^3C}$ is modeled with the dynamic of capacitor voltage and arm current, and combined with the converter controller.

4.3.1 Dynamics of Voltage and Currents

The arm current and voltage of $\mathrm{M^3C}$ are discussed in Chapter 3 and shown in (3.9) – (3.10). By implementing the d-q transformation, the coupled terms can be isolated. The dynamic model of capacitor voltages including the 40 Hz voltage ripples and AC arm currents of $\mathrm{M^3C}$ can be derived. The mathematical models have been well documented in [41], and the equations are listed below:

The capacitor voltages are expressed as:

$$\begin{cases} \dot{U}_{dc\_0} = \frac{1}{2U_{DC} \cdot C}(E_{d20}I_{d20} + E_{q20}I_{q20} + \\ \qquad E_{d60}I_{d60} + E_{q60}I_{q60}) \\ \dot{U}_{dc\_d2} = 2\omega_1 U_{dc\_q2} - \frac{1}{2U_{DC} \cdot C}(E_{q20}I_{q20} \\ \qquad -E_{d20}I_{d20}) \\ \dot{U}_{dc\_q2} = -2\omega_1 U_{dc\_d2} + \frac{1}{2U_{DC} \cdot C}(E_{d20}I_{q20} \\ \qquad +E_{q20}I_{d20}) \end{cases} \tag{4.35}$$

where U_{dc_0} is the DC component of capacitor voltage; U_{dc_d2} and U_{dc_q2} are the 40 Hz components of capacitor voltage in d-q frame, respectively; E_{d20}, E_{q20} and E_{d60}, E_{q60} are the magnitudes of modulation voltages at both frequencies in d-q frame, respectively; I_{d20}, I_{q20} and I_{d60}, I_{q60} are the magnitudes of arm currents at both frequencies in d-q frame, respectively;

And the dynamic models of AC currents are expressed as:

$$\begin{cases} \dot{I}_{d20} = \frac{1}{L}U_{d20} - \frac{R}{L}I_{d20} + \omega_1 I_{q20} - \frac{1}{L}U_{arm\_20\mathrm{d}} \\ \dot{I}_{q20} = \frac{1}{L}U_{q20} - \frac{R}{L}I_{q20} - \omega_1 I_{d20} - \frac{1}{L}U_{arm\_20q} \\ \dot{I}_{d60} = -\frac{1}{L}U_{d60} - \frac{R}{L}I_{d60} + \omega_3 I_{q60} - \frac{1}{L}U_{arm\_60d} \\ \dot{I}_{q60} = -\frac{1}{L}U_{q60} - \frac{R}{L}I_{q60} - \omega_3 I_{d60} - \frac{1}{L}U_{arm\_60q} \end{cases} \tag{4.36}$$

where,

$$\begin{cases} U_{arm\_20d} = \frac{NU_{dc\_0}}{U_{DC}}E_{d20} + \frac{N}{2U_{DC}}(U_{dc\_d2}E_{d20} \\ \qquad +U_{dc\_q2}E_{q20}) \\ U_{arm\_20q} = \frac{NU_{dc\_0}}{U_{DC}}E_{q20} - \frac{N}{2U_{DC}}(U_{dc\_d2}E_{q20} \\ \qquad -U_{dc\_q2}E_{d20}) \\ U_{arm\_60d} = \frac{U_{dc\_0}}{U_{DC}}E_{d60} \\ U_{arm\_60q} = \frac{U_{dc\_0}}{U_{DC}}E_{q60} \end{cases} \tag{4.37}$$

The converter can be modelled with state and input variables as follows:

$$x_{cvtr} = [U_{dc\_0}, U_{dc\_d2}, U_{dc\_q2}, I_{d20}, I_{q20}, I_{d60}, I_{q60}] \tag{4.38}$$

$$x_{cvtr} = [E_{d20}, E_{q20}, E_{d60}, E_{q60}, \omega_1, \omega_3, U_{d20}, U_{q20}, U_{d60}, U_{q60}] \tag{4.39}$$

4.3.2 Control System

The control block of M^3C is designed based on the control strategies described in Chapter 3. The M^3C connects the offshore wind farm with the onshore main grid. The main control objective of the M^3C is to collect the power generated by the offshore wind farm, step up the fractional frequency to the standard system frequency and deliver it to the main grid via the onshore transmission line. The output power of DFIG is controlled by its rotor-side converter.

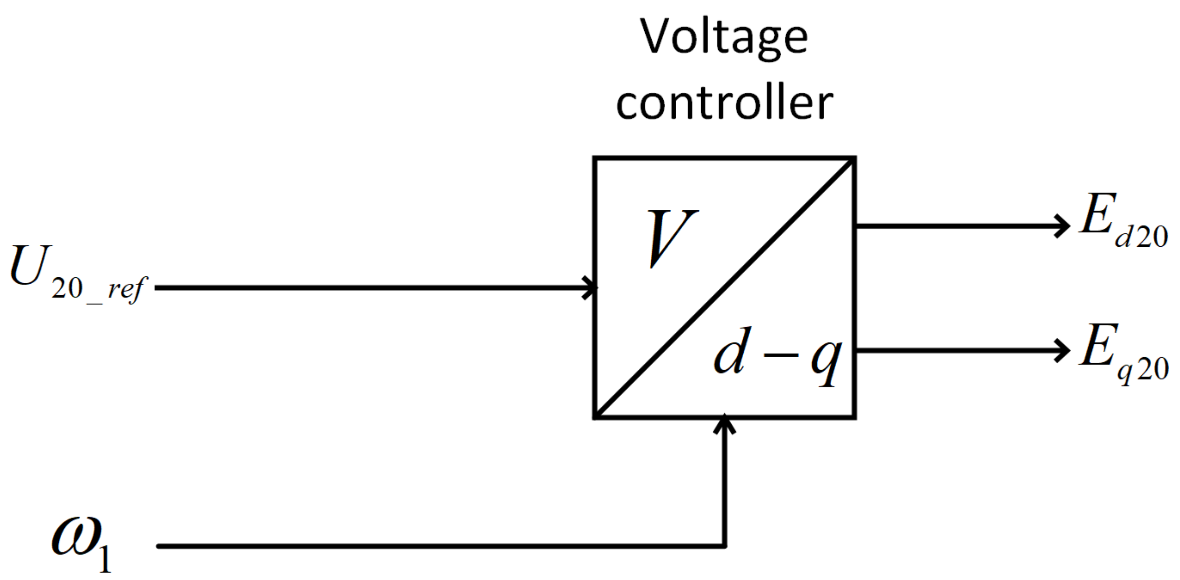

Fig. 4.5 Voltage control of $\mathbf{M^3C}$ fractional frequency side

To avoid the conflicting controls between M^3C and DFIG, the fractional frequency side of M^3C is operated as a voltage source with constant voltage magnitude and frequency, so the power generated from the offshore wind farm can be absorbed smoothly by M^3C. The control block diagram of fractional frequency side is shown in Fig. 4.5.

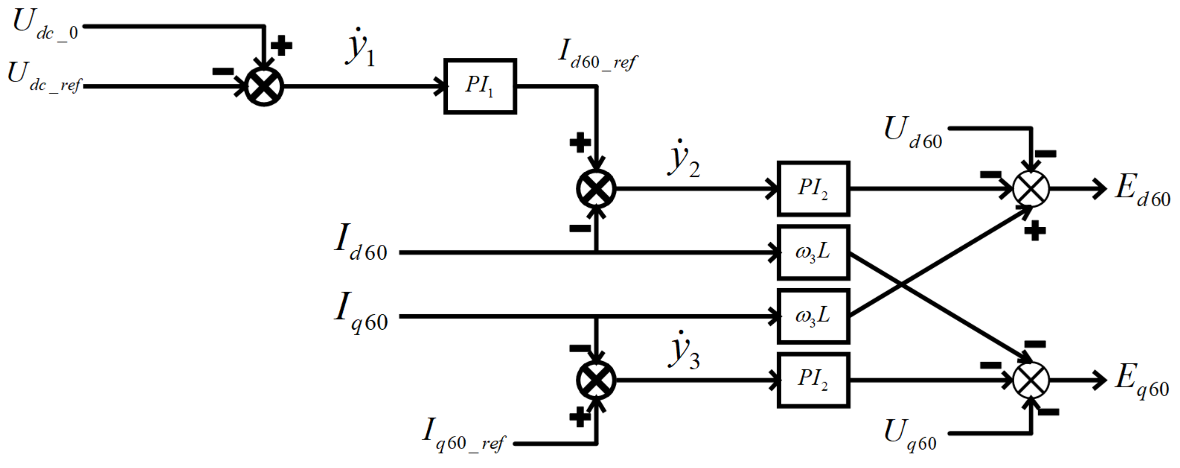

Fig. 4.6 Vector control of $\mathbf{M^3C}$ system frequency side

The system frequency side of M^3C controls the capacitor DC voltage and reactive power. The control block diagram is shown in Fig. 4.6, and the control equations are given below:

$$E_{d20} = U_{20\_ref}\, sin(\omega_{1\_0} + \beta_1) \tag{4.40}$$

$$E_{q20} = -U_{20\_ref}\, cos(\omega_{1\_0} + \beta_1) \tag{4.41}$$

$$\dot{y}_1 = U_{dc\_0} - U_{dc\_ref} \tag{4.42}$$

$$\dot{y}_2 = k_{p1}U_{dc\_0} - k_{p1}U_{dc\_ref} + k_{i1}y_1 - I_{d60} \tag{4.43}$$

$$\dot{y}_3 = I_{q60\_ref} - I_{q60} \tag{4.44}$$

$$\begin{aligned} E_{d60} = -U_{d60} - k_{p2}(kp_1 U_{dc_0} - k_{p1}U_{dc_{ref}} + k_{i1}y_1 \\ -I_{d60}) - k_{i2}y_2 + I_{q60}\omega_3 L \end{aligned} \tag{4.45}$$

$$\begin{aligned} E_{q60} = -U_{q60} - k_{p2}\left(I_{q60_{ref}} - I_{q60}\right) \\ -k_{i2}y_3 - I_{d60}\omega_3 L \end{aligned} \tag{4.46}$$

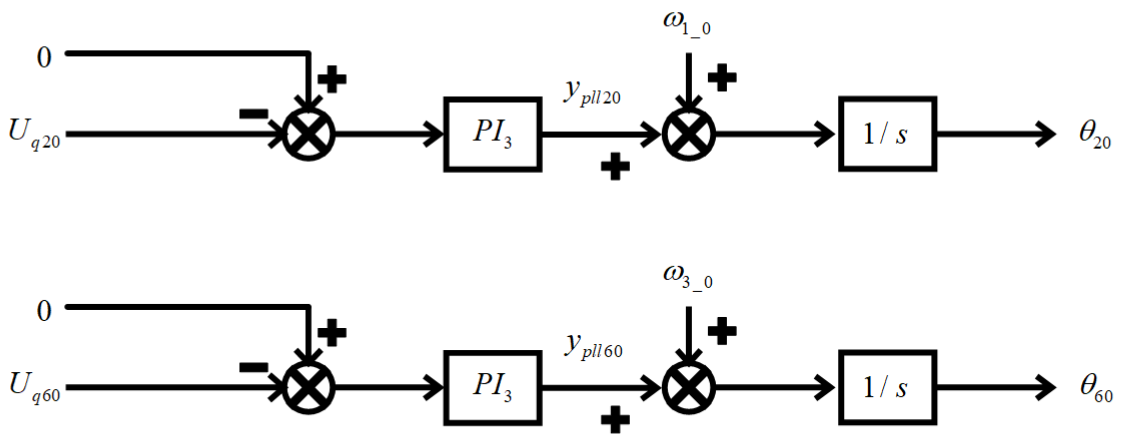

Fig. 4.7 PLL control of M^{3}C

Two PLL blocks shown in Fig. 4.7 are used to provide the angle references of 20 Hz and 60 Hz side, respectively.

$$\dot{y}_4 = U_{q20} \tag{4.47}$$

$$\dot{y}_{pll20} = -k_{p3}U_{q20} - k_{i3}y_4 \tag{4.48}$$

$$\dot{y}_5 = U_{q60} \tag{4.49}$$

$$\dot{y}_{pll60} = -k_{p3}U_{q60} - k_{i3}y_5 \tag{4.50}$$

The state and output variables of the control system are listed below:

$$x_{crtl} = [y_1, y_2, y_3, y_4, x_{pll20}, y_5, x_{pll60}] \tag{4.51}$$

$$z_{crtl} = [E_{d20}, E_{q20}, E_{d60}, E_{q60}, \omega_1, \omega_3] \tag{4.52}$$

4.3.3 Combined Model

Eliminating the input variables of converter model using the output variables from its control system, the combined model of $\mathrm{M^3C}$ can be expressed as :

$$\dot{x}_{M3C} = f(x_{M3C}, u_{M3C}) \tag{4.53}$$

All the state and input variables are listed as follows:

$$\begin{cases} x_{M3C} = [U_{dc\_0}, U_{dc\_d2}, U_{dc\_q2}, I_{d20}, I_{q20}, I_{d60}, I_{q60}, \\ \qquad\qquad y_1, y_2, y_3, y_4, x_{pll20}, y_5, x_{pll60}] \\ u_{M3C} = [U_{d20}, U_{q20}, U_{d60}, U_{q60}] \end{cases} \tag{4.54}$$

4.4 Modelling of AC Transmission Line

The terminal of DFIG is connected to fractional frequency side of $\mathrm{M^3C}$ via the submarine cable, as shown in Fig. 4.8. v_s is the terminal voltage of the DFIG generator stator winding; U_{20} is the AC voltage of $\mathrm{M^3C}$ fractional frequency side. As mentioned above, the fractional frequency side of $\mathrm{M^3C}$ is controlled with constant voltage and frequency. U_{20} is controlled with constant voltage magnitude and frequency, in that case, U_{20} can be used as the input variable for both DFIG and $\mathrm{M^3C}$ system in small signal model. Based on Kirchhoff's law, the interface between DFIG and $\mathrm{M^3C}$ can be expressed as the equation in d-q frame below:

$$\begin{bmatrix} v_{ds} \\ v_{qs} \end{bmatrix} = \begin{bmatrix} U_{d20} \\ U_{q20} \end{bmatrix} - \begin{bmatrix} R_{TL} & -X_{TL} \\ X_{TL} & R_{TL} \end{bmatrix} \times \left(\begin{bmatrix} i_{ds} \\ i_{qs} \end{bmatrix} + \begin{bmatrix} i_{dg} \\ i_{qg} \end{bmatrix} \right) \tag{4.55}$$

where $\mathrm{R_{TL}}$ and $\mathrm{X_{TL}}$ are combined resistance and reactance of the submarine cable and the transformer, respectively.

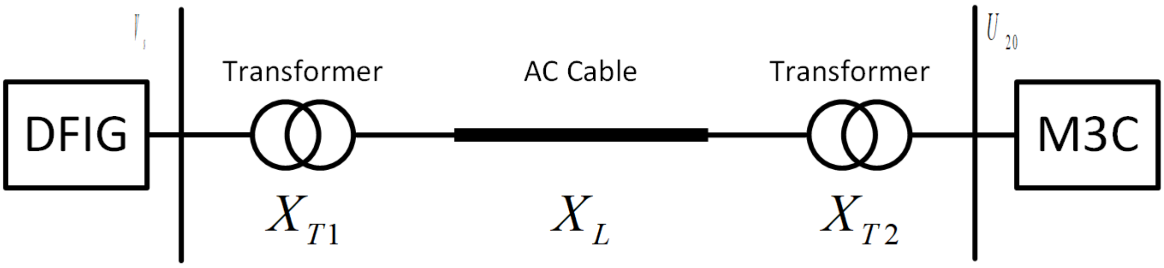

Fig. 4.8 Interface between DFIG and M^3C

4.5 Combined DFIG-M3C FFOWPS and System Performance

4.5.1 Small Signal Model for the Combined FFOWPS

The main grid is modelled as an infinite bus in the small signal model. The state space model of DFIG is derived from (4.33), and it can be expressed as:

$$\Delta \dot{x}_{WF} = A_{WF}\Delta x_{WF} + B_{WF}\Delta u_{WF} \tag{4.56}$$

The state space model of M^3C is derived from (4.53), and it can be expressed as:

$$\Delta \dot{x}_{M3C} = A_{M3C}\Delta x_{M3C} + B_{M3C}\Delta u_{M3C} \tag{4.57}$$

Based on (4.55), the linearized equation of the interface between DFIG and M^3C can be expressed as:

$$\Delta u_{WF} = C\Delta x_{WF} + D\Delta u_{M3C} \tag{4.58}$$

The outputs of DFIG can be eliminated by inputs of M^3C. The complete 31st order state space equation of FFOWPS is given by:

$$\Delta \dot{x} = A\Delta x + B\Delta u \tag{4.59}$$

where $\Delta x = [\Delta x_{WF}, \Delta x_{M3C}]^T$, $\Delta u = [\Delta u_{M3C}]$

4.5.2 System Performance

A non-linear detailed dynamic model of FFOWPS is developed in MATLAB/Simulink for EMT simulation. The model is running with discrete mode, with simulation time step of $1\mu s$ for the precise simulation of the dynamics of all the power electronics. The DFIG and $\mathrm{M^3C}$ systems are discussed and modelled in Chapter 3. The DFIG system is developed to generate 20 Hz power, the wound rotor induction generator and the back-to-back converter is modelled. The control system is modelled based on the control block diagram shown in Fig. 4.3 and Fig. 4.4. A 120 kV 100 km AC transmission line is modelled with a build-in three-phase PI section, as shown in Fig. 4.8. The $\mathrm{M^3C}$ topology is shown in Fig. 3.7. There are 9 arms, connecting the two sides of $\mathrm{M^3C}$, which are modelled with the build-in full-bridge modular multilevel converter model, and each arm contains 40 sub-modules. The control systems are designed based on the control block diagrams in Fig. 4.5 and Fig. 4.6, respectively. The AC grid is modelled as a voltage source. Full technical details can be found in Appendix.

The voltage and current profiles of the FFOWPS are shown in Fig. 4.9 and Fig. 4.10, which show satisfactory waveforms. Fig. 4.9 (a) shows the AC line voltage and current at the DFIG terminal. From the harmonic analysis, the THD voltage and current are only 1.08% and 1.76%, respectively. Fig. 4.9 (b) and (c) show the AC line voltages and currents at the two sides of $\mathrm{M^3C}$, respectively. For 20 Hz side, the harmonic quantities of voltage and current of other frequencies are 0.42% and 1.39%, respectively; for 60 Hz side, the harmonic quantities of voltage and current of other frequencies are 0.21% and 0.23%, respectively.

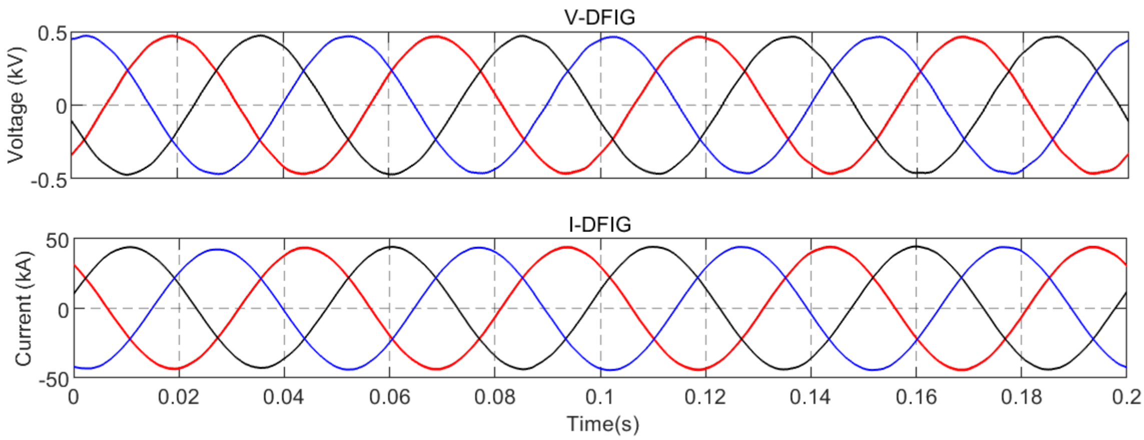

(a) DFIG terminal AC voltage (up) and current (down)

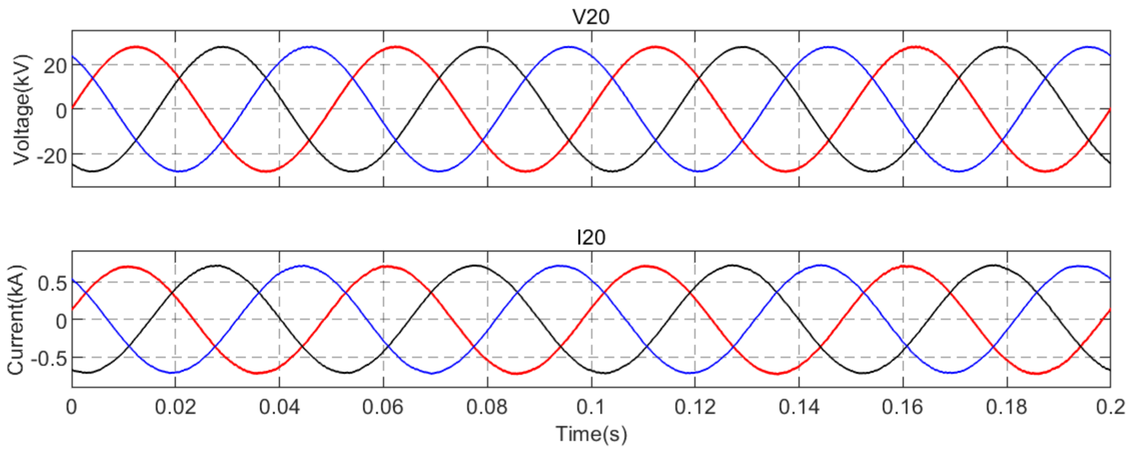

(b) M^3C 20 Hz AC voltage (up) and current (down)

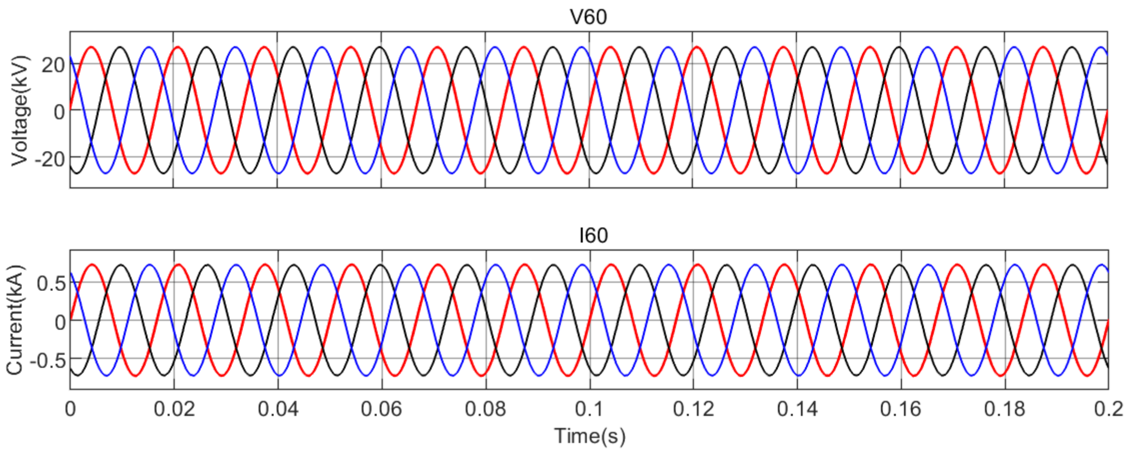

(c) M^3C 60 Hz AC voltage (up) and current (down)

Fig. 4.9 AC line voltage and current waveforms of FFOWPS

Fig. 4.10 (a) and (b) shows the arm voltages and currents inside M^3C, which are the decoupled waveform of 20 Hz and 60 Hz quantities. The voltage and current ripples are negligible with only 0.09% and 1.5%; Fig. 4.10 (c) shows the capacitor voltage of single sub-module. As described in Chapter 3, due to the deep coupling of two frequencies side quantities, the voltage ripple should be considered. The 40 Hz ripple has largest magnitude other than DC component, which is 0.018 kV. Other frequencies ripples can be ignored. It proves a good performance of M^3C as the AC/AC frequency changer converter.

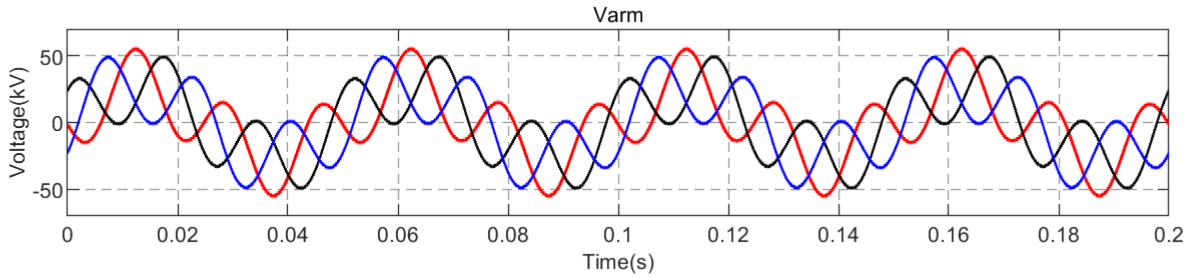

(a) M^3C Arm voltage

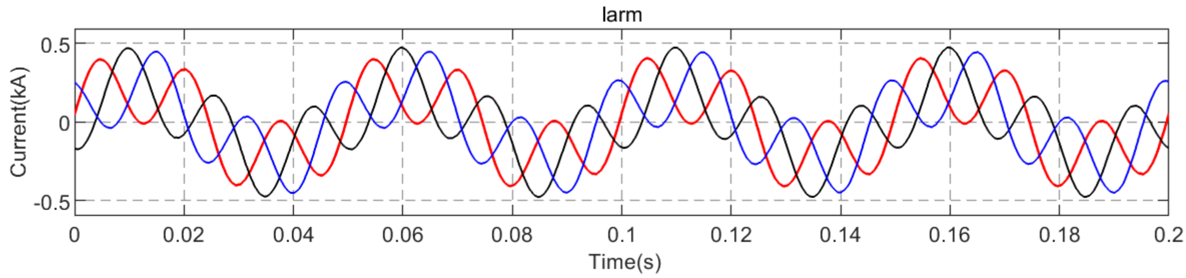

(b) M^3C Arm current

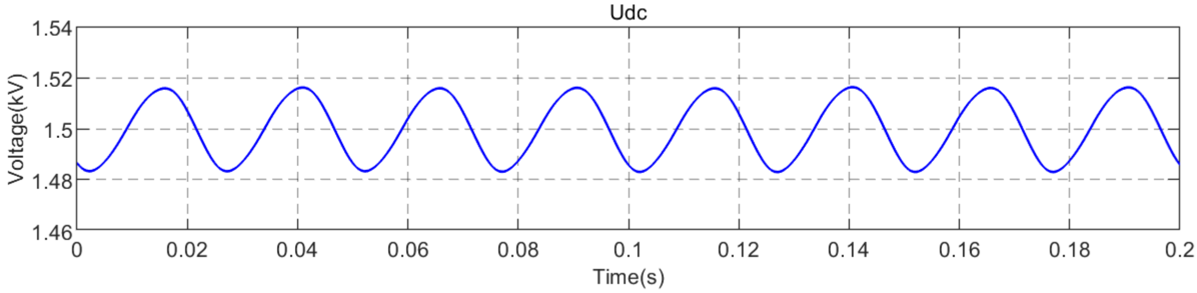

(c) M^3C Capacitor voltage

Fig. 4.10 Voltage and current profiles of M^3C

Fig. 4.11 shows the power transmission of the FFOWPS. A 0.1 pu step change of power reference of DFIG is set at 15s, as shown in the figure, the M^3C smoothly absorbed the power from wind farm and transmitted it to 60 Hz side. The power waveform between two side of M^3C successfully tracked the change of power from DFIG.

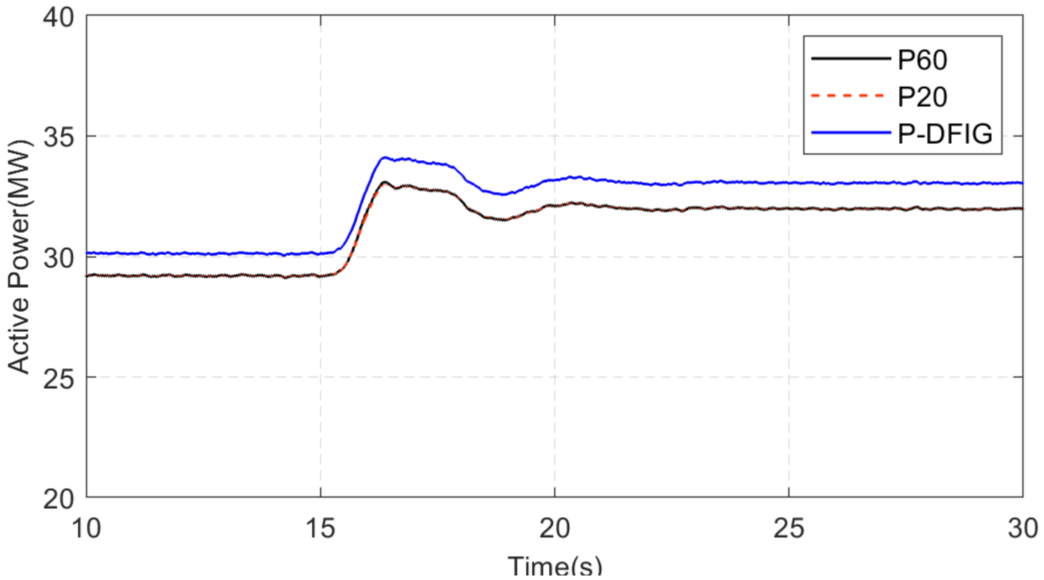

Fig. 4.11 Power transmission between DFIG and M^3C

4.6 Eigenvalue Analysis and Parameters Optimized

The small signal stability analysis of FFOWPS is carried out based on the developed small signal stability model. The eigenvalues of FFOWPS are calculated and all the real parts of eigenvalues are negative, which indicate that the proposed FFOWPS is originally stable. There are 7 pair modes of oscillation, which are listed in Table 4.1, including the damping ratios and participation factors. To improve the system damping performance, the small signal analysis is implemented to optimise the system parameters.

As shown in Table 4.1, modes $\lambda_{5,6}$ and $\lambda_{7,8}$ are both associated with capacitor voltages of M^3C and the damping of $\lambda_{5,6}$ is only 5% which is so called poor damping. To improve the system dynamic performance, it is worthy to assess the PI controllers used to control the capacitor DC voltage and the value of capacitance.

TABLE 4.1 EIGENVALUES ANALYSIS

$\boldsymbol{\lambda}$	$\boldsymbol{\sigma}$	$\boldsymbol{\omega}$	Damping (%)	Dominate factors
$\boldsymbol{\lambda_{1,2}}$	-372.44	849.36	40.16	v_{dc}, i_{dg}
$\boldsymbol{\lambda_{3,4}}$	-89.58	536.38	14.86	i_{q20}, y_{pll20}
$\boldsymbol{\lambda_{5,6}}$	-12.67	252.24	5	U_{dc_d2}, U_{dc_q2}
$\boldsymbol{\lambda_{7,8}}$	-119.43	91.6	79.35	U_{dc_0}, i_{d20}
$\boldsymbol{\lambda_{9,10}}$	-15.21	130.45	11.58	E'_d, E'_q, i_{ds}
$\boldsymbol{\lambda_{11,12}}$	-1.02	9.65	10.54	ω_t, θ_{tw}, ω_r
$\boldsymbol{\lambda_{13,14}}$	-0.35	0.56	53.42	y_4, y_5

4.6.1 Stability Analysis of Controller Parameters

Parameters k_{p1} and k_{i1} are used to control the DC capacitor voltage of M^3C. The performance of modes $\lambda_{7,8}$ are plotted where k_{p1} changes between 0 and 50. Fig. 4.12.(a) shows the damping ratio of the mode increased with the increasing of k_{p1} , and finally reach to 100% when k_{p1} is larger than 21. Fig. 4.12.(b) shows the root locus of the related mode. With the increasing of k_{p1}, the imaginary part of eigenvalues moves towards 0, then, one eigenvalue's real part keeps moving to negative side and another one moves to positive side. In that case, k_{p1} needs to be chosen considerately as either a small or large value may cause bad influence on system dynamic performance.

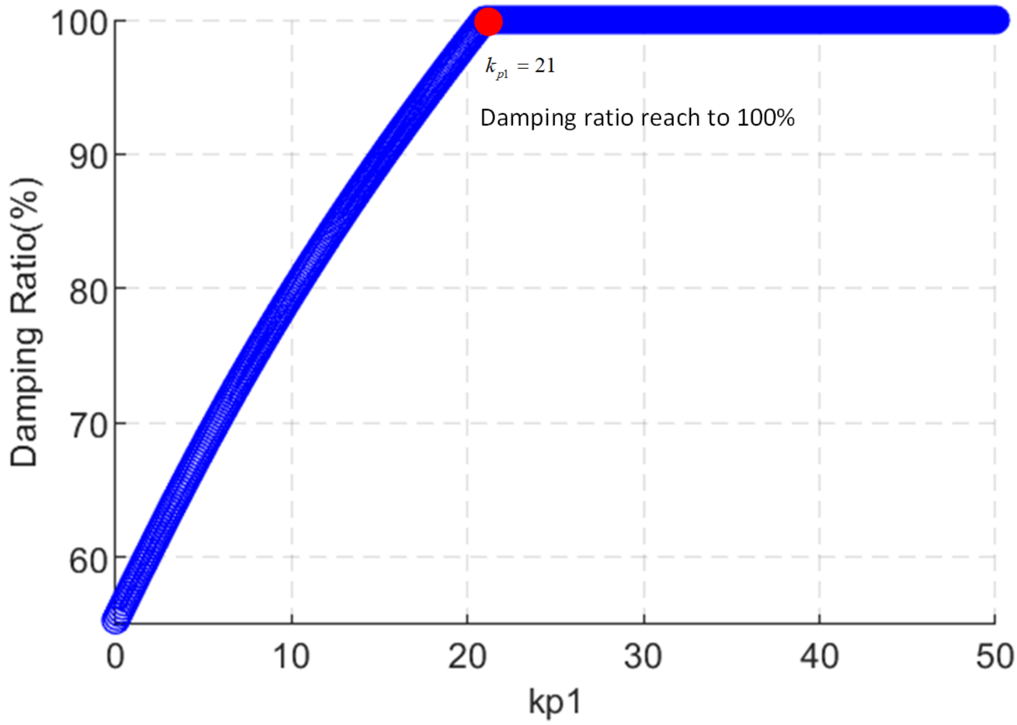

(a) Damping ratio of modes as k_{p1} increases

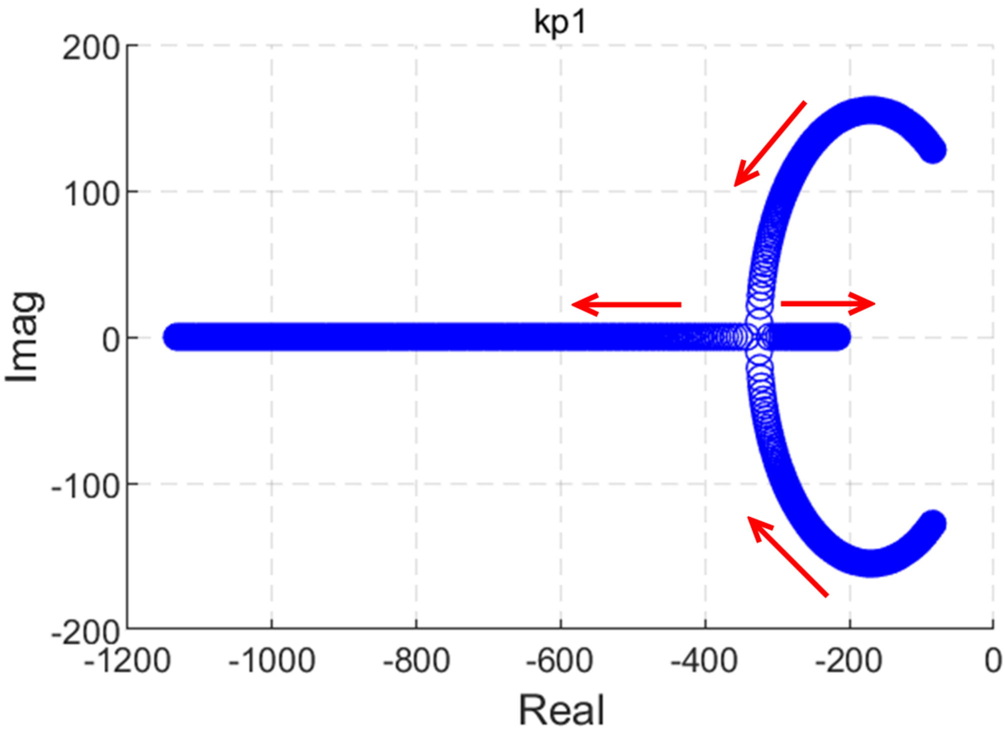

(b) Root locus of modes as k_{p1} increases

Fig. 4.12 Eigenvalue analysis of DC controller proportional gain

With a proper choice of k_{p1}, the choice of integral parameter k_{i1} becomes much clearer, as shown in Fig. 4.13, the value of k_{i1} between 0-10 does not affect the damping of modes, and a large k_{i1} leads to the more negative eigenvalues, which enhances the system small signal stability. However, it also has been found that large values of k_{p1} and k_{i1} have small negative influence on modes $\lambda_{5,6}$ even though they are not the dominated factors. Hence the values of k_{p1} and k_{i1} should be chosen accordingly.

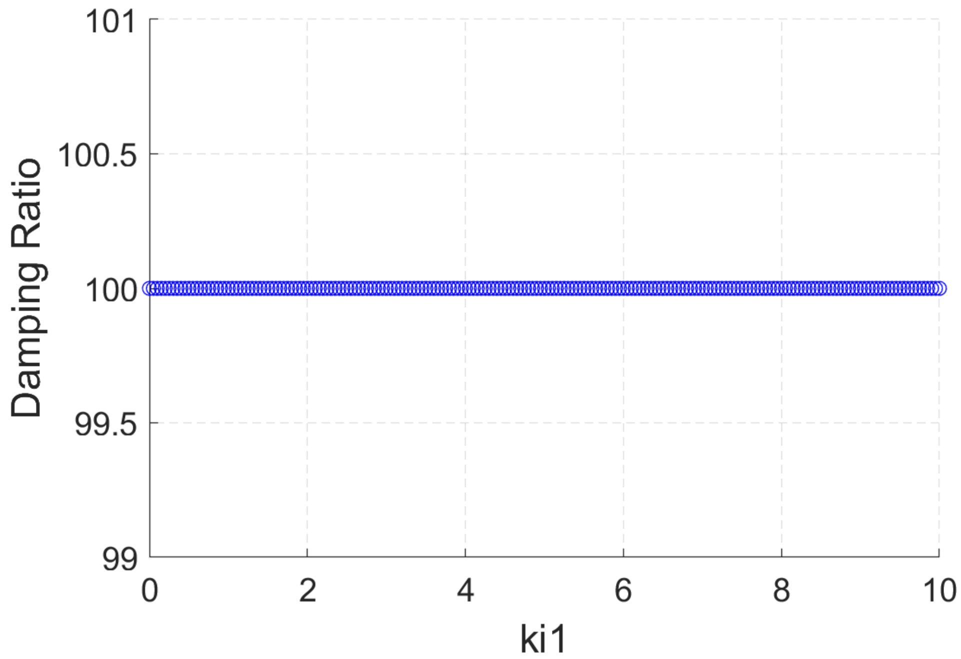

(a) Damping ratio of modes as k_{i1} increases

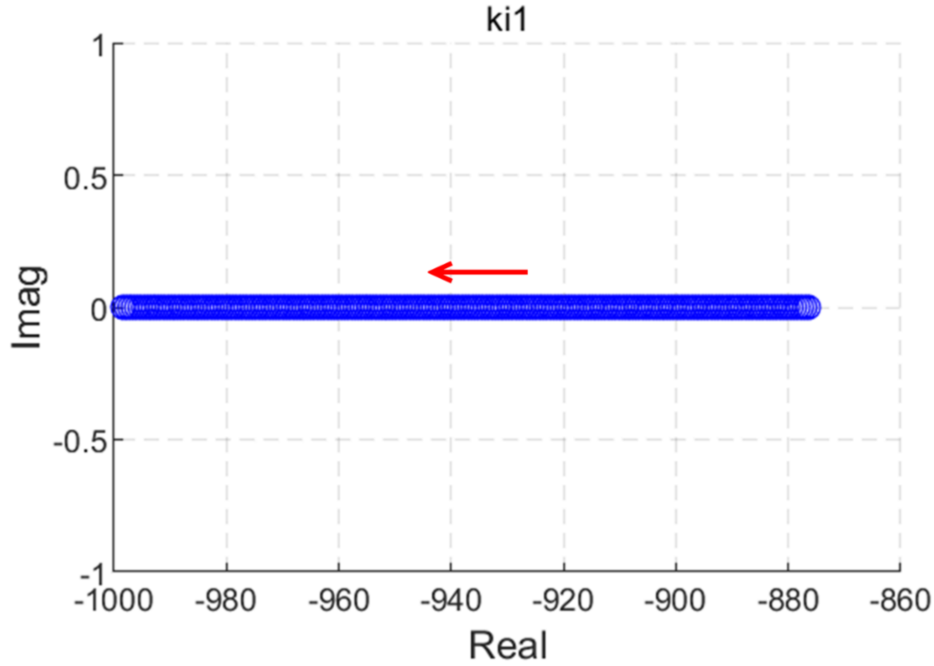

(b) Root locus of modes as k_{i1} increases

Fig. 4.13 Eigenvalue analysis of DC controller integral gain

4.6.2 Stability Analysis of Sub-module Capacitance

The influence of submodule capacitance to modes $\lambda_{7,8}$ is plotted in Fig. 4.14. As shown in the figure, a smaller capacitance can improve the poor damping mode. As the submodule capacitance also has the effects on arm voltage, it should be chosen carefully based on the small signal stability analysis.

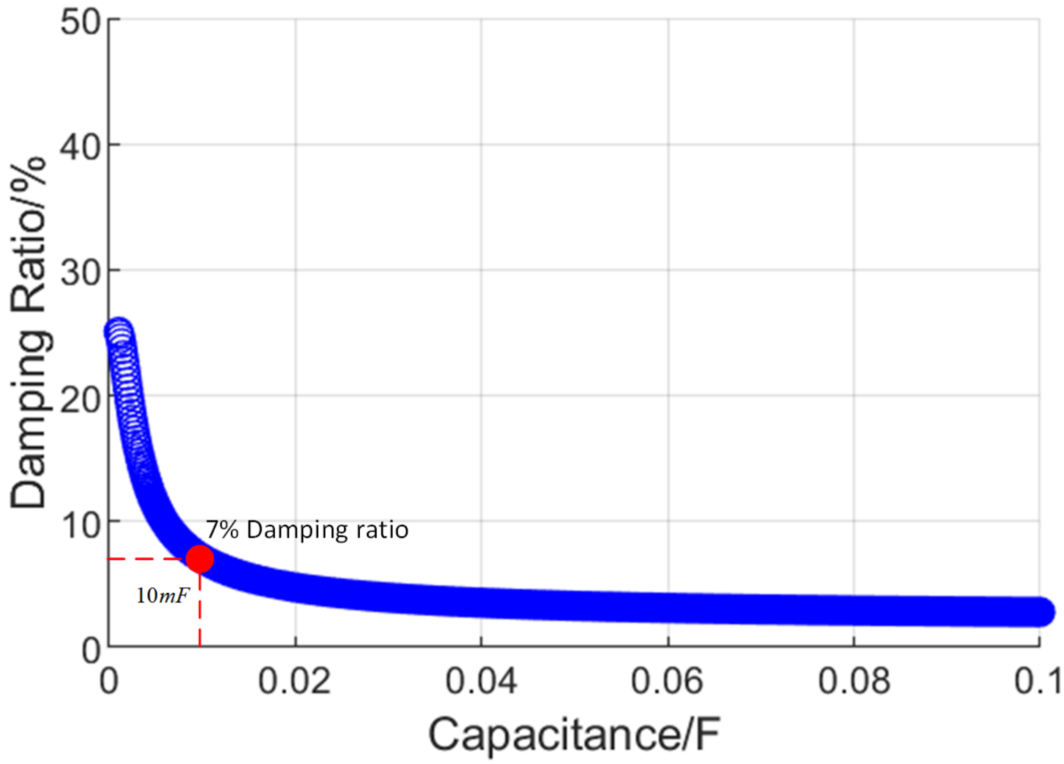

Fig. 4.14 Damping ratio of modes as capacitance increases

The rest of the parameters have been analysed with the proposed small signal stability model. The eigenvalue values of the optimized system are listed in Table 4.2. The oscillation modes are reduced to 4 pairs, and mostly control system related modes are enhanced to damping modes with more than 10% damping ratio. The rest of the modes are restricted with the mechanical parameters of the system or is conflicted to another control system. Overall, the system damping increases based on the small signal stability analysis results.

Table 4.2 Optimized System Eigenvalues

λ	σ	ω	Damping (%)	Dominate factors
$\lambda_{3,4}$	-89.58	536.38	52.61	i_{q20}, x_{pll20}
$\lambda_{5,6}$	-12.67	252.24	18.25	U_{dc_d2}, U_{dc_q2}
$\lambda_{9,10}$	-15.21	130.45	11.05	E'_d, E'_q, i_{ds}
$\lambda_{11,12}$	-1.02	9.65	10.53	ω_t, θ_{tw}, ω_r

4.7 Time Domain Simulation

To verify the improvement of system small signal stability with the optimized system parameters, the dynamic performances of proposed FFOWPS are discussed in this section.

4.7.1 System Performance under Small Disturbance

A step change of 0.1 pu is applied to the electromagnetic torque reference in the control of rotor side converter. The active power transmitted from DFIG to M^3C is simulated and plotted in Fig. 4.15. With the optimized system parameters, as shown in Fig. 4.15 (a), the active power generate from the DFIG system reaches to the steady state much quicker after the disturbance than the original system. Fig. 4.15 (b) shows the active power transmitted to the 60 Hz side of M^3C. As it shown, the system also damping quicker than the original system, and the M^3C tracked the power from the DFIG system more accurate.

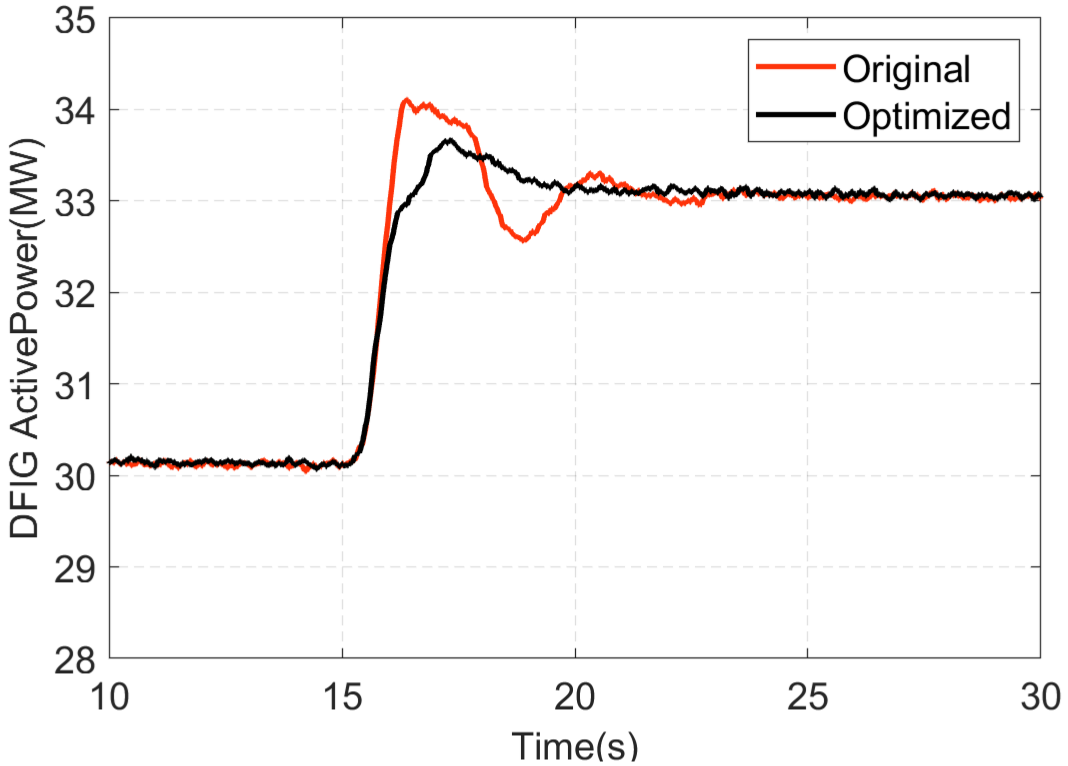

(a) DFIG active power

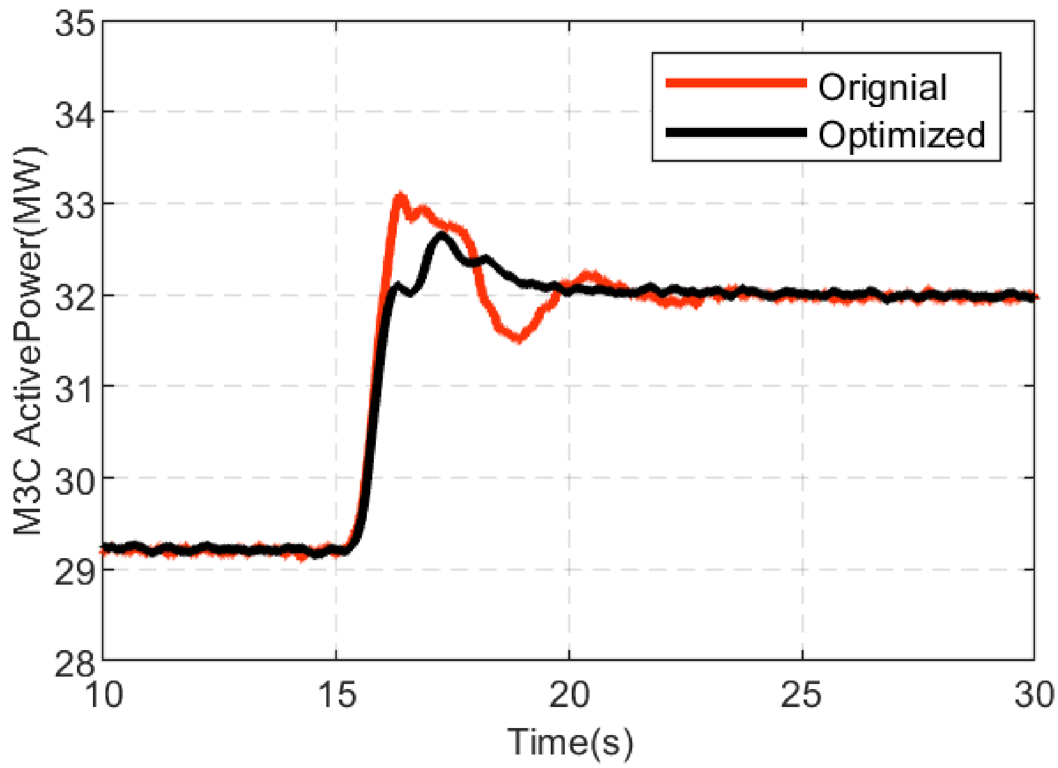

(b) M^3C 60 Hz side active power

Fig. 4.15 System dynamic performance under small disturbance

4.7.2 System Performance under Large Disturbance

To validate the optimized control parameters in improving the system stability, the dynamic response of the studied system under large disturbance are simulated. As shown in Fig. 4.16, A three-phase grounding fault is applied to the DFIG terminal, and the terminal of M^3C 60 Hz side, respectively. Fig. 4.17 shows the active power, DC voltage, terminal voltage and current of DFIG with the fault located at DFIG terminal bus. As shown in Fig. 4.17 (a), with the optimized control parameters, the active power oscillation caused by the fault of DFIG system can be damped out quickly. Fig. 4.17 (b) shows the DC voltage oscillation magnitude decreases significantly, which means the fault ride through ability of DFIG system has been improved. Fig. 4.17 (c) and (d) present the terminal voltage and current waveform oscillation of DFIG after fault, which are also damped out quicker than the original system. Fig. 4.18 present the active power, DC voltage, terminal voltage and current of M^3C system when the fault located at the 60 Hz side terminal bus of M^3C. Same as the DFIG system, the optimized parameters also improve the damping ability of M^3C system. The active power, DC voltage and terminal current oscillations after fault are all damped out quicker than the original case. The 60 Hz side terminal of M^3C is connected to main grid, in that case, the improvement of controller has less impact on the terminal voltage as it is mainly affected by main grid voltage. From the simulation results, it can be proved that the whole FFOWPS system damping ability is improved.

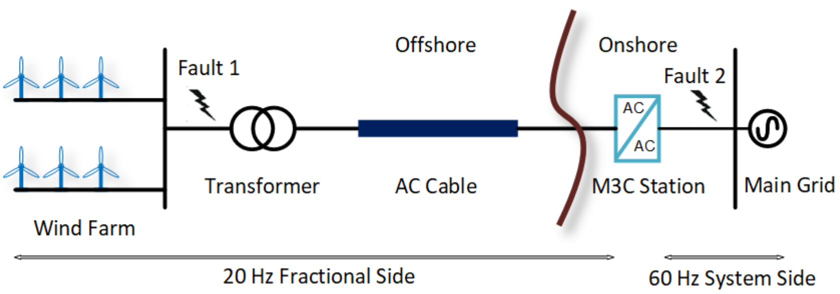

Fig. 4.16 System diagram under large disturbances

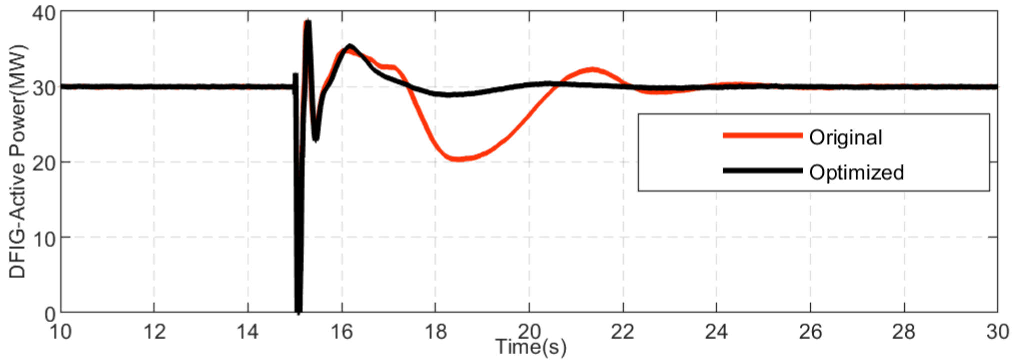

(a) DFIG active power

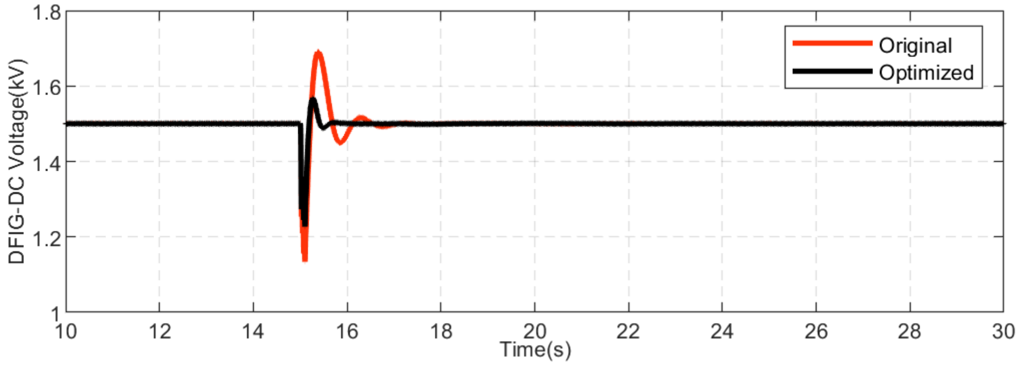

(b) DFIG DC voltage

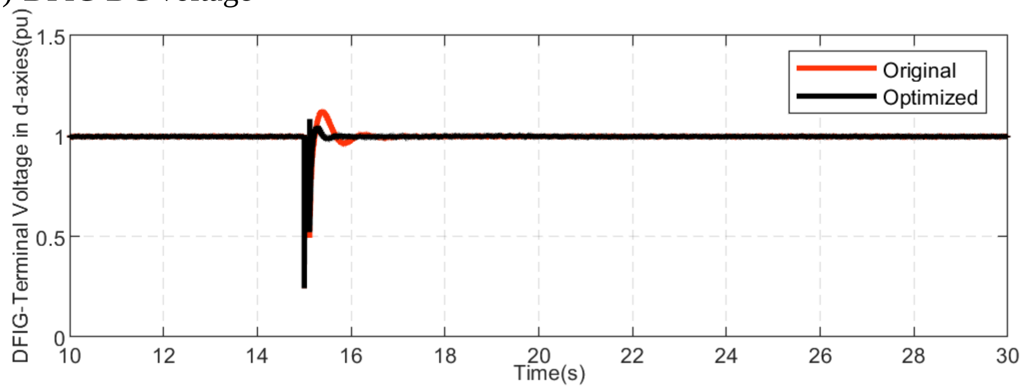

(c) DFIG terminal voltage in d-axis

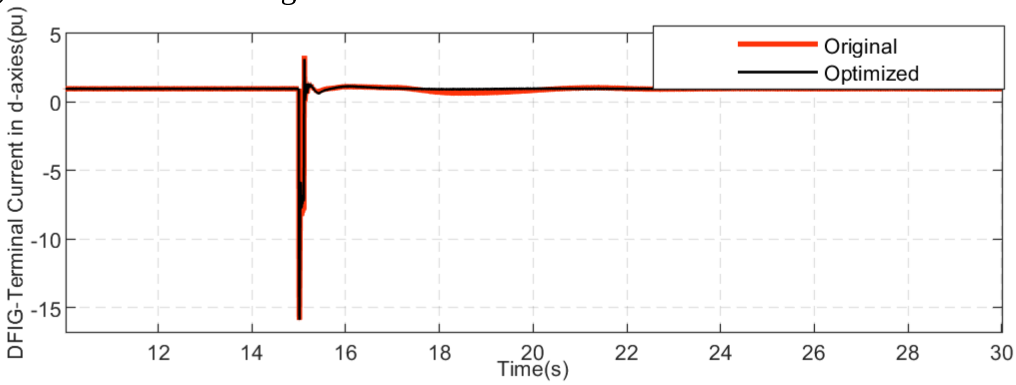

(d) DFIG terminal current in d-axis

Fig. 4.17 DFIG dynamic performance under large disturbance

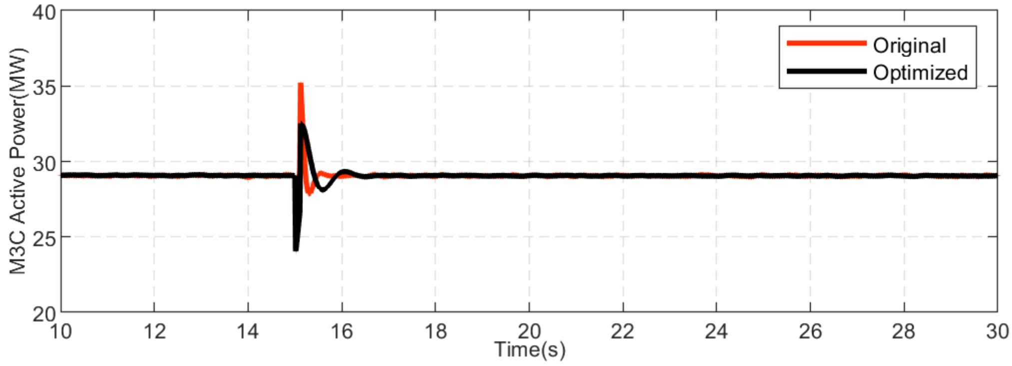

(a) M^3C active power

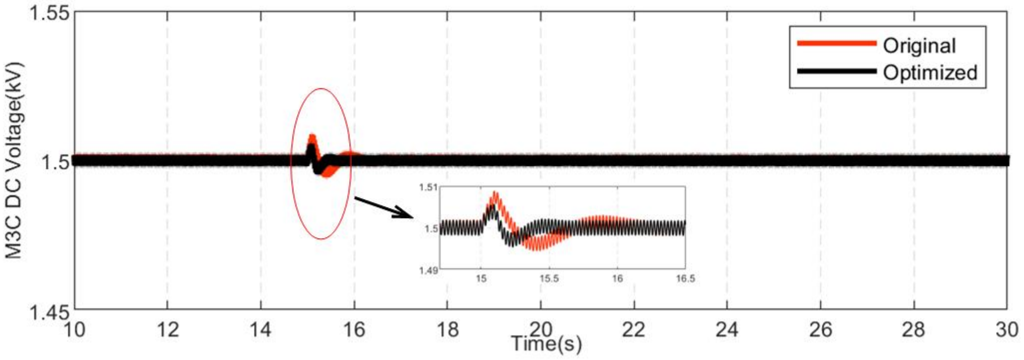

(b) M^3C DC voltage

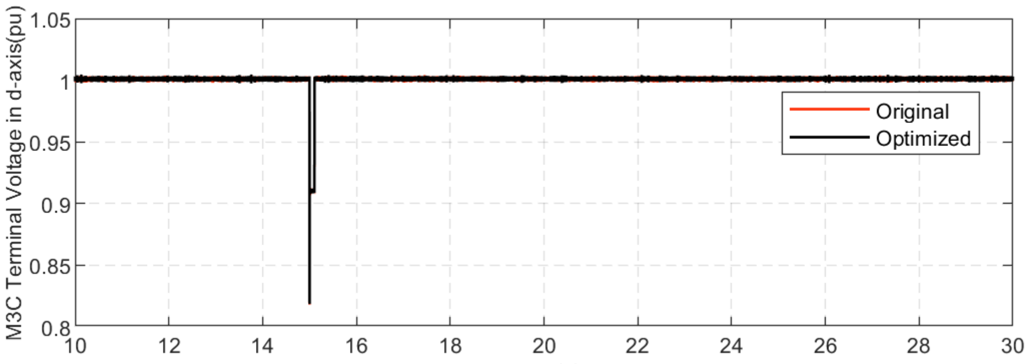

(c) M^3C terminal voltage in d-axis

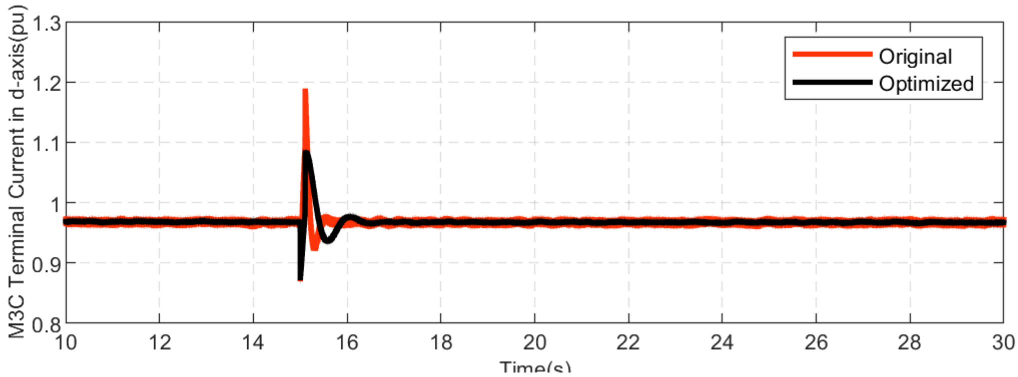

(d) M^3C terminal current in d-axis

Fig. 4.18 M^3C dynamic performance under large disturbance

4.8 Summary

The FFOWPS is reliable solution for the increasing penetration of offshore wind generation. The DFIG and M^3C are good candidates to form the FFOWPS. In order to study the impact of FFOWPS on the external AC grid, a detailed DFIG - M^3C based FFOPWS small signal stability model has been developed in this chapter. The constant voltage and frequency control are designed to connect DFIG with M^3C smoothly. The dynamic responses of voltages and currents have shown satisfactory dynamic performance using the proposed model where M^3C can track the power from DFIG accurately.

The proposed small signal stability model has been validated with the detailed EMT simulation results. The eigenvalue – based small signal stability analysis has been implemented to study the impact of control system parameters on system damping. From the analysis results, the PI control parameters can be chosen considerately as either a large or small value of proportional gain of the DC voltage controller can both cause a poor damping. With the optimized control parameters, the oscillation modes of the system are reduced from 7 pairs to 4 pairs and system damping can be increased. The optimized system has been tested with different disturbances, and from the analysis of the simulation results, it has been proved the system damping ability can be improved with the proposed small signal stability analysis.

Chapter 5 Techno – Economic Analysis and Comparisons of Technologies for FFOWPS

5.1 Introduction

The establishment of wind farm is shifting far ocean in recent years, where wind resources are more abundant and large-scale project planning is less complicated. However, the demands on transmission system are also increased. The M^3C based FFOWPS has been discussed as a promising option for offshore wind power integration with a medium distance in previous chapters. From [97], the installed capacity of offshore wind power generation in Europe was 780 MW in 2020 on average, and the transmission length to coast was approximately 44 km on average. These numbers instruct an excellent opportunity for FFOWPS advancement. As the frequency converter is the key component of the FFOWPS, this chapter discusses and compares the technical performances of M^3C-based FFOWPS and BtB-MMC based FFOWPS. In addition, the power industry is profit driven, who is more concerned with profit and risk than with the innovation of the technology. If a technology is determined as not cost-effective, the worth of related studies work would be diminished because the discoveries are unlikely to contribute to a practical program. Consequently, it is essential to conduct a cost analysis against to FFOWPS. Either the current research does not accurately forecast the expenditure of M^3C, or it simply considers the primary investment and disregards the time-related costs. Nevertheless, offshore wind power systems typically have a lifespan of 20 years. The total value of long-term expenses can have a considerable impact on analysis and decision-making due to their potential magnitude. The main contributions of this chapter are list below:

- The EMT model simulation of M^3C-based FFOWPS and BtB-MMC based FFOWPS are provided and their technical performance are evaluated and compared;
- A economic analysis model that incorporates capital costs and time-related expenses of FFOPWS is developed to produce a accurate cost profile for the technology;
- An economic comparison of M^3C -based FFOWPS and BtB-MMC based HVDC is implemented and the transmission distance economic crossover point of the two technologies is analysed.

Two advantageous transmission technologies for offshore wind power system integration are plotted in Fig. 5.1.

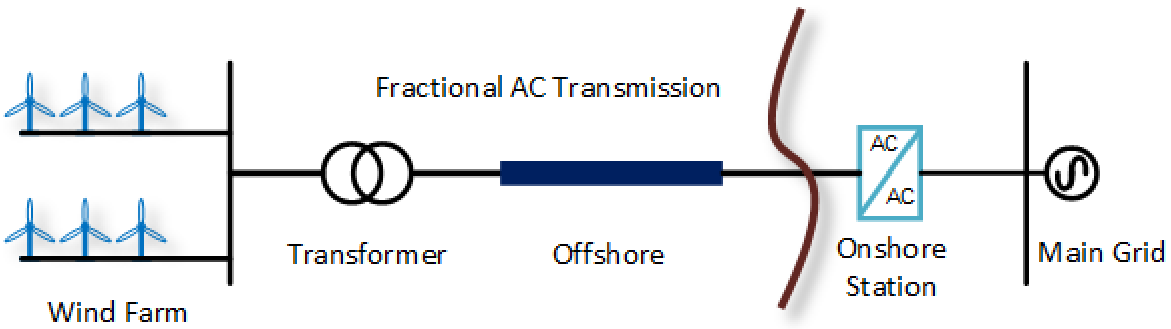

(a) Fractional frequency transmission connection

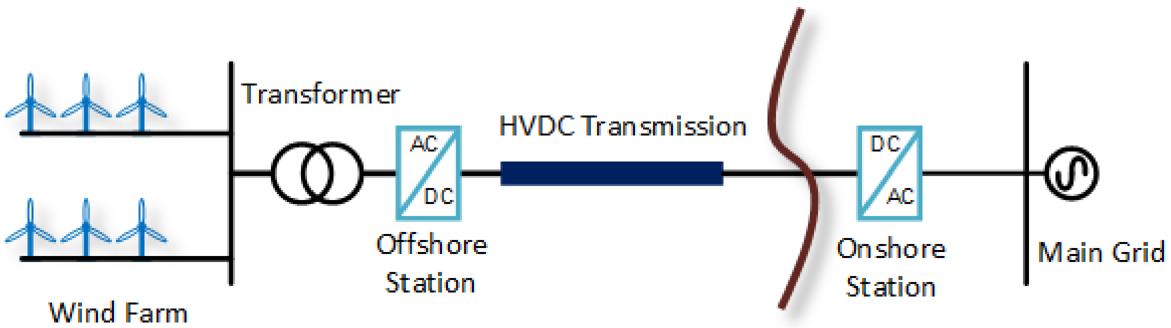

(b) HVDC transmission connection

Fig. 5.1 Schematic diagrams of offshore wind farm integration

5.2 Technical Performance Comparison of M^3C and BtB-MMC based FFOWPS

5.2.1 Structure and Principle of FFOWPS

The structure of FFOWPS is shown in Fig. 5.1.(a). For the AC system, the power transmitted by AC transmission line can be expressed by:

$$P_{AC} = \frac{U_S U_R}{X} sin\,\delta \tag{5.1}$$

$$X = 2\pi f_1 L \tag{5.2}$$

where P_{AC} is the active power transmit through the AC transmission line; U_S and U_R are the nominal line voltage of sending and receiving side; δ is the angle difference between the two voltages; $X$is the total reactance of the transmission line; f_1 is the fractional frequency, L is the inductance of transmission line.

As shown in (5.1) and (5.2) that the power of AC transmission line is inversely proportional to the frequency. The power capacity can be improved by lower the transmission frequency.

Besides, the voltage drop of a transmission line can be expressed by:

$$\Delta U\% = \frac{Q_{AC} X}{U^2} \times 100 \tag{5.3}$$

where Q_{AC} is the reactive power transmit through the AC transmission line;

From (5.3), the voltage drop of power transmission can be reduced by lower the transmission frequency. This is the working principle of FFTS. The $\mathrm{M^3C}$ and BtB-MMC is applied as the frequency converter for FFOPWS and discussed in this Chapter. The working principles of $\mathrm{M^3C}$ and BtB-MMC have been introduced and discussed in Chapter 3.

5.2.2 System Performance of M^3C and BtB-MMC for FFOWPS

The EMT models of M^3C and BtB-MMC have been developed in Sections 3.3.3 and 3.4.3 using the MATLAB/Simulink software, respectively. And the integrating control strategy has also been proposed and validated in SMIB simulation. In this section, the two frequencies of FFOWPS are set to 20 Hz and 60 Hz, respectively. The fractional frequency side of FFOWPS is integrated with the DFIG system via the transmission line, and the system frequency side is connected to the main grid, which is represented by an AC voltage source. For comparison purposes, the rated AC voltage of the two converters is both set to 33 kV. The number of submodules of two multilevel converters are both set to 40. The total output power from the DFIG system is rated at 30 MW. The transmission line distance between the DFIG and the frequency converter is set at 100 km. Full technology details can be found in Appendix A. The simulation outcomes of system performance are presented below.

As depicted in Fig. 5.2–5.4, the steady-state terminal voltages and currents of FFOWPS are measured at the DFIG terminal and two sides of the frequency converters.

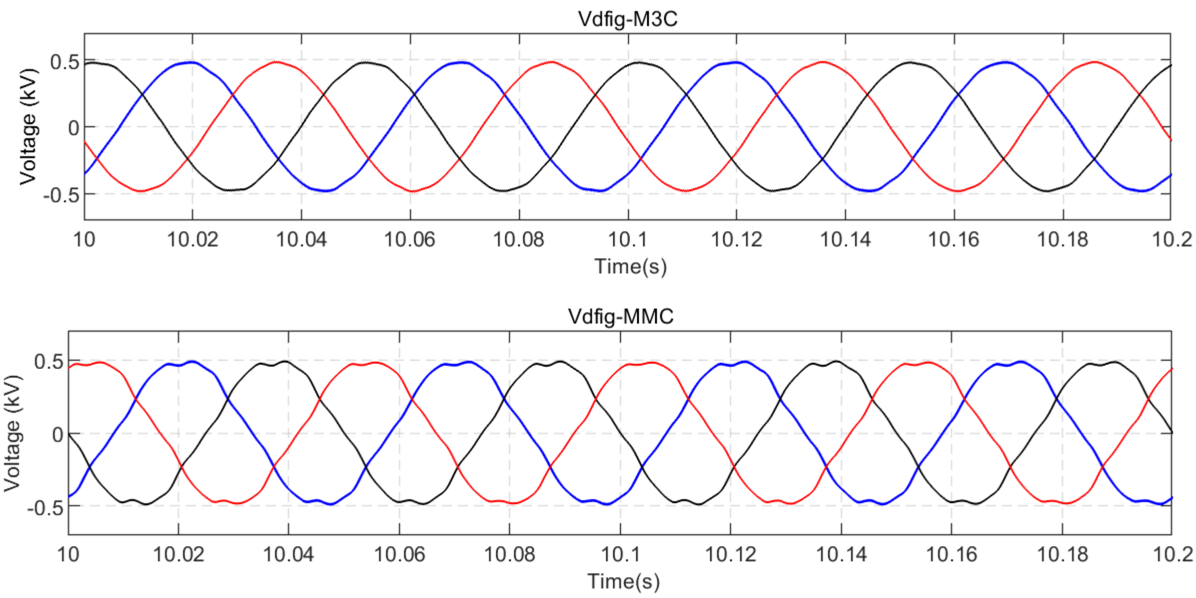

(a) DFIG terminal voltages of M^3C (up) and BtB-MMC (down) based FFOWPS

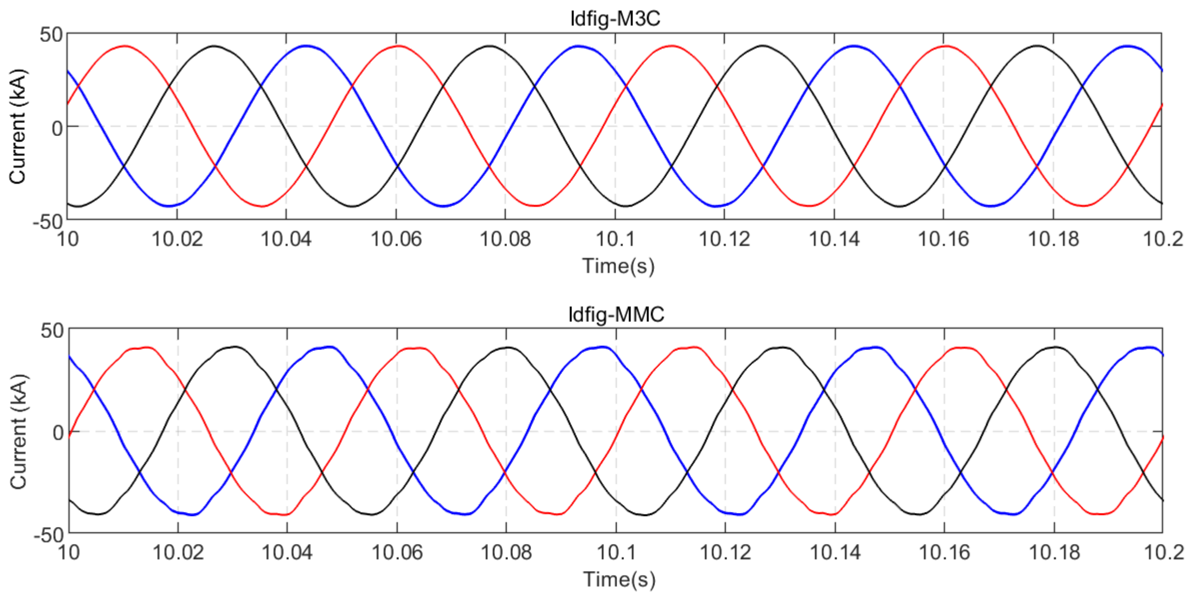

(b) DFIG terminal currents of M^3C and BtB-MMC based FFOWPS

Fig. 5.2 Voltage and current waveforms of DFIG terminal

As depicted in Fig. 5.2, the voltage and current waveforms at the DFIG terminals of the two systems are nearly identical and their harmonic performances are satisfactory without the addition of a filtering device.

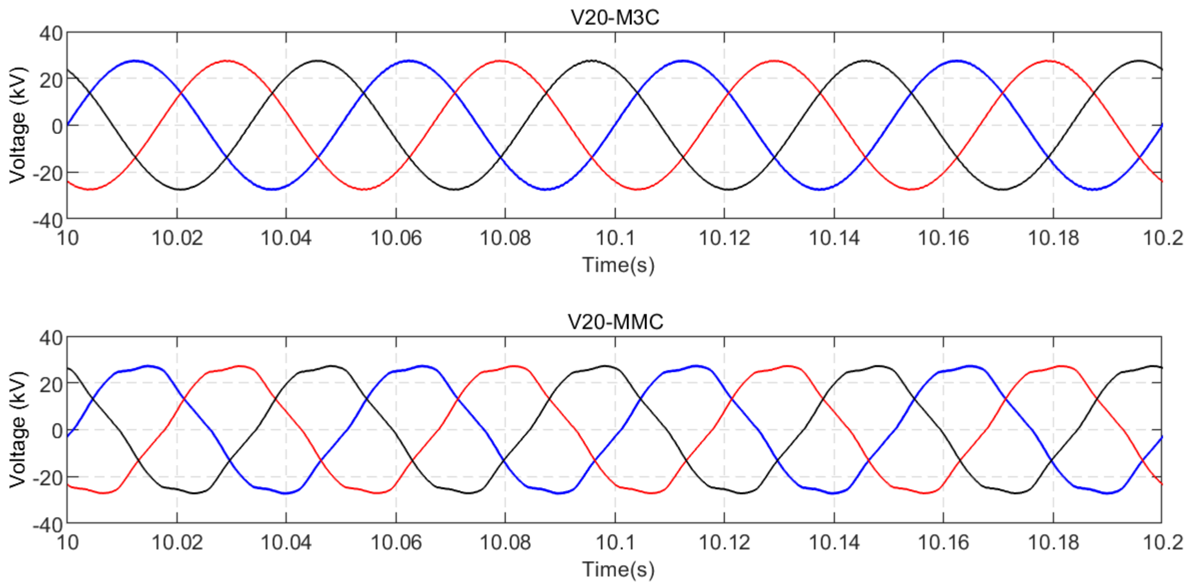

(a) Terminal voltages of M^3C (up) and BtB-MMC (down) at 20Hz Side

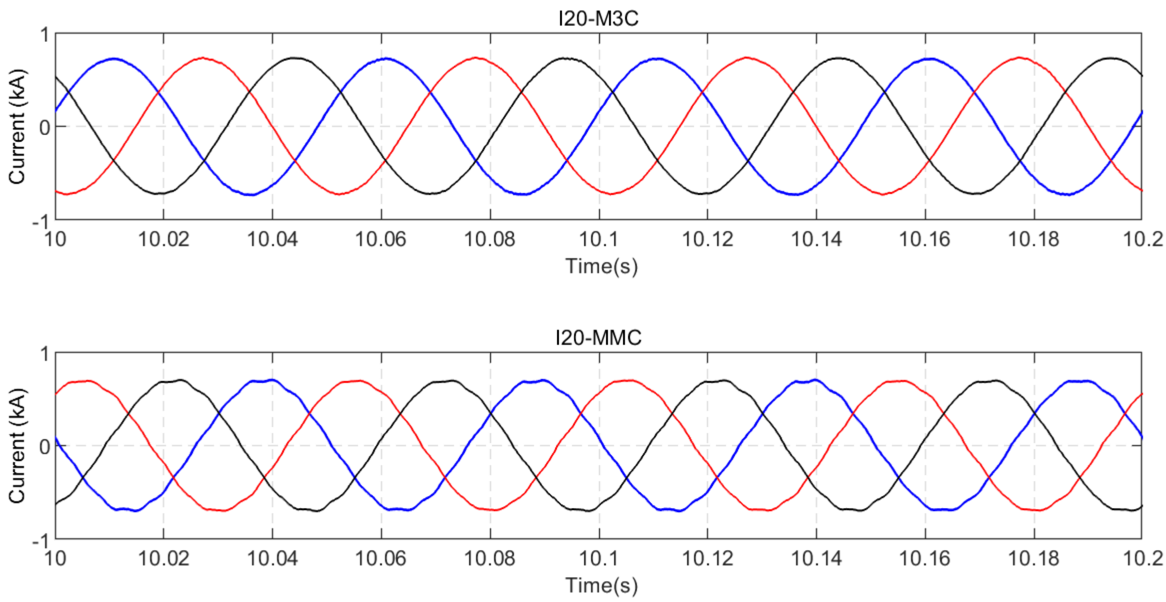

(b) Terminal currents of M^3C (up) and BtB-MMC (down) at 20Hz Side

Fig. 5.3 Voltage and current waveforms of 20Hz side terminal

Figure 5.3 presents the voltage and current waveforms at 20 Hz side. With the designed constant voltage and frequency control implemented at the fractional frequency side of the converters, the frequency converter absorbs the power from the DFIG smoothly while maintaining constant voltage and frequency. The voltage waveforms conform to the specified voltage level and frequency, and the current flows are stable, as shown in the figure.

Figure 5.4 illustrates the 60 Hz side waveforms, which are linked to the main grid. As depicted in the figure, the frequency of both quantities is shifted to 60 Hz while the voltage and current levels remain unchanged. Validation of the performance of two converters to be employed as frequency converters.

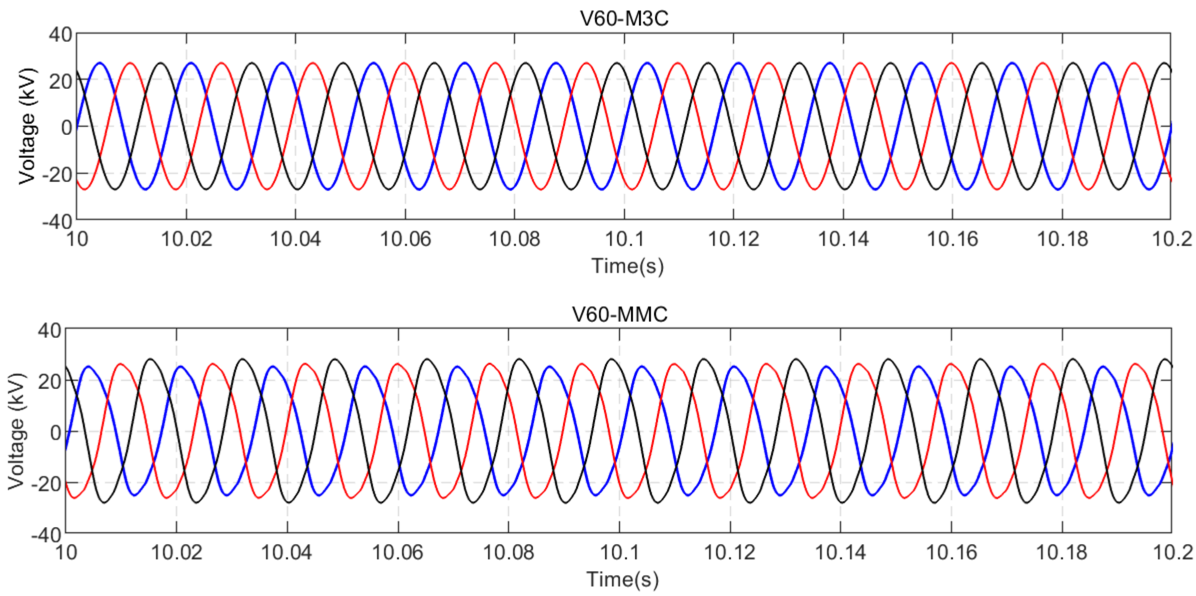

(a) Terminal voltages of M^3C (up) and BtB-MMC (down) at 60Hz Side

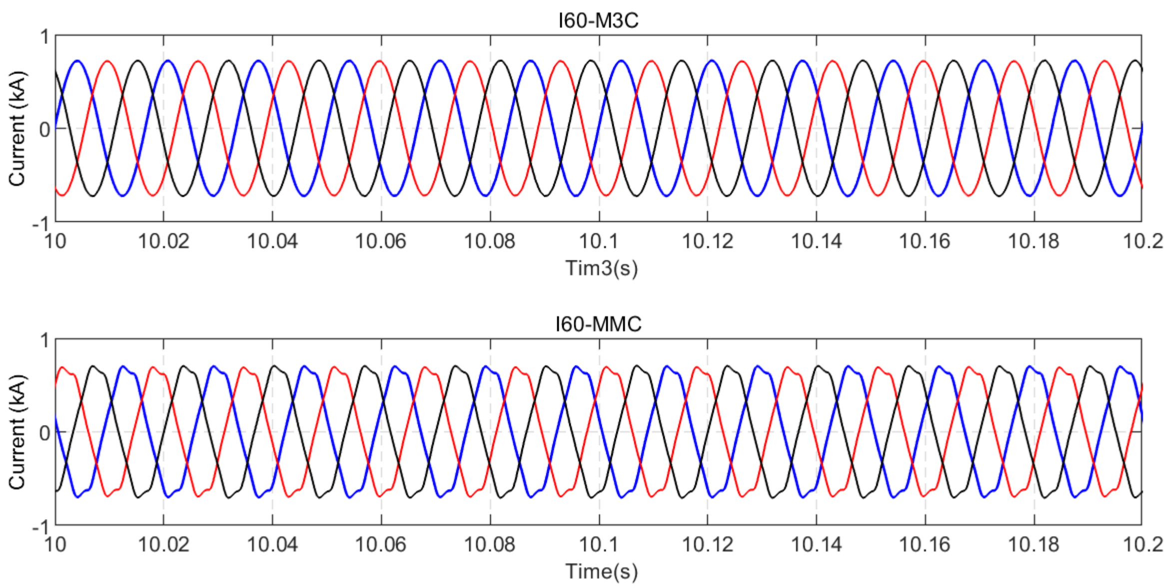

(b) Terminal currents of M^3C (up) and BtB-MMC (down) at 60Hz Side

Fig. 5.4 Voltage and current waveforms of 60Hz side terminal

In order to further evaluate the performance of two FFOWPS, disturbances are introduced. Figure 5.5 displays the power flow of the two systems with a 0.1 pu torque reference step change applied to the DFIG.

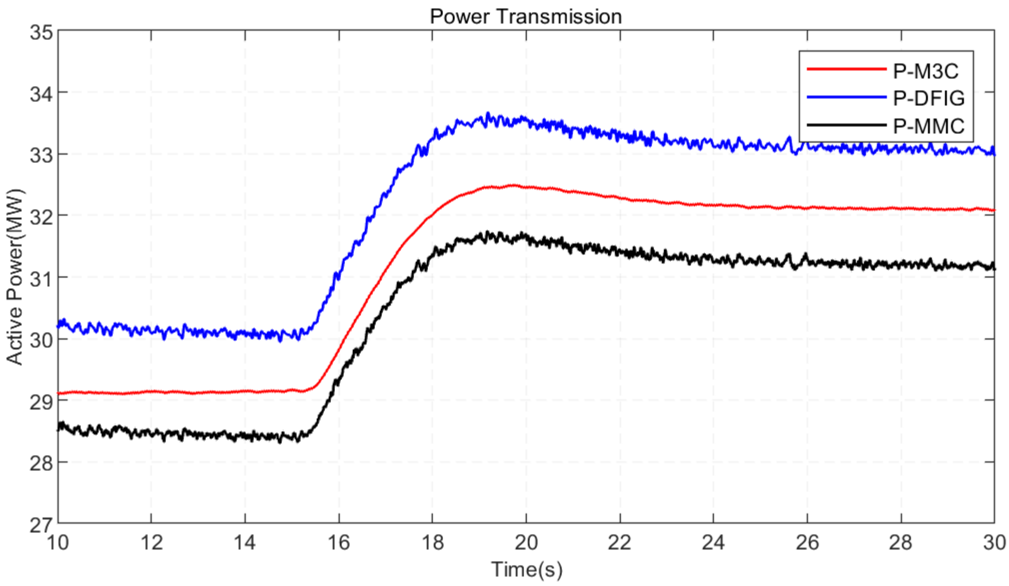

Fig. 5.5 Power transmission of FFOPWS

As seen in the figure, both frequency converters exactly track the power flow from DFIG. Due to the fact that BtB-MMC contains two converter stations with greater power electronics losses, the power loss of BtB-MMC is slightly higher.

Two FFOWPS are configured with a three-phase ground fault located at the 20 Hz side terminal and lasted from 15.02s to 15.05s. In Fig. 5.6, the voltage, current and power flow waveforms are displayed. As demonstrated, both systems promptly recovered from the fault, thus validating their performance as the frequency converter for FFOWPS.

In terms of their technical performance, both frequency converters are adequate for FFOWPS. Both systems voltage and current waveforms are of high quality, and their power transmission capabilities are satisfactory. There is a small variation in power loss because BtB-MMC has greater power electronics losses. To further compare two power converters, the following section provides a economic analysis.

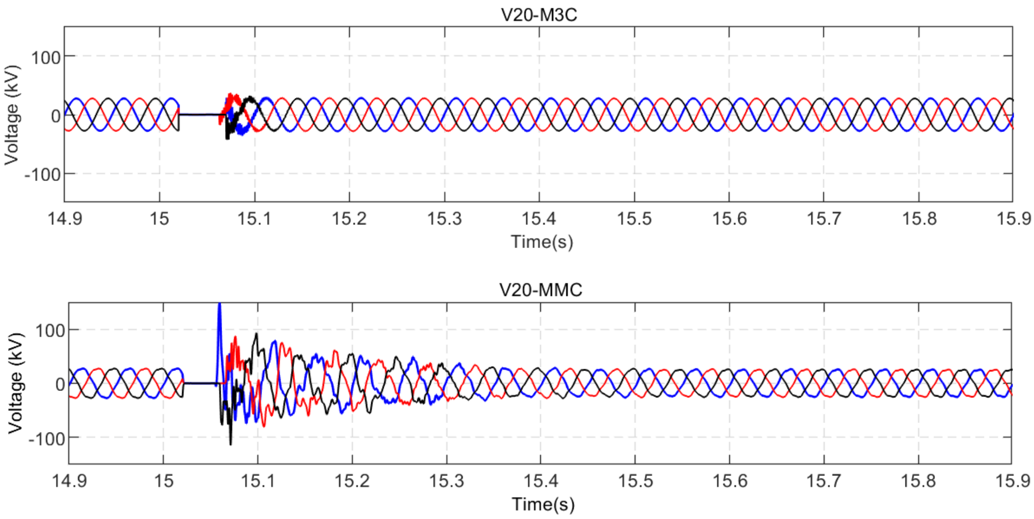

(a) Terminal voltages of M^3C (up) and BtB-MMC (down) at 20Hz Side

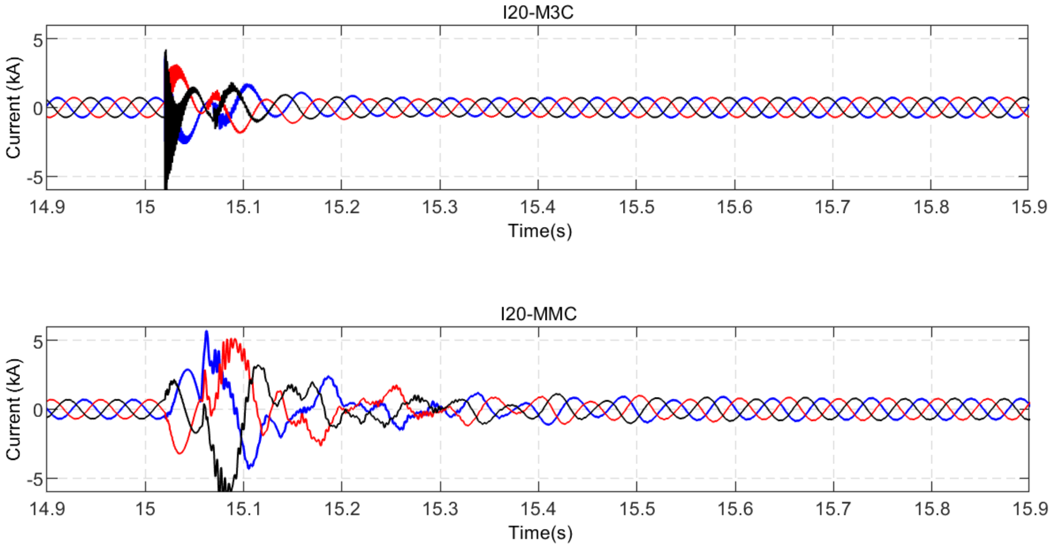

(b) Terminal currents of M^3C (up) and BtB-MMC (down) at 20Hz Side

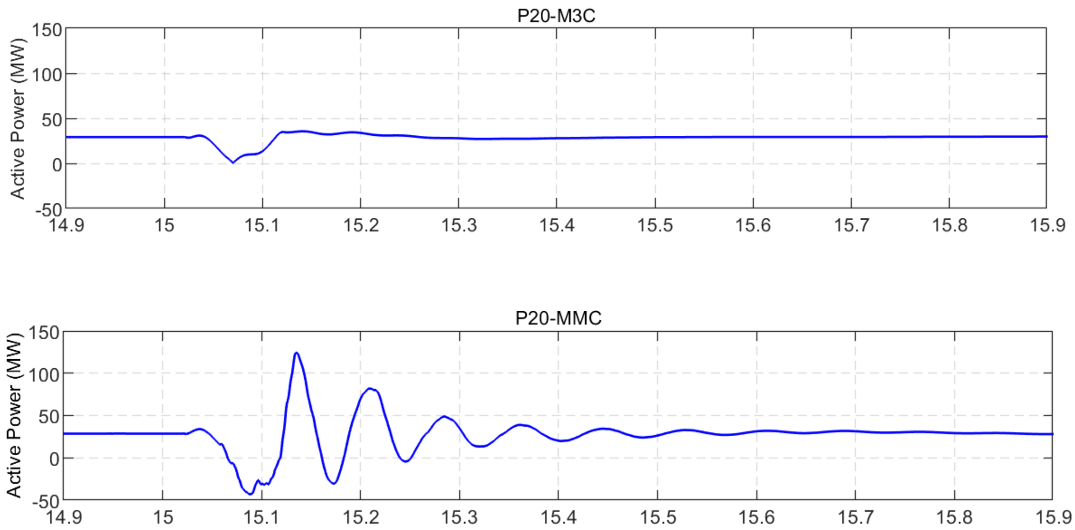

(c) Power flow of M^3C (up) and BtB-MMC (down)

Fig. 5.6 Performance of FFOWPS under large disturbance

5.3 Cost Components of FFOWPS

The total cost of the FFOWPS can be broken down into the expense of its individual components: the wind turbine for power conversion, the transformer for voltage boosting, the submarine cable for power transmission, and the converter station for grid integration. Each component can also be subdivided based on whether costs are incurred prior to or under serving. They are capital costs, unavailability costs, O&M costs, and power loss costs. This can be mathematically expressed as [98]:

$$C_{TOT} = C_{CAP} + C_{UA} + C_{O\&M} + C_{PL} \tag{5.4}$$

where C_{TOT} is the total costs of FFOWPS C_{CAP} is the capital costs of the components of FFOWPS, C_{UA} is the unavailability costs, $C_{O\&M}$ is the O&M costs, and C_{PL} is the power loss costs. Except for the capital costs considered as the initial investment, the rest three type of costs are incurred during operation and throughout the FFOWPS lifetime. Considering the time value of money, (5.5) is used to convert the long-term expenses over the lifetime of the wind power system to a net present cost.

$$C_{NPC} = C_{AN} \frac{(1+i)^n - 1}{i(1+i)^n} \tag{5.5}$$

where C_{AN} is the time value of the long-term cost in annual; n is the FFOWPS service years; i is the value discount rate.

5.3.1 Capital Cost

Typically, the primary cost of a wind power generator is incurred throughout the manufacturing, transport, and installation processes, as well as during foundation construction. For reasons of confidentiality, wind turbine generator cost data is sparse in the public domain, and it may vary from different suppliers and different projects. The economic data is collected and summarised from relevant literatures, and displayed in graphs and tables.

The general cost of the offshore wind turbines can be estimated as £1m/MW [99], which is the average cost and ignored the type of wind generators. In this research, the DFIG wind turbine is studied and from [100], the cost of DFIG is approximated at £1.8m/MW, and with the development of wind turbine technology, the cost is expecting to reduce. Fig. 5.1 shows the cost components of a typical DFIG wind turbine [101]. As it shown, gearbox is the main cost component which makes up 17% of the total cost. As discussed in previous chapters, wind implementing the DFIG in low frequency power system, the gearbox can be simplified and the cost should be reduced. Furthermore, the reduce size of gearbox also reduce the size and weight of tower and hub of the wind turbine. Based on [22], approximated 5.2% of cost should be reduced by applying the DFIG to FFOWPS.

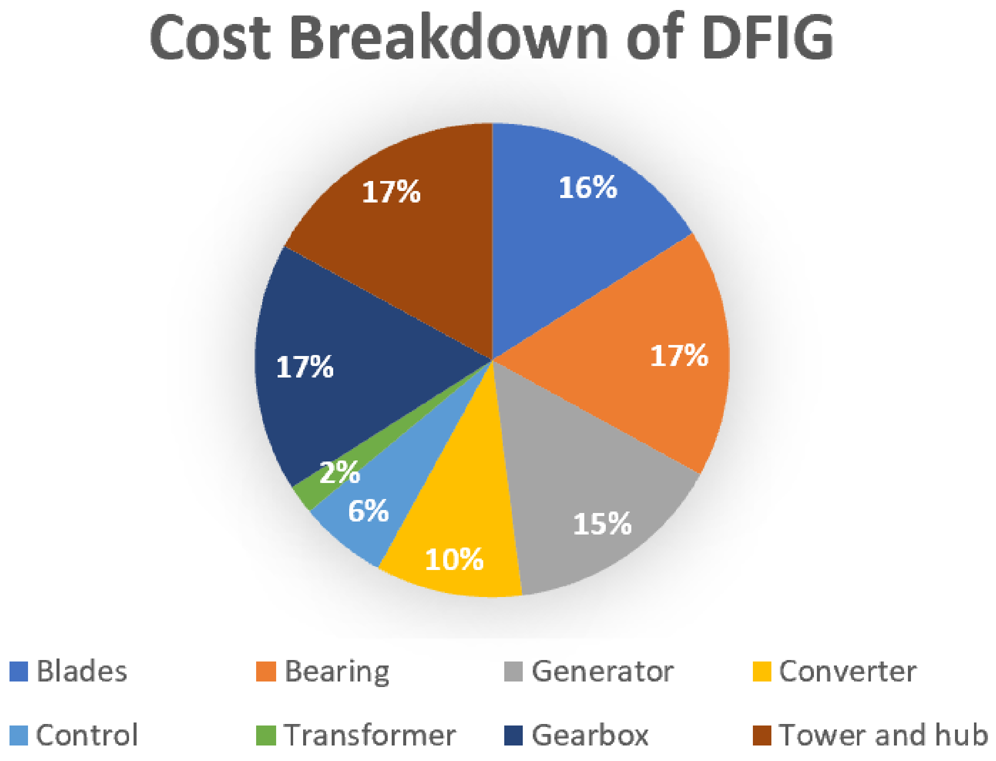

Fig. 5.7 Cost breakdown of DFIG

Based on the calculation in a Northseagrid report [102], average capital costs of the offshore station for transformer and converter are provided and tabulated in Table 5.1. At the same nominal rating, fractional frequency transformers are typically more costly and larger. According to the calculation in [103], the fractional frequency transformer would be around 75% more expensive than general transformer. Capital costs for an onshore converter station include the expense of property, construction work, and valves, etc. Due to the fact that MMC can employ half bridge sub-modules whereas M^3C must be applied with full bridge sub-modules, the overall spend of the M^3C converter station is increased about 20% compared to the converter station utilised with half bridge submodule valves [104]. However, there are rectifier and inverter converter stations for BtB-MMC with six arms installed in each station. Besides, the rectifier station would have to be installed offshore if the HVDC transmission technologies applied. There is no offshore station for M^3C based FFOWPS, and all nine arms are positioned onshore. In a simple calculation, the M^3C converter station is approximately 80% more expensive than the single BtB-MMC onshore converter station.

For standardisation purposes, only specific voltage levels are available for cables. Table 5.1 lists the capital costs of different types of cable derived from [93]. The selection of an submarine cable is dictated by the transmission distance and power capacity of the generation system. When discussed in previous chapters, as the charging current consumes a greater proportion of the cable's rating, the maximum transmittable active power for HVAC cables falls with increasing distance. FFTS is intended to alleviate the primary drawback of HVAC. Based on (5.1)-(5.2), FFTS operates at one-third the frequency drastically reduces the required charging current, hence increasing transmission capacity. With reactive power compensation, FFTS is able to transmit 500MW of energy over 400 km with a 220 kV voltage level, as demonstrated in [105]. This capability can satisfy the majority of distance needs for offshore wind energy systems, and greater voltage levels can further boost the transmission power capacity. Costs for reactive compensation vary based on the method of compensation and location of the equipment. In this study, it is assumed that two reactive power compensation equipment with same capacity is supplied by both ends of the transmission system. The costs of compensation can be found in [106]. As the costs are roughly linearly dependent on distance, it is assumed the first-order linear cost functions are used to calculate the compensation cost.

Table 5.1 Unit capital costs of FFOWPS main components

Components		Unit capital cost
DFIG		£1.8m/MW
DFIG operated in FFTS		£1.7m/MW
Offshore transformer station		£0.129m/MW
Offshore transformer station in FFTS		£0.194m/MW
Offshore BtB-MMC converter station		£0.254m/MW
Onshore BtB-MMC converter station		£0.107m/MW
Onshore M^3C station		£0.171m/MW
Fractional frequency AC cable	132 kV (0-300MW)	£0.86m/km
	220 kV (300-600MW)	£1.00m/km
	400 kV (600-1000MW)	£2.15m/km
DC cable	150 kV (0-500MW)	£0.785m/km
	300 kV (500-1000MW)	£1.015m/km

5.3.2 Unavailability Cost

The quantity of energy not delivered to the power grid determines the unavailability cost of the power system. The IEC Standard 61400 [107] defines the unavailability of the wind energy generation system as the percentage of the system unavailable time and the duration of the examined period, which is given by:

$$R_{UA} = \frac{t_{UA}}{t_{year}} \times 100\% \tag{5.6}$$

where R_{UA} is the rate of the unavailability of the offshore wind energy generation system; t_{UA} is the unavailability hours of the system accounted in one year; t_{year} is the total hours accounted as one year, which is defined as 8760 hours in this study. It should be noted that the t_{UA} is only considered the unexpected downtime of the system and not accounted the planned maintenance out of service time. And for simplification, it is assumed that only fault can occur simultaneously in the system, as system is assumed not operating when one component experience a fault. In that case, the total unavailability of the system is defined by adding the unavailability of each individual component. The total unavailability rate of the FFOWPS is given by:

$$R_{tot\_UA} = R_{wt\_UA} + R_{tran\_UA} + R_{cab\_UA} + R_{cov\_UA} \tag{5.7}$$

where R_{wt_UA} is the wind turbine unavailability rate; R_{tran_UA} is the transformer unavailability rate; R_{cab_UA} is the undersea cable unavailability rate; R_{cov_UA} is the converter unavailability rate. Based on (5.4), the total energy not delivered can be derived, and the unavailability cost is the multiplication of the not supplied power and energy price, given by:

$$C_{UA} = R_{tot\_UA} \times \mathrm{CF} \times P_{rated} \times EP_{wind} \times t_{year} \tag{5.8}$$

where CF is the capacity factor; P_{rated} is the rating of the offshore wind power generation system; EP_{wind} is the average energy price of the offshore wind power.

The relevant data of the unavailable hours of wind turbines are extracted from [108, 109] and listed in table 5.2, which is represented with the annual failure rate and downtime, and the unavailable hour t_{UA} of one year can be calculated by times the failure rate and downtime.

Table 5.2 Unavailability data of the wind turbines

Components	Failure Rate (per year)		Downtime (hours)
	DFIG	PMSG	
Gearbox	0.185	N/A	1008
Generator	0.123	0.046	768
Rotor Blade	0.16	0.16	1008
Converter Electronics	0.106	0.593	48

It can be seen from the table, for DFIG, the gearbox is the main unavailability components with highest failure rate and downtime hours. As stated in previous chapter, the gearbox structure of low-frequency wind turbine generators can be greatly simplified. Consequently, the failure rate of the gearbox would likewise decrease, and it is assumed that the decrease is one-third of the general rate as same as the reduction of frequency. For PMSG, the advantage is that it does not suffer from gearbox failure, however, the converter electronics failure rate is extremely high. The higher rate of converter failure is due to the fact that PMSG uses a fully rated converter. compared to the partially rated converter used by DFIG, fully rated converters are more likely to break.

Transformers operating at fractional frequency are a proven technology, and it is thought that they work with the same level of dependability as transformers operating at standard grid frequency considering it has been employed in fractional frequency railway networks for quite a long period [110]. The failure rates and downtime data of the cables and transformer are extracted from [102] and shown in Table 5.3.

Table 5.3 Unavailability data of transformers and cables

Components	Failure Rate (per year)	Downtime (hours)
Transformer	0.024	2160
AC Cable/100km	0.1114	1440
DC Cable/100km	0.1114	1440

For the purpose of simplicity, it is assumed that the unavailability of multilevel converters is proportional to the number of power electronic submodules. However, onshore and offshore converter stations should be evaluated independently. Unavailability data for onshore converter stations are derived from a comprehensive GIGRE investigation of the global dependability of a significant variety of HVDC networks. [111]. Data for offshore converter stations on existing offshore wind farm projects from the past three years is collected, and an average unavailability rate is determined [112]. Table 5.4 details the unavailability values of each components in FFOWPS.

Table 5.4 Unavailability value of components in FFOWPS

Components		Value
Wind turbines unavailability	PMSG	2.57%
	DFIG	5.11%
	DFIG in FFTS	3.69%
Converter unavailability	Onshore BtB-MMC	0.35%
	Offshore BtB-MMC	0.8%
	M^3C	0.52%
Transformer unavailability		0.59%
Cable unavailability		0.18%

5.3.3 O&M Cost

Multiple activities might result in O&M expenses for offshore wind energy installations [113]. Common sources of O&M expenditures include labour, accounting fees, changed components, vessel expenses, rent, and insurance cost. Existing offshore wind farm operations and maintenance (O&M) cost information is not publicly available, which presents a challenge. In addition, the O&M expenses for every offshore wind energy installation might vary based on the maintenance regularity, the availability of skilled labourers and ships, and the atmospheric and ocean conditions. Since typical statistics in economic studies could not be accurate, the annual O&M cost for each element could be approximated as a proportion of the component's initial investment, which is given by [114]:

$$R_{O\&M} = \frac{C_{O\&M\_indivi}}{C_{CAP\_indivi}} \times 100\% \tag{5.9}$$

where $C_{O\&M\_indivi}$ is the annual O&M cost of individual equipment and C_{CAP_indivi} is the capital cost of individual equipment components. For different equipment components, the $C_{O\&M\_indivi}$ is varied depended on its technologically mature and operation mode, for example, he offshore wind turbine requires more maintenance than the transformer due to the fact the wind turbine is relevantly new technology and has the moving mechanical part. The related O&M data are extracted from [102, 115] and listed in Table. 5.5.

Table 5.5 O&M data of FFOWPS

Components	O&M Ratio (year)
Wind Turbine	3.4%
Offshore Transformer	0.15%
Undersea Cable	2.5%
Offshore Converter Station	2%
Onshore Converter Station	0.7%

5.3.4 Power Loss Cost

The power loss cost has the same mathematic expression as the unavailability cost, which can be expressed as the multiplication of lost power and energy price, given by:

$$C_{PL} = R_{tot\_PL} \times P_{rated} \times EP_{wind} \times t_{OP} \tag{5.10}$$

where R_{tot_PL} is the ratio of the total power loss of each component and t_{OP} is the annual operation time of the system. The R_{tot_PL} is given by:

$$R_{tot\_PL} = R_{wt\_PL} + R_{tran\_PL} + R_{cab\_PL} + R_{cov\_PL} \tag{5.11}$$

where R_{wt_PL} is the wind turbine power loss ratio; R_{tran_PL} is the transformer power loss ratio; R_{cap_PL} is the submarine cable power loss ratio; and R_{cov_PL} is the converter power loss ratio. The relevant data is collected from [106, 116-118] and listed in Table. 5.6.

Table 5.6 Power loss data of FFOWPS

Components		Power Loss
Wind Turbines	PMSG	6.4%
	DFIG	5%
	DFIG in FFTS	3%
Converters	Offshore BtB-MMC	1%
	Onshore BtB-MMC	1%
	M^3C	1.95%
Submarine Cables	AC/100km	3%-5%
	DC/100km	0.5%-2.5%
Transformer		0.8%

For different wind turbines, PMSG applied with a full rating converter, which contributes the majority power loss of system due to the inefficiency of primary low levels converter. For DFIG, mechanical loss, specifically the loss from gearbox, comprises a significant share of total wind turbine loss. Still, same as the previous definition, the gearbox loss of a DFIG working at fractional frequency is approximately one-third that of the original. Switching loss and conduction loss are the two primary forms of power loss in a converter power electronics. The BtB-MMC uses half bridge sub-modules, and the power loss of each converter station is approximately 1% of the system power rating. Submodules applied to M^3C are full bridges, which provides a greater loss. The full bridge and half bridge valves have the same switching loss, however, the power loss to conduct full bridge submodule valve is double that of half bridge submodule valve. In that case, the power loss of M^3C is assessed to be 1.95%. The AC cable and DC cable have distinct power loss ratios. The active current passing through the cable is the primary source of power loss of DC cable, whereas for AC cable, the cable capacitance produces the active and reactive current which enlarge the power loss. Consequently, AC cable has a greater loss than DC cable. Depending on the voltage level, 100 km of AC cable suffers a 3% to 5% power loss, while DC cable has only 0.5% to 2.5% at the same distance. In transformers, the heating current in the windings and the magnetising current in the core account for the majority of power losses. The transformers have a high efficiency and a power loss ratio of 0.8% on average due to their technologically advanced benefits. For the sake of simplicity, the difference in the transformer's power loss ratio when running at fractional frequency versus system frequency is disregarded.

5.4 Cost analysis and Comparison of FFOWPS

In last section, the cost components of FFOWPS are discussed, along with the pertinent data and mathematical formulae. In this section, the cost analysis of M^3C based FFOWPS and BtB-MMC based FFOWPS are derived. In addition, a BtB-MMC based HVDC economic model is built for comparative research. Components that have a substantial impact on the system's total cost are underlined. A cost constituents analysis of M^3C based FFOWPS and BtB-MMC based FFOWPS is shown first, followed by the cost effectiveness comparison between M^3C based FFOWPS and BtB-MMC based HVDC.

Table 5.7 Economic Parameters for Cost Analysis

Items	Parameters
Power rating	500MW
Transmission distance	100km
Discount rate	5%
Power Plant life time	20 years
Capacity factor	40%
Annual operation time	2500 hours
Wind energy price	£50/MWh

5.4.1 Cost constituents of FFOWPS

The relevant economic data extracted from [119-121], and the rating parameters of proposed FFOWPS system are listed in Table 5.7. Based on the economic data and cost equations (5.4) – (5.11), the cost breakdown of M^3C based FFOWPS and BtB-MMC based FFOWPS can be calculated. The cost constituents of two systems are shown in Fig. 5.2 (a)-(b).

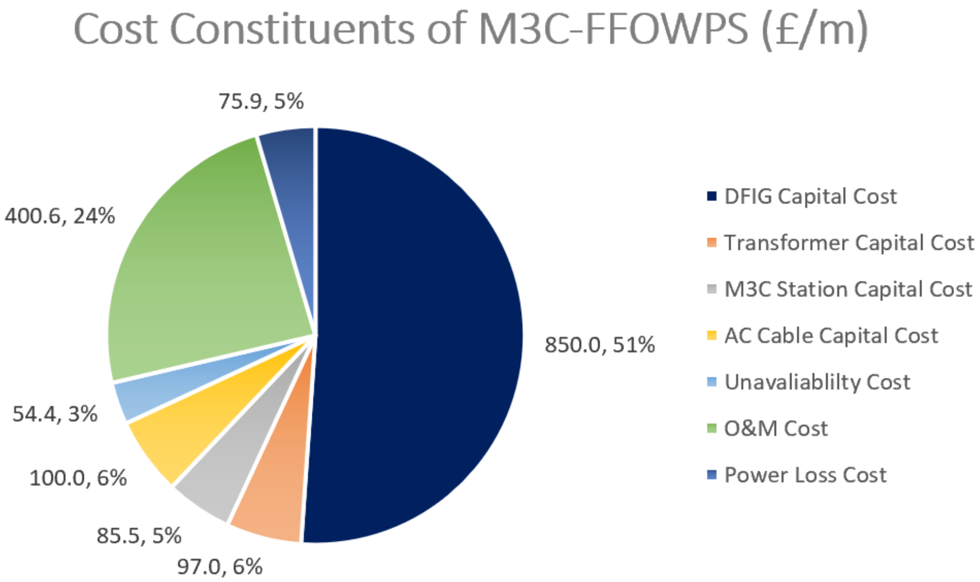

(a) Cost constituents of M^3C based FFOWPS

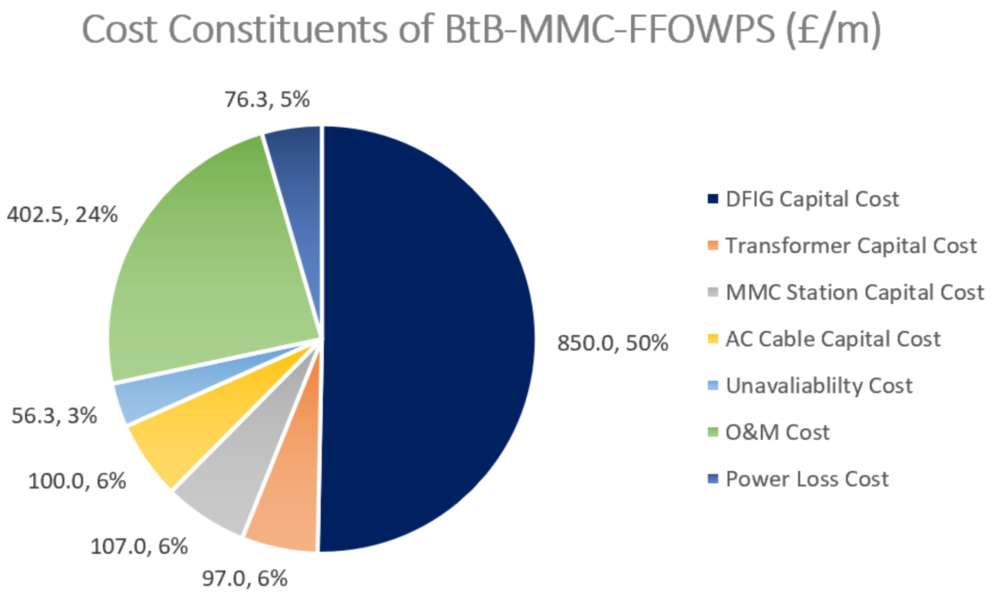

(b) Cost constituents of BtB-MMC based FFOWPS

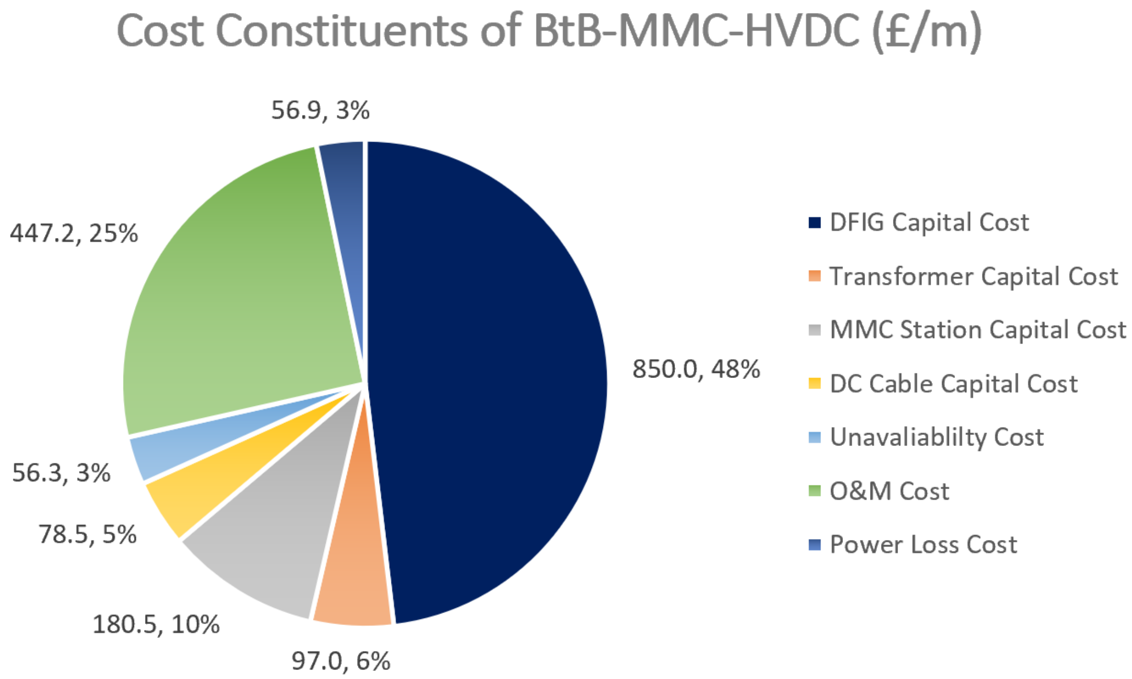

(c) Cost constituents of BtB-MMC based HVDC offshore wind power system
Fig. 5.8 Cost constituents of offshore wind power integration technologies

It is obviously the capital cost of DFIG wind turbine is largest cost contributor, take up around 50% overall project cost of FFOWPS. The second in importance are the O&M costs, which account for roughly 24%. This number is the total value accounted the net present value calculated with the 20 years operation lifetime of the offshore wind farm, and this principle is implemented to all other time-related expenses, such as the cost of system unavailability and the cost of power loss. The cost of power loss for both technologies is about 5%, while the cost of unavailability comprises the smallest portion. Only the capital cost of converter station has identifiable difference due to the fact BtB-MMC technology has larger stations site. For further comparison, the cost constituents of MMC-HVDC offshore wind power integration technology is calculated in Fig. 5.8 (c). It is obviously the cost of MMC station is further increased due to the offshore converter station construction required, so does the O&M costs. In contrast, the cable cost and power loss are reduced due to the using of DC cable. To sum up, the total expense of FFOWPS is largely determined by capital expenses, with wind turbines being the most expensive component. Therefore, it is crucial to do research on how to reduce the capital cost of wind turbines to make offshore wind power technology more competitive.

5.4.2 Cost-Effectiveness Transmission Distance

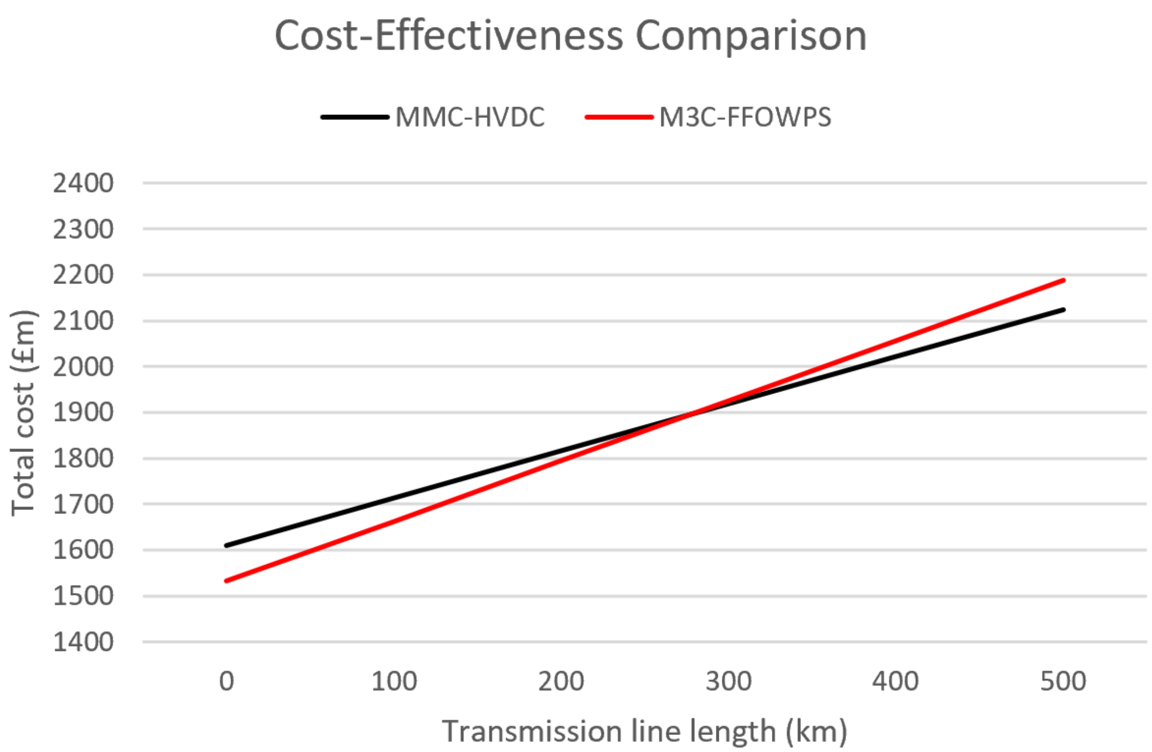

Fig. 5.9 Cost-Effectiveness Comparison of FFOWPS and HVDC vs Distance

In this subsection, the economical effective transmission distances for M^3C based FFOWPS and BtB-MMC based HVDC are evaluated for an DFIG based offshore wind farm system with a rated capacity at 500 MW. The crossover point is identified, and the cost differential is analysed. The overall expenses of the two methods are plotted against the transmission distance in Figure 5.9. As it shown, the crossover point occurs at a transmission distance of 280 km, before which M^3C based FFOWPS is the less expensive option, and BtB-MMC based HVDC is the less expensive option for transmission distances more than 280 km. To analyse the cause, two points are chosen at 250 km and 350 km, which are slightly shorter and longer than the crossing point, and the variations in capital, unavailability, O& M, and power loss costs are depicted at each point in Fig. 5.10. To be specific, the value in the graph is calculated by the cost of BtB-MMC based HVDC minus M^3C based FFOWPS, so a negative value indicates that M^3C based FFOWPS is more costly.

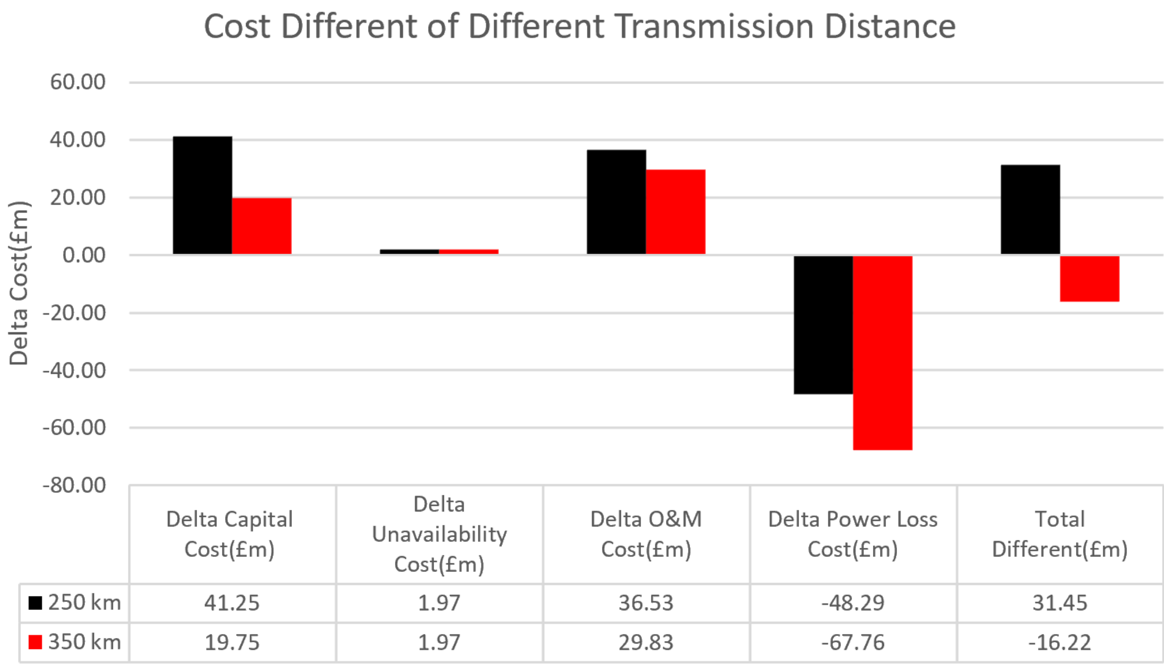

Fig. 5.10 Cost differences of different transmission distance

Based on the previous discussion, at the shorter distance, the capital cost of converter stations have a greater impact on the overall cost. At a distance of 250 km, the converter station of BtB-MMC based HVDC has a higher capital cost due to the additional offshore converter station, which results in a greater disparity in capital costs. When the transmission distance extended to 350 km, the AC cable of M^3C based FFOWPS becomes more expensive, and the cost difference decreased. Besides, the AC cable has a greater power loss than the DC cable, which is the primary disadvantage. The largest positive change in O&M costs is again attributable to the offshore converter plant. The M^3C station is placed on land, making its operation and maintenance significantly less dependent on weather and sea conditions, as well as the availability of vessels. However, as transmission distance increases, so does the O&M cost of AC cable. In conclusion, at a shorter distance, the cost difference of capital, unavailability, and O&M expenses is positive and enough to cancel the negative power loss costs, resulting in a positive total delta cost, which means the M^3C based FFOWPS is more cost-effective. Nonetheless, as the transmission distance increases to 350 km, the shortcomings of AC cable become more apparent in every aspect. The expansion is so substantial that it nullifies out the benefits of the onshore converter station. Therefore, the total delta cost becomes negative and the BtB-MMC based HVDC is a more economical option for long-distance transmission.

5.5 Summary

This chapter provides a comprehensive techno-economic study and comparison of M^3C and BtB-MMC for the integration of the offshore wind farm. The technical performance of both technologies is described first, and the reliability of both frequency converters for FFTS integration can be validated. Therefore, it is worthwhile to examine their economic profiles further in order to identify the most cost-effective option. The economic analysis approach and the total cost decomposition have been implemented. The cost components including the capital cost, unavailability cost, O&M cost, and power loss cost have been explored in detail separately. The economic research revealed that about 50% of the project total cost is taken up by the primary expense of the wind turbine. O&M expenditures comprise around 24% of the total cost and are the second most influential factor in the analysis. It has been demonstrated that M^3C based FFOWPS is a very promising option for offshore wind power integration at a medium transmission length no longer than 280km compared to HVDC. And it also has been determined that three issues impede its cost-effectiveness, including the expensive undersea AC cable, greater power loss, and a costly offshore transformer plant. Compared to M^3C based FFOWPS, the offshore converter station is the primary negative factor for BtB-MMC based

HVDC technology. It has a high capital cost, a greater rate of unavailability, more complex maintenance than the onshore plant, and additional power loss from the converter. Nevertheless, the BtB-MMC based HVDC is still the optimum alternative for long-distance power transmission due to the amazing benefits of DC cable, which include a reduced capital price, no requirement for reactive power compensation, and minimal power loss.

Chapter 6 Conclusions and Future Work

6.1 Conclusions

In an attempt to reduce carbon emissions and fossil fuel usage, nations are investing considerable effort in producing renewable energy. Since the 1990s, wind energy generation has flourished, with offshore wind power development being particularly dramatic. The advantages of offshore wind power include high and abundant resources, appropriateness for large-scale utilization, and minimal influence on community areas. From the previous literature, three predominant transmission systems for offshore wind farms have been identified. HVAC is a reliable and cost-effective method for the integration of short-distance offshore wind generation systems. It has been utilised in the majority of wind power plants to reduce technical risk and increase the profitability of costly offshore wind projects. However, the capacitive charging current limits the transmission distance of HVAC, thus it is not capable of connecting the future far ocean offshore wind power generation to the grid. The HVDC technology is a viable option for long-distance power transmission and has been utilised by a number of power integration projects. FFTS can also alleviate the drawbacks of HVAC and is considered a good contender for offshore wind energy applications. In Chapter 1, three transmission technologies have been compared, and the relatively new FFTS technology is highlighted. A brief overview of the power electronic technologies for FFOWPS adaptation has been provided. The motivations, objectives, and contributions of this PhD research are also given.

The M^3C is the fundamental component of FFOWPS and is recognised as the relatively new and advanced AC/AC converter technology. It has the advantages of substantial controllability, adaptable scalability, and high efficiency. Chapter 2 has reviewed relevant topics in the previous studies and has provided an overview and essential information for subsequent chapters. The applications and control strategies of M^3C have been reviewed first to give a comprehensive picture of the AC/AC converter technologies. Then, the fundamental concept of the small signal stability analysis has been presented, and a portion of the existing literature on wind turbine and power converter small signal modelling has been discussed. Existing economic analyses of FFOWPS have been reviewed, and different kinds of economic analysis methods have been presented and discussed.

In Chapter 3, the system structures, working principles, and control strategies of the power electronics for FFOWPS adaptation were extensively discussed, laying the groundwork for the small signal modelling of FFOWPS. To provide a thorough description of the M^3C control strategy, the general control strategies for DFIG, M^3C, and BtB-MMC have been discussed. An integration control strategy for M^3C to connect wind generationhas been first developed in this thesis to prevent control conflicts between wind power systems and power converters. The simulation test system utilised in this doctoral study was developed in accordance with the system structure and methods of control. The performance of the M^3C and BtB-MMC as a frequency converter has been examined, and the effectiveness of the designed control strategy for integration has been validated.

In Chapter 4, the design of the small signal model for FFOWPS has been implemented. Due to the fact that DFIG-M^3C FFOWPS is a promising option for offshore wind plant development, the small signal model that that takes into account all essential components is necessary in order to examine its influence on power grid. The small signal model of whole FFOWPS has been designed and provided in this thesis, which is in modular structure and can be easily interfaced with different external AC system and internal control system. The dynamic of DFIG, M^3C and the interface between two system are modelled. With the eigenvalue based small signal stability analysis, the proposed model can provide valuable guidance regarding controller parameter and submodule capacitance selection. Based on the results of eigenvalues, the PI control parameters can be selected with care, as a large or small value of the proportional gain of the DC voltage controller can both result in poor damping. In addition, the damping of the sub-module capacitance related modes can be inadequate if the capacitor value is selected improperly. With optimised control parameters, the system's oscillation modes are reduced from 7 to 4, and system damping ability can be increased. The small signal model is advantageous for future system stability research and controller development.

In Chapter 5, the technical and economic aspects of the DFIG-M^3C based FFOWPS are investigated. The M^3C and BtB-MMC frequency converters for FFOWPS are examined and contrasted in terms of their technical performance. The conclusion is that both technologies have reliable performance for FFOWPS. In that case, to further study the performance of two technologies in economic aspects, a cost analysis model for FFOWPS was developed that accounted for detailed cost components including the capital, unavailability, O&M and power loss costs of the system. According to the main cost elements pie chart generated from the cost analysis, the primary cost of the wind turbines is the most expensive component, which formed almost 50% of project cost, followed by the long-term O&M expenses of the entire project that took up 24% of total cost. The only difference between M^3C FFTS and BtB-MMC FFTS is the frequency converter, with M^3C being a more cost-effective option than an AC-DC-AC converter. A detailed cost comparison between M^3C based FFOWPS and BtB-MMC based HVDC is presented. M^3C based FFOWPS has been found to be economically superior to BtB-MMC based HVDC at medium transmission distances. It has been determined that DFIG-M^3C FFOPWS is the more cost-effective transmission technology at distances of approximately 280 km.

6.2 Future Work

Possible of further studies can be continued as follows:

1. Chapter 3 develops the control strategy for integrating the M^3C with the DFIG system. The experimental simulation verifies the effectiveness of the control system, which is designed to maintain a constant voltage magnitude and frequency on the fractional frequency side of the M^3C. Future research could consider a modification to control the fractional frequency side voltage more flexible without interfering with the DFIG control system. Additionally, additional research could be proposed to incorporate the DFIG control system into the M^3C.
2. Analysis of small signal stability is a perennial topic of power system research. Small signal models of all the system's components are required for power system small signal analysis. A small signal model of DFIG-M^3C based FFOWPS accounted the dynamics of DFIG, M^3C, and interaction between two system has been developed in Chapter 4. The model has been designed with a modular structure and can be easily interfaced with various external AC system and internal control systems. The further action could be to investigate how various control strategies enhance system performance based on their impacts on system oscillation modes and damping ratio. Additionally, as the offshore wind power generation is replacing the conventional fossil fuel generation, the study can seek the influence of the FFOWPS to power grid as the system inertial is reduced with high penetrate of wind generation. It would be intriguing to study the stability problems and seek for solution of such a system.
3. In Chapter 5, an economic analysis is conducted based on a single offshore wind farm that is connected to the onshore grid. The single offshore wind farm to grid topology will likely evolve into a offshore wind farm grid to onshore power grid topology as

renewable energy generation and transmission technologies advance. It would be fascinating to investigate the economic implications of adopting a more complex topology, such as fractional frequency AC grids. Additionally, a hybrid system may be developed and considered. Moreover, the cost analysis model can be improved. For the sake of simplicity, the O&M cost is assumed constant throughout the life of the project in the analysis model. In reality, however, the O&M cost may be lower during the first few years of equipment commissioned and increase as the equipment ages. This trend in the model could be investigated by additional research.

List of References

[1] H. Ritchie, M. Roser, and P. Rosado, "Energy," 2020. [Online]. Available: https://ourworldindata.org/energy

[2] IEA, " Net Zero by 2050, IEA, Paris https://www.iea.org/reports/net-zero-by-2050," 2021.

[3] REN21, "Renewables 2022 Global Status Report," 2022.

[4] GOV.UK, "Renewable electricity capacity and generation," 2022. [Online]. Available: https://www.gov.uk/government/statistics/energy-trends-section-6-renewables.

[5] GOV.UK, "Energy Trends June 2022," 2022. [Online]. Available: https://www.gov.uk/government/statistics/energy-trends-section-6-renewables

[6] GOV.UK, "British Energy Security Strategy," 2022. [Online]. Available: https://www.gov.uk/government/publications/british-energy-security-strategy

[7] GWEC, "Global Offshore Wind Report," 2022. [Online]. Available: https://gwec.net/gwecs-global-offshore-wind-report/

[8] W. EUROPE. Offshore wind in Europe - Key trends and statistics [Online] Available: https://windeurope.org/intelligence-platform/product/offshore-wind-in-europe-key-trends-and-statistics-2020/

[9] Y. Wang, G. Delille, H. Bayem, X. Guillaud, and B. Francois, "High Wind Power Penetration in Isolated Power Systems—Assessment of Wind Inertial and Primary Frequency Responses," *IEEE Transactions on Power Systems*, vol. 28, no. 3, pp. 2412-2420, 2013, doi: 10.1109/TPWRS.2013.2240466.

[10] G. Song, B. Cao, and L. Chang, "Review of Grid-forming Inverters in Support of Power System Operation," *Chinese Journal of Electrical Engineering*, vol. 8, no. 1, pp. 1-15, 2022, doi: 10.23919/CJEE.2022.000001.

[11] X. Fu *et al.*, "Large-Signal Stability of Grid-Forming and Grid-Following Controls in Voltage Source Converter: A Comparative Study," *IEEE Transactions on Power Electronics*, vol. 36, no. 7, pp. 7832-7840, 2021, doi: 10.1109/TPEL.2020.3047480.

[12] Drax, "Renewable curtailment and the role of long duration storage," 2022. [Online]. Available: https://www.drax.com/wp-content/uploads/2022/06/Drax-LCP-Renewable-curtailment-report-1.pdf
[13] A. Madariaga, I. M. de Alegría, J. L. Martín, P. Eguía, and S. Ceballos, "Current facts about offshore wind farms," *Renewable and Sustainable Energy Reviews*, vol. 16, no. 5, pp. 3105-3116, 2012/06/01/ 2012, doi: https://doi.org/10.1016/j.rser.2012.02.022.
[14] E. Apostolaki-Iosifidou, R. Mccormack, W. Kempton, P. Mccoy, and D. Ozkan, "Transmission Design and Analysis for Large-Scale Offshore Wind Energy Development," *IEEE Power and Energy Technology Systems Journal*, vol. 6, no. 1, pp. 22-31, 2019, doi: 10.1109/JPETS.2019.2898688.
[15] J. Song-Manguelle, M. H. Todorovic, S. Chi, S. K. Gunturi, and R. Datta, "Power Transfer Capability of HVAC Cables for Subsea Transmission and Distribution Systems," *IEEE Transactions on Industry Applications*, vol. 50, no. 4, pp. 2382-2391, 2014, doi: 10.1109/TIA.2013.2291934.
[16] R. Perveen and S. R. Mohanty, "Offshore wind farm development: Present status and challenges," *Renewable and Sustainable Energy Reviews*, vol. 29, 01/31 2014, doi: 10.1016/j.rser.2013.08.108.
[17] Y. Xue, X. Zhang, and C. Yang, "AC Filterless Flexible LCC HVDC With Reduced Voltage Rating of Controllable Capacitors," *IEEE Transactions on Power Systems*, vol. 33, no. 5, pp. 5507-5518, 2018, doi: 10.1109/TPWRS.2018.2800666.
[18] X. Liu and A. Lindemann, "Control of VSC-HVDC Connected Offshore Windfarms for Providing Synthetic Inertia," *IEEE Journal of Emerging and Selected Topics in Power Electronics*, vol. 6, no. 3, pp. 1407-1417, 2018, doi: 10.1109/JESTPE.2017.2751541.
[19] M. Saeedifard and R. Iravani, "Dynamic Performance of a Modular Multilevel Back-to-Back HVDC System," *IEEE Transactions on Power Delivery*, vol. 25, no. 4, pp. 2903-2912, 2010, doi: 10.1109/TPWRD.2010.2050787.
[20] S. Gang, W. Guoxiang, C. Xu, and Z. Chen, "Coordinated control of multi-terminal VSC-HVDC transmission for large offshore

wind farms," in *Proceedings of The 7th International Power Electronics and Motion Control Conference*, 2-5 June 2012 2012, vol. 2, pp. 1278-1282, doi: 10.1109/IPEMC.2012.6259035.

[21] W. Xifan and W. Xiuli, "Feasibility study of fractional frequency transmission system," *IEEE Transactions on Power Systems,* vol. 11, no. 2, pp. 962-967, 1996, doi: 10.1109/59.496181.

[22] X. Zhang *et al.*, "Selection of the rated frequency for fractional frequency offshore wind power system," in *2017 IEEE Conference on Energy Internet and Energy System Integration (EI2)*, 26-28 Nov. 2017 2017, pp. 1-6, doi: 10.1109/EI2.2017.8245643.

[23] B. Zhao, X. Wang, X. Wang, and S. Liu, "Upgrading Transmission Capacity by Altering HVAC into Fractional Frequency Transmission System," *IEEE Transactions on Power Delivery,* pp. 1-1, 2021, doi: 10.1109/tpwrd.2021.3139726.

[24] W. Fischer, R. Braun, and I. Erlich, "Low frequency high voltage offshore grid for transmission of renewable power," in *2012 3rd IEEE PES Innovative Smart Grid Technologies Europe (ISGT Europe)*, 14-17 Oct. 2012 2012, pp. 1-6, doi: 10.1109/ISGTEurope.2012.6465646.

[25] V. Yaramasu, B. Wu, P. C. Sen, S. Kouro, and M. Narimani, "High-power wind energy conversion systems: State-of-the-art and emerging technologies," *Proceedings of the IEEE,* vol. 103, no. 5, pp. 740-788, 2015, doi: 10.1109/JPROC.2014.2378692.

[26] Y. Duan and R. G. Harley, "Present and future trends in wind turbine generator designs," in *2009 IEEE Power Electronics and Machines in Wind Applications*, 24-26 June 2009 2009, pp. 1-6, doi: 10.1109/PEMWA.2009.5208401.

[27] D. J. Trudnowski, A. Gentile, J. M. Khan, and E. M. Petritz, "Fixed-speed wind-generator and wind-park modeling for transient stability studies," *IEEE Transactions on Power Systems,* vol. 19, no. 4, pp. 1911-1917, 2004, doi: 10.1109/TPWRS.2004.836204.

[28] M. Yamamoto and O. Motoyoshi, "Active and reactive power control for doubly-fed wound rotor induction generator," *IEEE Transactions on Power Electronics,* vol. 6, no. 4, pp. 624-629, 1991, doi: 10.1109/63.97761.

[29] G. Abad, J. Lopez Taberna, M. Rodríguez, L. Marroyo, and G. Iwanski, *Doubly Fed Induction Machine: Modeling and Control for Wind Energy Generation*. 2011, pp. 619-625.
[30] B. Bose, "Modern Power Electronics and AC Drives," 2002.
[31] W. A. Hill, E. Ho, and I. Neuzil, "Dynamic behaviour of a cycloconverter system," in *Conference Record of the 1990 IEEE Industry Applications Society Annual Meeting*, 7-12 Oct. 1990 1990, pp. 1024-1030 vol.2, doi: 10.1109/IAS.1990.152310.
[32] C. Yongnam, G. J. Cokkinides, and A. P. Meliopoulos, "Time domain simulation of a three-phase cycloconverter for LFAC transmission systems," in *PES T&D 2012*, 7-10 May 2012 2012, pp. 1-8, doi: 10.1109/TDC.2012.6281559.
[33] N. Lianhui, W. Xifan, and T. Yufei, "Experiment on wind power integration grid via fractional frequency transmission system: Realization of the variable-speed variable-frequency power wind," in *2011 4th International Conference on Electric Utility Deregulation and Restructuring and Power Technologies (DRPT)*, 6-9 July 2011 2011, pp. 444-449, doi: 10.1109/DRPT.2011.5993932.
[34] J. Li and X. Zhang, "Small Signal Stability of Fractional Frequency Transmission System With Offshore Wind Farms," *IEEE Transactions on Sustainable Energy*, vol. 7, no. 4, pp. 1538-1546, 2016, doi: 10.1109/TSTE.2016.2552540.
[35] J. Ruddy, R. Meere, and T. O'Donnell, "Low Frequency AC transmission for offshore wind power: A review," *Renewable and Sustainable Energy Reviews*, vol. 56, pp. 75-86, 2016/04/01/ 2016, doi: https://doi.org/10.1016/j.rser.2015.11.033.
[36] Y. Tang, Z. Zhang, and Z. Xu, "DRU Based Low Frequency AC Transmission Scheme for Offshore Wind Farm Integration," *IEEE Transactions on Sustainable Energy*, vol. 12, no. 3, pp. 1512-1524, 2021, doi: 10.1109/TSTE.2021.3053051.
[37] Y. Tang, P. B. Wyllie, J. Yu, X. M. Wang, L. Ran, and O. Alatise, "Offshore low frequency AC transmission with back-to-back modular multilevel converter (MMC)," in *11th IET International Conference on AC and DC Power Transmission*, 10-12 Feb. 2015 2015, pp. 1-8, doi: 10.1049/cp.2015.0020.

[38] R. W. Erickson and O. A. Al-Naseem, "A new family of matrix converters," in *IECON'01. 27th Annual Conference of the IEEE Industrial Electronics Society (Cat. No.37243)*, 29 Nov.-2 Dec. 2001 2001, vol. 2, pp. 1515-1520 vol.2, doi: 10.1109/IECON.2001.976015.
[39] W. Biyang *et al.*, "Reliability comparison of two types of converters for fractional frequency transmission system," in *2016 IEEE PES Asia-Pacific Power and Energy Engineering Conference (APPEEC)*, 25-28 Oct. 2016 2016, pp. 1627-1631, doi: 10.1109/APPEEC.2016.7779768.
[40] S. Liu, X. Wang, B. Wang, S. Pengwei, Z. Qian, and C. Yong, "Comparison between back-to-back MMC and M³C as high power AC/AC converters," in *2016 IEEE PES Asia-Pacific Power and Energy Engineering Conference (APPEEC)*, 25-28 Oct. 2016 2016, pp. 671-676, doi: 10.1109/APPEEC.2016.7779588.
[41] J. Luo, X. P. Zhang, and Y. Xue, "Small Signal Model of Modular Multilevel Matrix Converter for Fractional Frequency Transmission System," *IEEE Access*, vol. 7, pp. 110187-110196, 2019, doi: 10.1109/ACCESS.2019.2932050.
[42] W. Kawamura, M. Hagiwara, H. Akagi, M. Tsukakoshi, R. Nakamura, and S. Kodama, "AC-Inductors Design for a Modular Multilevel TSBC Converter, and Performance of a Low-Speed High-Torque Motor Drive Using the Converter," *IEEE Transactions on Industry Applications*, vol. 53, no. 5, pp. 4718-4729, 2017, doi: 10.1109/TIA.2017.2713338.
[43] W. Kawamura, M. Hagiwara, and H. Akagi, "Control and Experiment of a Modular Multilevel Cascade Converter Based on Triple-Star Bridge Cells," *IEEE Transactions on Industry Applications*, vol. 50, no. 5, pp. 3536-3548, 2014, doi: 10.1109/TIA.2014.2311759.
[44] S. Liu, M. Saeedifard, and X. Wang, "Analysis and Control of the Modular Multilevel Matrix Converter Under Unbalanced Grid Conditions," *IEEE Journal of Emerging and Selected Topics in Power Electronics*, vol. 6, no. 4, pp. 1979-1989, 2018, doi: 10.1109/JESTPE.2018.2812723.

[45] S. Hillmansen and C. Roberts, "Energy storage devices in hybrid railway vehicles: A kinematic analysis," *Proceedings of the Institution of Mechanical Engineers, Part F: Journal of Rail and Rapid Transit*, vol. 221, no. 1, pp. 135-143, 2007/01/01 2007, doi: 10.1243/09544097JRRT99.
[46] S. Lu, P. Weston, S. Hillmansen, H. B. Gooi, and C. Roberts, "Increasing the Regenerative Braking Energy for Railway Vehicles," *IEEE Transactions on Intelligent Transportation Systems*, vol. 15, no. 6, pp. 2506-2515, 2014, doi: 10.1109/TITS.2014.2319233.
[47] P. Sun, X. Wang, L. Ning, S. Liu, L. Tang, and M. Lu, "The application of modular multilevel matrix converter in fractional frequency offshore wind power system," in *2016 IEEE 16th International Conference on Environment and Electrical Engineering (EEEIC)*, 7-10 June 2016 2016, pp. 1-4, doi: 10.1109/EEEIC.2016.7555879.
[48] Y. Miura, T. Mizutani, M. Ito, and T. Ise, "Modular multilevel matrix converter for low frequency AC transmission," in *2013 IEEE 10th International Conference on Power Electronics and Drive Systems (PEDS)*, 22-25 April 2013 2013, pp. 1079-1084, doi: 10.1109/PEDS.2013.6527180.
[49] Y. Miura, T. Fujikawa, T. Yoshida, and T. Ise, "Control scheme of the modular multilevel matrix converter using space vector modulation for wide frequency range operation," in *2017 IEEE Energy Conversion Congress and Exposition (ECCE)*, 1-5 Oct. 2017 2017, pp. 1084-1091, doi: 10.1109/ECCE.2017.8095908.
[50] F. Kammerer, J. Kolb, and M. Braun, "Fully decoupled current control and energy balancing of the Modular Multilevel Matrix Converter," in *2012 15th International Power Electronics and Motion Control Conference (EPE/PEMC)*, 4-6 Sept. 2012 2012, pp. LS2a.3-1-LS2a.3-8, doi: 10.1109/EPEPEMC.2012.6397408.
[51] S. Liu, X. Wang, Y. Meng, P. Sun, H. Luo, and B. Wang, "A Decoupled Control Strategy of Modular Multilevel Matrix Converter for Fractional Frequency Transmission System," *IEEE Transactions on Power Delivery*, vol. 32, no. 4, pp. 2111-2121, 2017, doi: 10.1109/TPWRD.2016.2646384.

[52] M. Diaz *et al.*, "Vector Control of a Modular Multilevel Matrix Converter Operating Over the Full Output-Frequency Range," *IEEE Transactions on Industrial Electronics*, vol. 66, no. 7, pp. 5102-5114, 2019, doi: 10.1109/TIE.2018.2870367.

[53] W. Yao, J. Liu, and Z. Lu, "Distributed Control for the Modular Multilevel Matrix Converter," *IEEE Transactions on Power Electronics*, vol. 34, no. 4, pp. 3775-3788, 2019, doi: 10.1109/TPEL.2018.2849027.

[54] R. Alaei, S. A. Khajehoddin, and W. Xu, "Control and Experiment of AC/AC Sparse Modular Multilevel Converter," *IEEE Transactions on Power Delivery*, vol. 32, no. 3, pp. 1527-1534, 2017, doi: 10.1109/TPWRD.2016.2618935.

[55] S. Liu, M. Saeedifard, X. Wang, and B. Zhao, "A Current Reallocation Strategy to Attenuate the Peak Arm Current of the Modular Multilevel Matrix Converter," *IEEE Journal of Emerging and Selected Topics in Power Electronics*, vol. 7, no. 4, pp. 2292-2302, 2019, doi: 10.1109/JESTPE.2019.2892420.

[56] B. Fan, K. Wang, Z. Zheng, L. Xu, and Y. Li, "Optimized Branch Current Control of Modular Multilevel Matrix Converters Under Branch Fault Conditions," *IEEE Transactions on Power Electronics*, vol. 33, no. 6, pp. 4578-4583, 2018, doi: 10.1109/TPEL.2017.2769117.

[57] C. Melendez, M. Diaz, S. Cerda, F. Rojas, and H. Chavez, "Frequency Support Control of a Modular Multilevel Matrix Converter based Wind Energy Conversion System," in *2018 IEEE International Conference on Automation/XXIII Congress of the Chilean Association of Automatic Control (ICA-ACCA)*, 17-19 Oct. 2018 2018, pp. 1-6, doi: 10.1109/ICA-ACCA.2018.8609738.

[58] J. Ma, M. Dahidah, V. Pickert, and J. Yu, "Modular multilevel matrix converter for offshore low frequency AC transmission system," in *2017 IEEE 26th International Symposium on Industrial Electronics (ISIE)*, 19-21 June 2017 2017, pp. 768-774, doi: 10.1109/ISIE.2017.8001343.

[59] T. H. Nguyen and D. Lee, "Control of offshore wind farms based on HVDC," in *2012 IEEE Energy Conversion Congress and*

Exposition (ECCE), 15-20 Sept. 2012 2012, pp. 3113-3118, doi: 10.1109/ECCE.2012.6342354.
[60] P. Kundur *et al.*, "Definition and classification of power system stability IEEE/CIGRE joint task force on stability terms and definitions," *IEEE Transactions on Power Systems*, vol. 19, no. 3, pp. 1387-1401, 2004, doi: 10.1109/TPWRS.2004.825981.
[61] P. B. N. J. L. M. G. Kundur, *Power system stability and control*. New York: McGraw-Hill (in English), 1994.
[62] X.-F. S. Y.-H. I. M. Wang, "Modern power systems analysis," (in English.), 2008. [Online]. Available: http://public.ebookcentral.proquest.com/choice/publicfullrecord.aspx?p=763215.
[63] M. Klein, G. J. Rogers, and P. Kundur, "A fundamental study of inter-area oscillations in power systems," *IEEE Transactions on Power Systems*, vol. 6, no. 3, pp. 914-921, 1991, doi: 10.1109/59.119229.
[64] Z. Saad-Saoud and N. Jenkins, "Simple wind farm dynamic model," *IEE Proceedings - Generation, Transmission and Distribution*, vol. 142, no. 5, pp. 545-548. [Online]. Available: https://digital-library.theiet.org/content/journals/10.1049/ip-gtd_19952121
[65] L. Holdsworth, X. G. Wu, J. B. Ekanayake, and N. Jenkins, "Comparison of fixed speed and doubly-fed induction wind turbines during power system disturbances," *IEE Proceedings - Generation, Transmission and Distribution*, vol. 150, no. 3, pp. 343-352. [Online]. Available: https://digital-library.theiet.org/content/journals/10.1049/ip-gtd_20030251
[66] R. Pena, J. C. Clare, and G. M. Asher, "Doubly fed induction generator using back-to-back PWM converters and its application to variable-speed wind-energy generation," *IEE Proceedings - Electric Power Applications*, vol. 143, no. 3, pp. 231-241. [Online]. Available: https://digital-library.theiet.org/content/journals/10.1049/ip-epa_19960288
[67] L. Yazhou, A. Mullane, G. Lightbody, and R. Yacamini, "Modeling of the wind turbine with a doubly fed induction generator for grid integration studies," *IEEE Transactions on*

Energy Conversion, vol. 21, no. 1, pp. 257-264, 2006, doi: 10.1109/TEC.2005.847958.
[68] J. Ekanayake, L. Holdsworth, X. Wu, and N. Jenkins, "Dynamic modeling of doubly fed induction generator wind turbines," *Power Systems, IEEE Transactions on*, vol. 18, pp. 803-809, 06/01 2003, doi: 10.1109/TPWRS.2003.811178.
[69] I. Erlich, J. Kretschmann, J. Fortmann, S. Mueller-Engelhardt, and H. Wrede, "Modeling of Wind Turbines Based on Doubly-Fed Induction Generators for Power System Stability Studies," *IEEE Transactions on Power Systems*, vol. 22, no. 3, pp. 909-919, 2007, doi: 10.1109/TPWRS.2007.901607.
[70] F. Wu, X. P. Zhang, K. Godfrey, and P. Ju, "Small signal stability analysis and optimal control of a wind turbine with doubly fed induction generator," *Generation, Transmission & Distribution, IET*, vol. 1, pp. 751-760, 10/01 2007, doi: 10.1049/iet-gtd:20060395.
[71] L. Yang, G. Yang, Z. Xu, Z. Y. Dong, K. Wong, and X. Ma, "Optimal controller design of doubly-fed induction generator wind turbine system for small signal stability enhancement," *Generation, Transmission & Distribution, IET*, vol. 4, pp. 579-597, 06/01 2010, doi: 10.1049/iet-gtd.2009.0553.
[72] J. G. Slootweg and W. L. Kling, "Kling, W.L.: The impact of large scale wind power generation on power system oscillations. Electrical Power System Research 67(1), 9-20," *Electric Power Systems Research*, vol. 67, pp. 9-20, 10/01 2003, doi: 10.1016/S0378-7796(03)00089-0.
[73] E. Hagstrøm, I. Norheim, and K. Uhlen, "Large - scale wind power integration in Norway and impact on damping in the Nordic grid," *Wind Energy*, vol. 8, pp. 375-384, 07/01 2005, doi: 10.1002/we.168.
[74] D. Gautam, V. Vittal, and T. Harbour, "Impact of Increased Penetration of DFIG-Based Wind Turbine Generators on Transient and Small Signal Stability of Power Systems," *IEEE Transactions on Power Systems*, vol. 24, no. 3, pp. 1426-1434, 2009, doi: 10.1109/TPWRS.2009.2021234.

[75] C. Schauder, "Vector analysis and control of advanced static VAr compensators," in *International Conference on AC and DC Power Transmission*, 17-20 Sept. 1991 1991, pp. 266-272.

[76] Q. Hao, Z. Li, F. Gao, and J. Zhang, "Reduced-Order Small-Signal Models of Modular Multilevel Converter and MMC-Based HVdc Grid," *IEEE Transactions on Industrial Electronics,* vol. 66, no. 3, pp. 2257-2268, 2019, doi: 10.1109/TIE.2018.2869358.

[77] L. Xu, L. Yao, and C. Sasse, "Grid Integration of Large DFIG-Based Wind Farms Using VSC Transmission," *IEEE Transactions on Power Systems,* vol. 22, no. 3, pp. 976-984, 2007, doi: 10.1109/TPWRS.2007.901306.

[78] Y. Liu, A. Q. Huang, W. Song, S. Bhattacharya, and G. Tan, "Small-Signal Model-Based Control Strategy for Balancing Individual DC Capacitor Voltages in Cascade Multilevel Inverter-Based STATCOM," *IEEE Transactions on Industrial Electronics,* vol. 56, no. 6, pp. 2259-2269, 2009, doi: 10.1109/TIE.2009.2017101.

[79] C. Andalib-Bin-Karim, M. R. Hossain, M. I. Adham, and A. Ahmed, "Small signal stability analysis of power system equipped with VSC based back to back HVDC," in *2015 International Conference on Electrical Engineering and Information Communication Technology (ICEEICT)*, 21-23 May 2015 2015, pp. 1-6, doi: 10.1109/ICEEICT.2015.7307367.

[80] T. Li, A. M. Gole, and C. Zhao, "Harmonic Instability in MMC-HVDC Converters Resulting From Internal Dynamics," *IEEE Transactions on Power Delivery,* vol. 31, no. 4, pp. 1738-1747, 2016, doi: 10.1109/TPWRD.2016.2542188.

[81] G. B. Diaz, J. A. Suul, and S. D. Arco, "Small-signal state-space modeling of modular multilevel converters for system stability analysis," in *2015 IEEE Energy Conversion Congress and Exposition (ECCE)*, 20-24 Sept. 2015 2015, pp. 5822-5829, doi: 10.1109/ECCE.2015.7310477.

[82] A. Jamshidifar and D. Jovcic, "Small-Signal Dynamic DQ Model of Modular Multilevel Converter for System Studies," *IEEE Transactions on Power Delivery,* vol. 31, no. 1, pp. 191-199, 2016, doi: 10.1109/TPWRD.2015.2478489.

[83] IRENA, "Renewable Power Generation Costs in 2021," 2022. [Online]. Available: https://irena.org/publications/2022/Jul/Renewable-Power-Generation-Costs-in-2021
[84] A. Gonzalez, "Review of offshore wind farm cost components," *Energy for Sustainable Development*, vol. 37, pp. 10-19, 04/01 2017, doi: 10.1016/j.esd.2016.12.001.
[85] B. C. Ummels, E. Pelgrum, and W. L. Kling, "Integration of large-scale wind power and the use of energy storage in the Netherlands," *Renewable Power Generation, IET*, vol. 2, pp. 34-46, 04/01 2008, doi: 10.1049/iet-rpg:20070056.
[86] E. Haghi, M. Fwoler, and K. Raahemifar, "Economic analysis of hydrogen production in context of a microgrid," in *2017 IEEE International Conference on Smart Energy Grid Engineering (SEGE)*, 14-17 Aug. 2017 2017, pp. 79-84, doi: 10.1109/SEGE.2017.8052780.
[87] H. Tebibel, "Wind Turbine Power System for Hydrogen Production and Storage: Techno-economic Analysis," in *2018 International Conference on Wind Energy and Applications in Algeria (ICWEAA)*, 6-7 Nov. 2018 2018, pp. 1-6, doi: 10.1109/ICWEAA.2018.8605079.
[88] B. F. Ronad and S. H. Jangamshetti, "Optimal cost analysis of wind-solar hybrid system powered AC and DC irrigation pumps using HOMER," in *2015 International Conference on Renewable Energy Research and Applications (ICRERA)*, 22-25 Nov. 2015 2015, pp. 1038-1042, doi: 10.1109/ICRERA.2015.7418568.
[89] W. Ma, X. Xue, and G. Liu, "Techno-economic evaluation for hybrid renewable energy system: Application and merits," *Energy*, vol. 159, pp. 385-409, 2018/09/15/ 2018, doi: https://doi.org/10.1016/j.energy.2018.06.101.
[90] L. Wang, T. Yeh, W. Lee, and Z. Chen, "Benefit Evaluation of Wind Turbine Generators in Wind Farms Using Capacity-Factor Analysis and Economic-Cost Methods," *IEEE Transactions on Power Systems*, vol. 24, no. 2, pp. 692-704, 2009, doi: 10.1109/TPWRS.2009.2016519.
[91] D. Elliott *et al.*, "A Comparison of AC and HVDC Options for the Connection of Offshore Wind Generation in Great Britain,"

IEEE Transactions on Power Delivery, vol. 31, no. 2, pp. 798-809, 2016, doi: 10.1109/TPWRD.2015.2453233.
[92] P. Bresesti, W. L. Kling, R. L. Hendriks, and R. Vailati, "HVDC Connection of Offshore Wind Farms to the Transmission System," *IEEE Transactions on Energy Conversion*, vol. 22, no. 1, pp. 37-43, 2007, doi: 10.1109/TEC.2006.889624.
[93] X. Xiang, M. M. C. Merlin, and T. C. Green, "Cost analysis and comparison of HVAC, LFAC and HVDC for offshore wind power connection," in *12th IET International Conference on AC and DC Power Transmission (ACDC 2016)*, 28-29 May 2016 2016, pp. 1-6, doi: 10.1049/cp.2016.0386.
[94] J. Ruddy, R. Meere, and T. O'Donnell, "A Comparison of VSC-HVDC with Low Frequency AC for Offshore Wind Farm Design and Interconnection," *Energy Procedia*, vol. 80, pp. 185-192, 12/01 2015, doi: 10.1016/j.egypro.2015.11.421.
[95] F. Deng and Z. Chen, "A Control Method for Voltage Balancing in Modular Multilevel Converters," *IEEE Transactions on Power Electronics*, vol. 29, no. 1, pp. 66-76, 2014, doi: 10.1109/TPEL.2013.2251426.
[96] B. Chuco and E. H. Watanabe, "Back-to-back HVDC based on Modular Multilevel Converter," in *XI Brazilian Power Electronics Conference*, 11-15 Sept. 2011 2011, pp. 970-976, doi: 10.1109/COBEP.2011.6085335.
[97] W. Europe, "Wind Energy in Europe: 2021 Statistics and the outlook for 2022-2026," 2022. [Online]. Available: https://windeurope.org/intelligence-platform/product/wind-energy-in-europe-2021-statistics-and-the-outlook-for-2022-2026/
[98] J. Luo, K. Lin, J. Li, Y. Xue, and X. Zhang, "Cost analysis and comparison between modular multilevel converter (MMC) and modular multilevel matrix converter (M³C) for offshore wind power transmission," in *15th IET International Conference on AC and DC Power Transmission (ACDC 2019)*, 5-7 Feb. 2019 2019, pp. 1-6, doi: 10.1049/cp.2019.0063.
[99] T. Stehly and P. Duffy, "2020 Cost of Wind Energy Review," United States, 2021-12-28 2021. [Online]. Available: https://www.osti.gov/biblio/1838135

[100] RenewablesFirst. "Wind Power Learning Center." https://www.renewablesfirst.co.uk/windpower/windpower-learning-centre/ (accessed.
[101] X. Wang, Y. Teng, L. Ning, Y. Meng, and Z. Xu, "Feasibility of integrating large wind farm via fractional frequency transmission system a case study," *International Transactions on Electrical Energy Systems*, vol. 24, 01/01 2014, doi: 10.1002/etep.1706.
[102] NorthSeaGrid, "Annexes to the Final Report," 2014. [Online]. Available: http://northseagrid.info/sites/default/files/NorthSeaGrid_Final_Report_Annexes.pdf
[103] S. Liu, X. Wang, L. Ning, B. Wang, M. Lu, and C. Shao, "Integrating Offshore Wind Power Via Fractional Frequency Transmission System," *IEEE Transactions on Power Delivery*, vol. 32, no. 3, pp. 1253-1261, 2017, doi: 10.1109/TPWRD.2015.2435993.
[104] D. Woodford, "Symmetrical Monopole VSC transmission," *Electranix technical paper*, 2014.
[105] C. W. G. B1.40, "CIGRE Report 610: Offshore Generation Cable Connections," 2015.
[106] A. Friday and M. Luckett, "Economic Analysis of Large Submarine Cables," 2016. [Online]. Available: https://ore.catapult.org.uk/app/uploads/2018/02/Economic-Analysis-of-Large-Submarine-Cables.pdf
[107] I. E. Commission, "Availability for wind energy generation systems (IEC 61400-26-1:2019)," 2019.
[108] G. W. Ault and D. McMillan, "Specification of reliability benchmarks for offshore wind farms," 2008.
[109] J. Carroll, "Reliability comparison of wind turbines with DFIG and PMG drive trains," in *2015 IEEE Power & Energy Society General Meeting*, 26-30 July 2015 2015, pp. 1-1, doi: 10.1109/PESGM.2015.7286449.
[110] W. G. B3.36, "CIGRE Report 612: Special Considerations for AC Collector Systems and Substations Associated with HVDC," 2015.

[111] M. G. BENNETT, N. S. DHALIWAL, and A. LEIRBUKT, "A Survey of The Reliability of HVDC Systems Throughout The World During 2011-2012," 2014.
[112] 4Coffshore. "Offshore Converter Events." https://www.4coffshore.com/transmission/ (accessed.
[113] L. Rademakers, H. Braam, and T. Obdam, "Operation and maintenance of offshore wind energy systems," 2011, pp. 546-583.
[114] B. Eeckhout, D. Van Hertem, M. Reza, K. Srivastava, and R. Belmans, "Economic comparison of VSC HVDC and HVAC as transmission system for a 300 MW offshore wind farm," *European Transactions on Electrical Power*, vol. 20, pp. 661-671, 06/10 2009, doi: 10.1002/etep.359.
[115] T. J. Stehly, D. M. Heimiller, and G. N. Scott, "2016 Cost of Wind Energy Review," United States, 2017-12-29 2017. [Online]. Available: https://www.osti.gov/biblio/1415731
[116] N. Barberis Negra, J. Todorovic, and T. Ackermann, "Loss evaluation of HVAC and HVDC Transmission solutions for large offshore wind farms," *Electric Power Systems Research*, vol. 76, pp. 916-927, 07/01 2006, doi: 10.1016/j.epsr.2005.11.004.
[117] J. Tamura, "Calculation Method of Losses and Efficiency of Wind Generators," in *Wind Energy Conversion Systems: Technology and Trends*, S. M. Muyeen Ed. London: Springer London, 2012, pp. 25-51.
[118] A. Papadopoulos, S. Rodrigues, E. Kontos, T. Todorcevic, P. Bauer, and R. T. Pinto, "Collection and transmission losses of offshore wind farms for optimization purposes," in *2015 IEEE Energy Conversion Congress and Exposition (ECCE)*, 20-24 Sept. 2015 2015, pp. 6724-6732, doi: 10.1109/ECCE.2015.7310601.
[119] H. Khatib, *Economic Evaluation of Projects in the Electricity Supply Industry*. Institution of Engineering and Technology, 2003.
[120] E. Numbers. "UK offshore wind capacity factors." https://energynumbers.info/uk-offshore-wind-capacity-factors (accessed.
[121] Elexon. "Balancing mechanism reporting service." https://www.bmreports.com/bmrs/?q=help/about-us (accessed.

List of Publications

1. Kai Lin and Xiao-Ping Zhang, "Small Signal Stability Analysis of Fractional Frequency Offshore Wind Power System with Modular Multilevel Matrix Converter", *IEEE Access, Under review.*
2. Jiajie Luo, Kai Lin, Jianing Li, Ying Xue and Xiao-Ping Zhang, "Cost analysis and comparison between modular multilevel converter (MMC) and modular multilevel matrix converter (M^3C) for offshore wind power transmission," *15th IET International Conference on AC and DC Power Transmission (ACDC 2019)*, 2019, pp. 1-6, doi: 10.1049/cp.2019.0063.

APPENDIX A

DFIG SYSTEM PARAMETERS

Per unit system: $S_w = 1.5\ MW$, $V_b = 0.575\ kV$, $f = 20\ Hz$.

Wind turbine: $H_t = 3\ s$, $V_w = 15\ m/s$, $C_p = 0.4382$, $R = 37.049\ m$, $\rho = 1.225\ kg/m^3$, $N_{turbine} = 20$.

Generator of DFIG: $R_s = 0.00706\ pu$, $L_m = 2.9\ pu$, $L_{ss} = 3.07\ pu$, $L_{rr} = 3.05\ pu$, $R_r = 0.005\ pu$, $H_g = 1\ s$.

Converter: $C = 10\ mF$, $v_{DC} = 1.5\ kV$, $L_g = 0.3\ pu$, $R_g = 0.003\ pu$.

$\mathbf{M^3}$C SYSTEM PARAMETERS

Per unit system: $S_c = 30\ MW$, $V_l = 33\ kV$, $f_1 = 20\ Hz$, $f_2 = 60\ Hz$.

Converter: $N_{arm} = 40$, $L_{arm} = 15\ mH$, $R_{arm} = 0.1\Omega$, $C_{sm} = 10\ mF$, $U_{DC} = 1.5\ kV$.

TRANSMISSION LINE

Distance: $100\ km$

Line – to – line RMS voltage: 120 kV

Impedance: $R_{TL} = 0.1153\ \Omega/km$, $L_{TL} = 0.00105\ H/km$

ORIGINAL CONTROL PARAMETERS

DFIG: $k_{p1} = 100$, $k_{i1} = 5$; $k_{p2} = 1$, $k_{i2} = 0.1$; $k_{p3} = 3$, $k_{i3} = 30$; $k_{p4} = 1$, $k_{i4} = 100$; $k_{p5} = 0.1$, $k_{i5} = 20$.

M^3C: $k_{p1} = 0.5$, $k_{i1} = 10$; $k_{p2} = 50$, $k_{i2} = 50$; $k_{p3} = 5$, $k_{i3} = 100$.

OPTIMIZED CONTROL PARAMETERS

DFIG: $k_{p1} = 120$, $k_{i1} = 20$; $k_{p2} = 0.2$, $k_{i2} = 1$; $k_{p3} = 20$, $k_{i3} = 65$; $k_{p4} = 8$, $k_{i4} = 400$; $k_{p5} = 0.83$, $k_{i5} = 5$.

M^3C: $k_{p1} = 25$, $k_{i1} = 5$; $k_{p2} = 0.5$, $k_{i2} = 5$; $k_{p3} = 35$, $k_{i3} = 50$.